Spectrophotometry of the infrared emission of Earth-like Planets

Illeana Gómez Leal

SPECTROPHOTOMETRY OF THE INFRARED EMISSION OF EARTH-LIKE PLANETS

Centre National de la Recherche Scientifique
Laboratoire d'Astrophysique de Bordeaux
CNRS. OASU-LAB

Université de Bordeaux 1
École Doctorale des Sciences Physiques et de l'Ingénieur
Speciality: Plasma, Nuclear and Astrophysics

Illeana Gómez Leal

THÈSE

PRÉSENTÉE À

l'Université de Bordeaux 1

École Doctorale des Sciences Physiques et de l'Ingénieur

par **Illeana GÓMEZ LEAL**

POUR OBTENIR LE GRADE DE

DOCTEUR

SPÉCIALITÉ: ASTROPHYSIQUE, PLASMAS, NUCLÉAIRE

Spectrophotométrie de l'emission infrarouge des exoplanètes telluriques

---

Soutenue le : 11 juillet 2013

Après avis de : Eduardo Martín..... Rapporteur
Marc Ollivier..... Rapporteur

Devant la Commision d'examen formée de :

Francis Codron	M. de Conf., Université Pierre et Marie Curie, LMD.....	Examinateur
Muriel Gargaud	Directrice de Recherche, LAB, CNRS.....	Présidente
Eduardo Martín	Professeur, Centro de Astrobiología, INTA-CSIC.....	Rapporteur
Marc Ollivier	Astronome, Université de Paris-Sud, IAS.....	Rapporteur
Enric Pallé	Ch. de Recherche, Inst. Astrofísico de Canarias, IAC.....	Examinateur
Franck Selsis	Chargé de Recherche, LAB, CNRS.....	Directeur de thèse

La filosofia naturale è scritta in questo grandissimo libro che continuamente ci sta aperto innanzi agli occhi, io dico l'universo, ma non si può intendere se prima non s'impara a intender la lingua e conoscer i caratteri nei quali è scritto. Egli è scritto in lingua matematica, e i caratteri son triangoli, cerchi ed altre figure geometriche, senza i quali mezzi è impossibile a intenderne umanamente parola; senza questi è un aggirarsi vanamente per un oscuro labirinto.

Il Saggiatore, Galileo Galilei (1564-1642)

Abstract

The thermal emission received from a planet is a key to characterize the physical and chemical properties of its atmosphere. The spectral resolution, and therefore the spectral characterization that we can achieve for extrasolar planets is unfortunately very limited in particular for terrestrial planets. In this thesis, we study the possibility to characterize an Earth-like exoplanet by the analysis of the broadband infrared emission variability. The apparent thermal emission is indeed modulated by the seasons, the rotation of the planet, the motion and variability of atmospheric patterns and clouds, the orbital phase, and even the presence of a moon. As a reference case, we have studied the thermal emission of the Earth seen as a distant point-source, as well as the variability and the dependency of the signal on the observation geometry. We have modeled the emission of the Earth using data derived from observations and data produced by a General Circulation Models (GCMs), comparing both types of data in order to validate our simulations.

As a second part of our work, we have used the GCM to model Earth-like planets that differ from the Earth by a few parameters such as different rotation rates (including tidally-locked planets), a planetary surface completely covered by ice or water, different obliquities and eccentricities. For all these virtual planets, we have studied the climate derived from the physical properties and the photometric infrared signal associated with them.

The last part of the thesis is a preliminary work that no longer consider the bolometric emission but the signal from narrow spectral bands, thanks to a new generation of GCMs. Because each band probes a specific level in the atmosphere, studying how the low resolution spectrum of the planets varies by comparing the photometric variabilities between bands, we can study the dynamics, composition, distribution and evolution of the atmosphere of the planet, which it opens a yet unexplored field for the characterization of exoplanets.

Résumé (français)

Le signal thermique d'une exoplanète tellurique est une clé pour caractériser les propriétés physiques et chimiques de son atmosphère. La résolution spectrale, et donc la caractérisation spectrale que nous pouvons réaliser des planètes extrasolaires, est malheureusement très limité, en particulier pour les planètes similaires à la Terre. Dans cette thèse, j'ai étudié la possibilité de caractériser des exoplanètes telluriques par l'analyse de la variabilité de son émission infrarouge. L'émission thermique apparente est en effet modulée par les saisons, la rotation de la planète, le mouvement et la variabilité des nuages, la phase orbitale, et aussi par la présence des satellites naturels.

Premièrement, nous avons étudié l' émission thermique de la Terre vue en tant que point-source distante, ainsi que la variabilité et la dépendance du signal de la géométrie d'observation. J'ai modélisé l'émission de la Terre à l'aide des données satellitaires et des données produites par des modèles de circulation général (GCMs) du Laboratoire de Météorologie Dynamique de Paris (LMD), en comparant les deux types de données afin de valider les simulations.

Pendant la deuxième partie de mon travail, j'ai utilisé des donnés du GCM pour modéliser des planètes telluriques qui diffèrent de la Terre par seulement un ou deux paramètres tels que: la vitesse de rotation (y compris des planètes synchrones), une surface planétaire entièrement recouverte par la glace ou de l'eau, l'obliquité de l'axe de rotation ou l'excentricité de l'orbite. Pour toutes ces planètes virtuelles, j'ai étudié le climat, déduit les propriétés physiques de la planète, et produit et analysé les signaux integrées associés à différentes géometries d'observation.

La dernière partie de la thèse est un travail préliminaire qui consiste en ne plus considérer l'émission bolométrique mais le signal de bandes spectrales étroites, grâce à une nouvelle génération de GCM. Parce que chaque bande explore un niveau spécifique dans l'atmosphère, l'étude de la variation du spectre en comparant les variabilités photométriques entre les bandes, permet d'étudier la dynamique, la composition, la

distribution et l'évolution de l'atmosphère de la planète, ce qui ouvre un champ encore inexploré pour la caractérisation des exoplanètes.

Acknowledgements

I would like to thank all the people who have contributed in some way or another to the work presented in this thesis. First, I would like to express my gratitude to my supervisor, Dr. Franck Selsis, whose patience and expertise encouraged me throughout all my time in the Laboratoire d'Astrophysique de Bordeaux, for accepting me into his group and giving me the intellectual freedom and support to develop my research. Secondly, I am very grateful to Dr. Enric Pallé for introducing me in the wonderful field of exoplanets during my master thesis in the Instituto Astrófisico de Canarias and for his collaboration in the first part of this work, and I am also thankful to Dr. Francis Codron, who have the credit to develop the Earth LMD GCM, and whose invaluable knowledge in climatology and hard work have been essential in the development of the signal of Earth-like planets shown in this thesis. I would also like to thank the other members of my commitee, Dr. Muriel Gargaud, Dr. Eduardo Martín and Dr. Marc Ollivier for their interest and their insightful comments. During my collaboration with the Laboratoire de Météorologie Dynamique de Paris, I have had the privilege to work with Dr. Robin Wordsworth and Benjamin Charnay, whose motivating discussions, work and invaluable help had been extremely useful in the development of my work.

This work would not have been possible without the care and support of many others. One of the best experiences in my thesis has been the "European Research Course on Atmospheres" (ERCA) 2011, we have formed a solid group of friends and collaborators, with our own web page to post questions and opinions. I want to thank all of the members, and specially to Dinand, Madou, Jo, Alex, Camille and also to Raoul, for his love and care, and our crazy travels throughout Europe. I would also like to thank Marcelino Agúndez, Paula Carretero, Paula Jofre, Thomas Madler, their two beautiful "poussins", Luis, Elise, Khaled, Azmel and Nawras for all the nice moments in Bordeaux, from the "deutsch paella" to the incredible palestinian concerts. I am specially grateful to Coco for his sensibility and love, and the rest of the "horde de normands" who have welcomed me in their beautiful country and make

feel like being at home, I hope to count among you for the rest of my days.

Finally I would like to thank all the people who have influenced me to pursuit this career: D. Herman and Mari Mar, who discovered me the beauty of Science and Mathematics, Dr. Carlos Eiroa and Dr. Carmen Morales, who showed me the job of astronomers, my friends in UAM, ESAC, IAC and IAA, specially to Luis Gómez, Paloma, Pablo, Luis Tortosa, Pedro, Juan Pablo, Marcos, Bea, Pablo Cassatella, Diego, Dani, Javi, Silvia, Caro, Mayte, Juan, Antonio, Fra, Laura, Fer, Beto and Chevi, with whom I shared one of the happiest moments of my life; I am also grateful to the Madrigal and the Baranzano families for their love, and finally to my own family and specially to my brother who told me wonderful stories about the stars and show me the surface of the Moon for the first time.

Bordeaux, July 2013

Table of Contents

PART I.

INTRODUCTION

Chapter 1

Introduction

Radial velocity surveys have recently detected extrasolar planets with masses similar to the Earth around M-type stars, opening the interest for the study of terrestrial planets. Future missions like The James Webb Space Telescope and EChO will be able to measure infrared light curves and perform high resolution, multi-wavelength spectroscopic observations of big terrestrial planets around main sequence stars. Therefore, the study of Earth analogues is underway. Detecting and characterizing terrestrial exoplanets and their potential habitability will considerably expand the field of planetary sciences and the understanding of our own planet. This chapter place our work in context by a short introduction of the detection and the study of habitable worlds.

1.1 Terrestrial planets are common

Finding and characterizing habitable exoplanets is one of the key objectives of 21st century astrophysics. Transit spectroscopy already allows us to constrain some of the atmospheric properties of hot exoplanets such as composition (Tinetti et al., 2007), temperature structure (e.g., Knutson et al., 2008) or circulation (Snellen et al., 2010). The phase variations of the thermal emission or reflected light of hot exoplanets can be extracted from combined star+planet photometry, providing another powerful tool to characterize the climate of exoplanets. This has been achieved in transiting configurations (e.g., Knutson et al., 2007), including one terrestrial-mass planet (Batalha et al., 2011), but also for non-transiting hot Jupiters (e.g., Cowan et al. (2007)). In theory, the thermal orbital light curves of non-transiting short-period rocky planets can also be measured with combined light photometry and used to detect atmospheric species (Selsis et al., 2011) or to constrain the radius, albedo and inclination of the planet (Maurin et al., 2012). Transit spectroscopy and orbital light

curve measurements may be achievable with the *James Webb Space Telescope* or the *Exoplanet Characterization Observatory* (Tinetti et al., 2011) for a few habitable planets transiting M stars that can hopefully be found in the solar vicinity (Belu et al., 2011; Pallé et al., 2011). Exoplanet Doppler searches have revealed a high frequency of exoplanets in the $1-10\ M_{\oplus}$ mass range. Around F, G, K stars, Mayor et al. (2011) have found with HARPS a biased occurrence rate of $f = 0.41 \pm 0.16$ for these masses and orbital periods shorter than 50 days. Thus, more than one quarter of all F-G-K stars host this type of *hot super-Earth*, as they are sometimes called. For the same types of stars, orbital periods and the $1-1.8R_{\oplus}$ range (corresponding to $1-10\ M_{\oplus}$ for rocky planets), Petigura et al. (2013) find an occurrence $f \sim 17\%$ from Kepler candidates, a result that significantly departs from the estimates derived from radial velocity detections. From the HARPS survey of M stars and for the same mass range, Bonfils et al. (2013) inferred a frequency of $0.36^{+0.25}_{-0.10}$ and $0.50^{+0.52}_{-0.16}$ for orbital periods within $1-10$ days and $10-100$ days, respectively. Statistics of Kepler candidates for cool stars imply a similar frequency: 0.51 planet per star for the $0.5-1.4\ R_{\oplus}$ range and periods shorter than 50 days (Dressing & Charbonneau, 2013). Although the frequency of Earth analogues (similar mass/radius and temperature) is not yet established, the trend of finding an increasing frequency as the mass/radius decreases and the orbital period increases is extremely promising for the search and characterization of Earth-like worlds.

1.2 Infrared photometry of exoplanets

The imaging of exoplanets (at thermal or visible wavelengths) has yet been achieved only for young Jupiter-like objects (Marois et al., 2008, e.g). In all other cases, the planetary signal has to be extracted from the unresolved star+planet system. In addition to transits and eclipses when they occur, the photometric variation of a spatially-unresolved planetary system contains two superimposed signals: the intrinsic variability of the star, and the change in apparent brightness of the planet. One planetary modulation is associated with the orbital phase. This phase

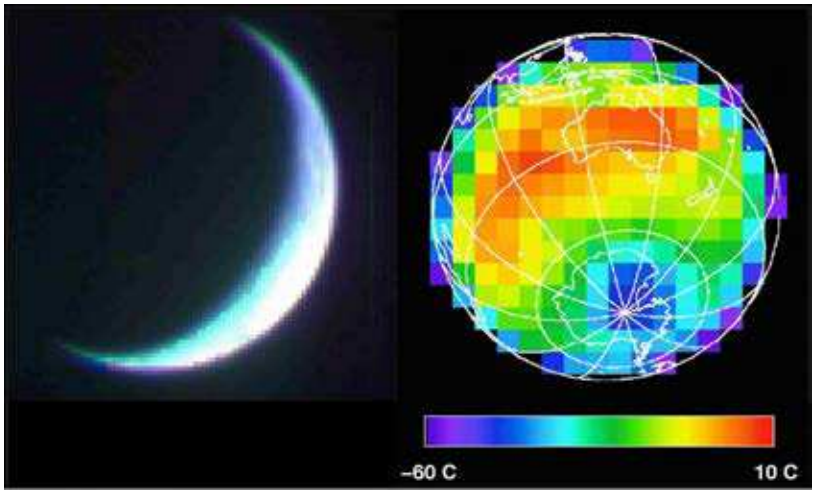

Figure 1.1 These two images were acquired at the same time by Mars Odyssey using a visible camera (left) and the Thermal Emission Imaging System (THEMIS, Murray et al. 2003). These images illustrate well what would see (without spatial resolution) the two alternative projects for Darwin/TPF: an optical choronographic single telescope observing the stellar light reflected by the planet and an IR interferometer observing the thermal proper emission of the planet. Image credit: NASA/JPL/Arizona State University.

modulation (or phase curve), which is obvious in reflected light, also exists at thermal wavelengths provided that a sufficient brightness temperature contrast exists between the day and night sides at the wavelength of the observation. Phase curves have been observed for hot Jupiters both in the infrared (Knutson et al., 2007) and in visible light (Welsh et al., 2010), for both transiting and non-transiting planets (Crossfield et al., 2010), and for eccentric planets (Lewis et al., 2013). The reflected lightcurve of Kepler-10-b, a very short-period transiting "terrestrial" planet, was obtained by Batalha et al. (2011) despite a relative amplitude of only $\sim 5 \times 10^{-6}$ (5 ppm), and the day-side emission of a similar exoplanet, 55 Cnc e was measured with Spitzer (Demory et al., 2012).

1.3 Towards habitable worlds

Observing thermal phase curves of planets smaller than 2 $R_\oplus$ will require future space observatories like JWST and EChO (Tinetti et al., 2012). Today, it may be achievable with Spitzer only for a very hot and very nearby object like 55 Cnc e. EChO aims at performing high precision spectro-photometry with an ability to detect relative photometric variations better than 10 ppm with days to weeks stability and a broad spectral coverage ($0.4 - 16$ μm). Observing phase curves to characterize low-mass exoplanets and their atmosphere is an important part of the science of EChO.

In the context of the space observatory project Darwin (Cockell et al., 2009), the measurement of broadband thermal light curves along the path of the orbit have been proposed to characterize habitable Earth-like planets and to infer the presence/absence of a dense atmosphere (Selsis, 2004). With a dense atmosphere, the temperature (and thus the thermal emission) has a much more uniform distribution over the planetary surface than without one. Especially, the day-night contrasts are considerably smoothed. Figure 1.1 shows the Earth seen in the visible and thermal infrared ranges.

In the case of a Mercury or Moon-like planet, visible and IR images would be extremely similar. As the temperatures are much higher during daytime (Mercury: $T_{\rm ss} = 700$ K, $T_{\rm night} = 150$ K; Moon: $T_{\rm ss} = 380$ K, $T_{\rm night} = 150$ K; ss: subsolar point) and, as the integrated thermal emission varies like T^4, the contribution of the night side to the global IR emission is negligible. On the contrary, planets like the Earth (or Venus as an extreme case), with a high thermal inertia provided by the atmosphere (and by the hydrosphere if there is one) and with a very efficient horizontal heat transport, have much smaller day-night differences. Therefore, the thermal flux received by the observer would not vary like the visual phase ϕ of the planet. This is illustrated by Figure 1.2.

In theory, beside revealing the presence of a dense atmosphere, orbital photometry can in theory be used to study other aspects of terrestrial exoplanets such as the

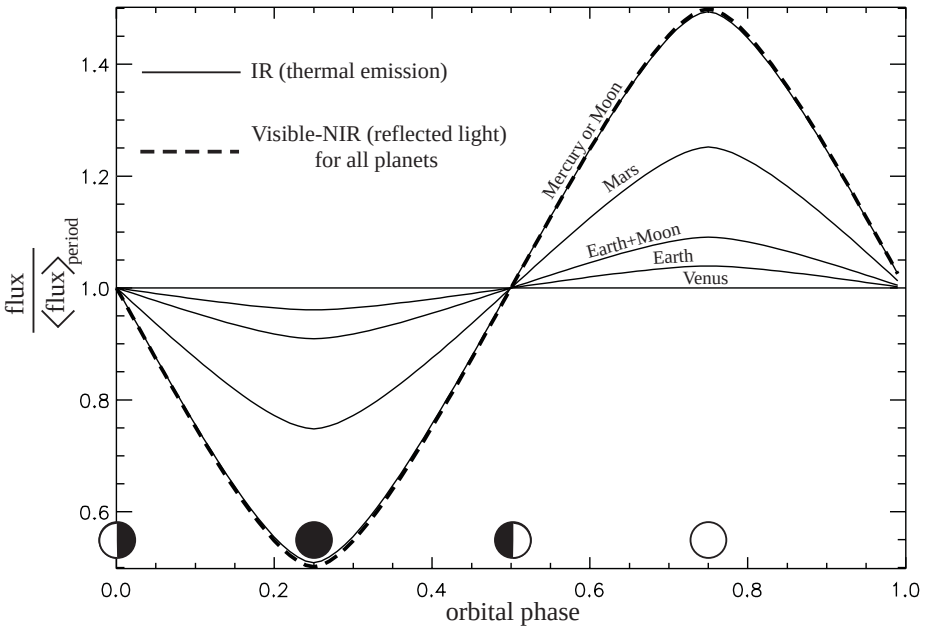

FIGURE 1.2 Variation of IR flux over an orbital period for different kinds of planets. The reflected light received from a planet is directly proportional to the illuminated fraction of the planet (visual phase:ϕ). In return, the IR emission only follows the variation of ϕ for atmosphere-less planets. In this simple model the planets have null obliquities and circular orbits seen with an inclination of 45° (from Selsis (2004)).

planet's obliquity (Gaidos & Williams, 2004), the eccentricity of the orbit (Cowan et al., 2011), or the presence of moons (Selsis, 2004; Moskovitz et al., 2009).

1.4 The Earth as an exoplanet

A broad diversity of terrestrial exoplanets is expected, in terms of bulk composition, water content, atmospheric composition, rotation, or climate, even within those called habitable due to their orbital distance compatible with the existence of surface liquid water. We do not know whether our planet is a common object, with many nearby analogues, or an exceptional and rare planet. Studying the Earth "as an exoplanet" is, however, an important step to prepare the future

attempts to characterize extrasolar habitable worlds. First, the Earth is the only habitable world we know, and it is obviously the planet whose physical, chemical and climatic properties are the most studied and characterized. However, it is necessary to understand the link between these properties and the observables, if we want to characterize Earth-like exoplanets. Furthermore, the point of view of a distant observer has never been considered until very recently, and as a consequence, we do not fully realize what properties of our planet (or another one) can be inferred from the spatially-unresolved signal and its variations.

In 1990, Sagan et al. (1993) took advantage of a flyby of the Earth by the probe Galileo on its route to Jupiter to observe our planet as an unknown world in search for biosignatures. To get a more distant point of view, several space probes like Mars Global Surveyor (Christensen & Pearl, 1997) or EPOXI (Robinson, 2011) have been used to point their instrument towards our planet and obtain high-resolution spectral data. Another way to get access to the disk-averaged Earth spectrum is to observe its reflection on the Moon. Several authors have extracted from the lunar Earthshine the spectrum of the light scattered by the Earth (from UV to near-infrared), also giving emphasis on potential biomarkers (Woolf et al., 2002; Arnold et al., 2002; Montañés Rodriguez et al., 2004; Hamdani et al., 2006; Arnold, 2008; Sterzik et al., 2012). Pallé et al. (2009) and Vidal-Madjar et al. (2010) have achieved an observation of the transmission spectrum of Earth atmosphere, similar to what can be observed during the transit of an exoplanet, by measuring the light reflected on the Moon during a Lunar eclipse.

This kind of observations are limited in terms of observation geometry and time coverage. To obtain more versatile data to predict photometric signatures requires the use of satellite observations (Atmospheric Infrared Sounder (AIRS) Hearty et al., 2009, for mid-infrared spectra) or a model (Ford et al., 2001, in the visible range), in the visible range) and often a combination of both: satellite observations can provide time dependent-maps of cloudiness that can be used to reconstruct with a radiative transfer model the disk-averaged visible lightcurves of the Earth. This was done by Pallé et al. (2008) who studied the signature of Earth rotation and weather. As a

starting point of this thesis, I adopted the same approach as in Pallé et al. (2008) but applied to the broadband thermal emission of our planet. Satellite validated data from NASA/GEWEX-SRB project (Section 3.1) provide information on the cloudiness, water vapor and thermal profile that are then used to construct time-dependent maps of the outgoing infrared emission over several decades with a 3 hrs resolution. Using a geometrical model, I use these maps to to produce infrared light curves of our planet as seen by a distant observer, and study how the photometric signatures vary with the observation geometry and their relation with the rotation seasons, geography and climate.

1.5 From Earth to Earth-like

To really understand how observables are influenced by the properties of the planet and the atmosphere and how these properties can be retrieved from the observables, it is necessary to study their variations by simulations. Models allow us to change one or a few of the properties of the planet (e.g. geography, land/ocean ratio, radius, gravity, rotation, obliquity, stellar spectrum, atmospheric pressure, atmospheric composition) and trace their influence on the observables. In particular, the use of paleoclimate models were also used to study the photometric properties of our planet in the past (Arnold et al., 2009; Sanromá & Pallé, 2012; Sanromá et al., 2013). In addition, an essential step to use climate models is the validation of the results. In the case of GCMs (3D Global Climate Models), validation is complex by the fact that these models may contain many parameterizations that were empirically tuned to reproduce some of the properties of Earth climate. Therefore, it is important to either use Earth GCMs within the range of the right conditions or to use more versatile GCMs that do not contain such empirical laws that cannot be exported to another planet. In this thesis, we have followed both approaches.

As a first approach, I have simulated the Earth using NASA SRB observations (Chapter 4), and then in collaboration with F. Codron (LMD), I have used the Earth

LMDZ GCM (Section 3.2) to simulate the Earth and Earth-like planets with slightly different conditions, while I have also used a generic version of the LMDZ model, in collaboration with B. Charnay, which allow the multiband spectral study and more exotic type of planets.

In order to validate LMDZ GCMs results to reproduce Earth-like planets, I have compared the observables obtained with the Earth LMDZ GCM with those based on NASA SRB observations (Chapter 3). Once validated, I have applied the model to simulate Earth-like worlds that differ from our planet by one or two parameters: a slowly rotating Earth, ocean-covered earths with different rotations including synchronization, and a snowball planet (Chapters 5 and 6). For all these cases, I describe the general climatic properties affected by altering these parameters, as well as the consequences on the observables, in particular the photometric variations related with rotation, seasons, phases, and weather.

In the last part, I show some preliminary results obtained at the very end of my thesis with the generic model. Thanks to the multiband treatment of the radiative transfer, this model provides use top-of-the-atmosphere flux in narrow bands from UV to the far infrared range. Therefore, we can reproduce spectra of the scattered light and the thermal emission at any time of the simulation and for any geometry, as well as synthetic multiwavelength lightcurves of Earth-like worlds. This was previously achieved with a GCM only by Showman et al. (2009) for hot Jupiters and by Selsis et al. (2011) for a hot terrestrial planet with a pure CO_2 atmosphere.

1.6 Summary

The study of the Earth-like planets is important to prepare the incoming detection and characterization of extrasolar habitable worlds. The use of climate models gives us the opportunity to built a variety of planets, by changing the planetary properties and simulating any geometry of observation, which it is important to understand their influence on the observables. In this thesis, we have used satellite and model results to simulate thermal light-curves of the Earth and several Earth-like planets, studying the climate and the circulation of the atmosphere and deriving some planetary properties

from the spectro-photometric signal, such as the planetary rotation rate, the global temperature of the planet, the existence of seasons, the eccentricity of the orbit, weather patterns or the presence of moons.

PART II.

METHODS

Chapter 2

Methods

In this chapter, we present the geometrical model used to simulate the ideal emission signal of the planet received by a distant observer at any given location, as well as the methods used to determine the global characteristics of the climate and to analyze the thermal light curve of the planet. The model transforms emission flux maps into the point-like signal of the planet and it is capable of calculating global parameters as the effective temperature or the Bond albedo to constrain the characteristics of the planetary climate. Then, we perform the analysis of the light curve obtained from the model with the aim of discussing the reliability of the parameters retrieved from the signal in each case. This chapter is organized as follows: the geometrical model is described in Section 2.1, the parameters used to typify the climate are presented in Section 2.2, and the methods of analysis of the signal are given in Section 2.3.

2.1 Geometrical Model

Our mathematical model uses a series of matrices of flux maps (emission flux as a function of longitude, latitude and time) as input data. We have used top-of-the-atmosphere (TOA) thermal emission flux maps with the purpose of building the infrared emission signal of the planet, however, other types of input data can be implemented by the model. Besides of the computation of the point-like emission from the TOA, the model can be applied to obtain global mean values as the global mean temperature at a certain altitude, the global cloud fraction, the albedo or the effective temperature, and it can also be adapted to cover specific regions of the planet. Each matrix point is defined as the mean value in the center of each grid cell, then the matrices are transformed in several steps:

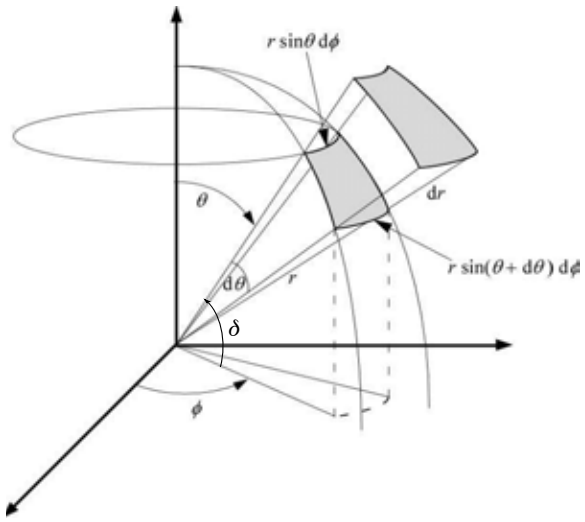

FIGURE 2.1 Spherical coordinates, where r is the radius of the sphere, θ and ϕ (longitude) are the spherical angles and δ is the geographical latitude.

i) Spherical maps.– According to the space resolution, the data matrices are converted into spherical maps by a transformation of the area $S_{i,j}$ of each grid cell. Defining $dS_{i,j}$ as the spherical elementary area (Fig. 2.1), $S_{i,j}$, the area of each grid cell can be calculated as:

$$\overrightarrow{dS}_{(i,j)} = R^2 \sin\theta \, d\theta \, d\phi \cdot \hat{r} \tag{2.1}$$

$$S_{i,j} = \int R^2 \cos\delta \, d\delta \, d\phi \tag{2.2}$$

$$S_{i,j} = R^2 \cdot (sin\delta_{i+1} - sin\delta_i) \cdot (\phi_{j+1} - \phi_j) \tag{2.3}$$

where (δ_i, δ_{i+1}) and (ϕ_j, ϕ_{j+1}) are the latitude and longitude limits of the each grid cell. For further calculations, we define the magnitude $a_{i,j}$, the unitary elementary as:

$$a_{\mathrm{i,j}} = (sin\delta_{i+1} - sin\delta_i) \cdot (\phi_{j+1} - \phi_j) \tag{2.4}$$

ii) Planetary position.– The position of the planet in the orbit is specified by the date, whereas the time is given either in Universal Time (UT) or by the location of the sub-stellar point, that can be obtained from the ephemeris. The

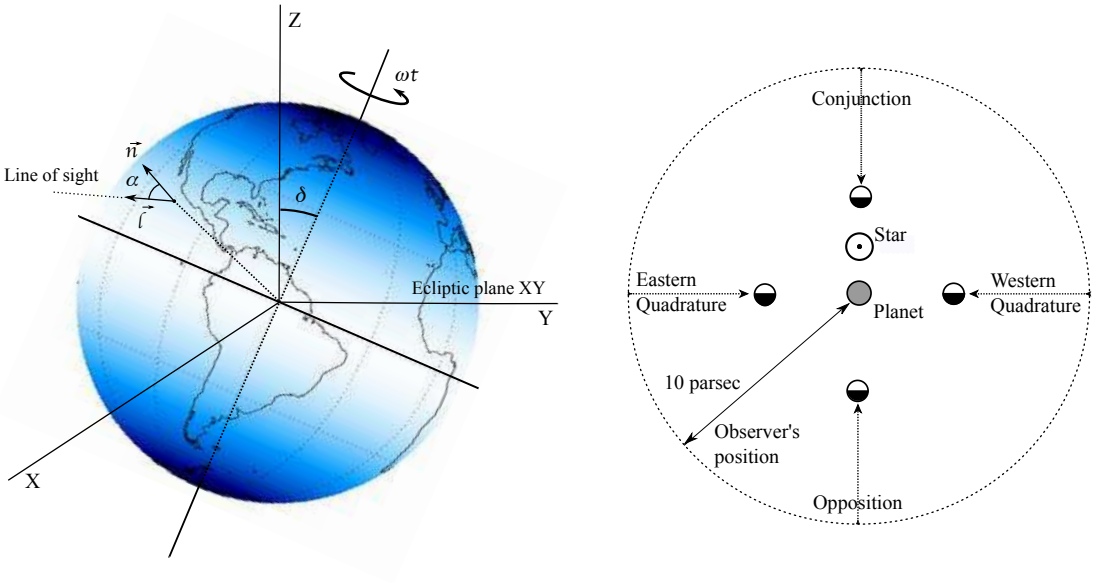

Figure 2.2 *Left:* Planetary configuration. *Right:* Schematic positions of the observers respect to the planet at the initial time: opposition, western quadrature, conjunction and eastern quadrature. The correspondent planetary phase seen by the observer is shown at the tip of the arrow pointing from the observer's position to the planet.

ephemeris implemented in the model are taken from the Jet Propulsion Laboratory (JLP) Horizons Ephemeris System, that adjusts the equations of motion to highly accurate measurements of planetary positions[1].

iii) Observer's position.– The coordinates of the observer are defined by the position of the sub-observer's point and the distance to the planet. To illustrate several simultaneous planet-observer geometries, we have defined observer positions by equatorial coordinates at a radius distance of 10 pc. In order to interpret the variation of the Earth emission in relation with the geographic features and the climate, it is relevant to locate the sub-observer point by its geographic coordinates: the equivalent of the declination angle on the planetary surface gives the latitude

[1]http://ssd.jpl.nasa.gov/?horizons

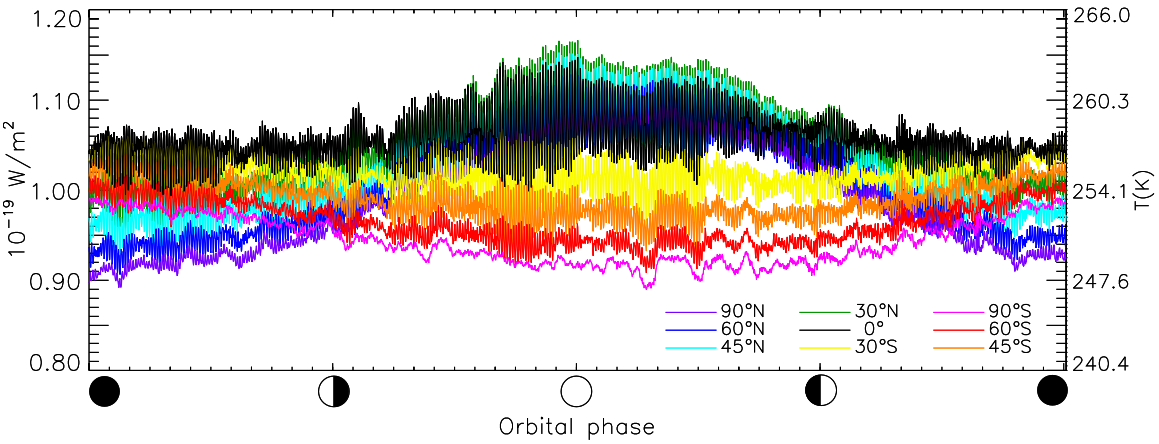

FIGURE 2.3 Earth orbital light curve. The colours indicate the latitude of the sub-observer point and the orbital phases correspond to an equatorial observer at opposition during northern winter (black line).

of the sub-observer point, which remains constant along the orbit. The latitude remains constant with time because precession and nutation are negligible during an orbit, and its longitude ϕ varies with time as $\phi(t) = \phi(t_0) - \omega t$, ω being the rotation rate of the Earth (with the exceptions of the polar cases where the planetary geometry does not change with time); therefore, we can define the sub-observer point by its latitude and its longitude at a given time.

The initial time is set to January 1, 0:00 UT of the year considered, then we use four different initial longitudes $\phi(t_0)$: the meridian of the sub-stellar point, the morning terminator, the meridian of the anti-stellar point and the evening terminator. We call these initial observing geometries conjunction (C), western quadrature (WQ), opposition (O) and eastern quadrature (EQ), respectively, although these terms should normally apply exclusively to an observer located in the ecliptic plane. Figure 2.2 represents a simplified scheme of the observers's positions used in this work. Previous studies ([e.g] Cowan et al. (2012)) define the planetary position in the orbit respect to the observer according to an inferior planet configuration. Because our study compares different views of the planet at the same moment, we have preferred to use an equivalent notation: we define

the observers's positions after a superior planet configuration. At the initial time, opposition designates an observer placed at a phase angle $\gamma = 180^o$, being midnight at the planetary disk Central Meridian (CM). An the observer is at conjunction when the planetary phase angle is $\gamma = 0^o$ (midday at CM). And therefore, western quadrature and eastern quadrature correspond to positions at $\gamma = 270^o$ and $\gamma = 90^o$, respectively. As the planet orbits around the star, its phase angle respect to the observer changes. For this matter, each observer is named after the position they have respect to the planet at the initial time of observation. In summary, the observers are placed respect to the equatorial plane, the sub-observer position over the planet is specified by the latitude of the sub-observer's point and by local hour at the CM.

It is important to note two facts: firstly, each observer sees the planet at a certain local hour during a whole rotation period, and secondly, observers placed at the same latitude but different longitudes see the same region of the planet at different local hours (i.e. if the (O) observer sees a given region of the planet during the winter midnight and the summer noon, the (C) observer sees the same region during the winter noon and the summer midnight). There is an exception for the polar views, where the observer sees the same hemisphere of the planet along the time of observation. In the need of a reference for time for this case, we define the "local hour" at a polar latitude according to the Universal Time (UT). In this case, the seasonal variability and the diurnal variability (daily change in temperature in a certain region) produce the variation of the signal and not the changing of the planetary view (rotational variability).

iv) Point-like signal.– In general, the flux received at a distance d is related to the flux emitted by the source as $F_{obs}(t) = \frac{R^2}{d^2} F_e$, where R^2 is in this case the radius of the planet. Specifically, at any moment, the planetary disk towards the observer is determined by the sub-observer point and the contribution of each point to the total flux is given by the Lambert's cosine law (Eq. 2.5) as the projection of the specific intensity of radiation into the direction of the observer, $I_r \cos \alpha_{i,j}(t)$, where $I^r_{i,j}$ is the specific intensity of radiation normal to the emission surface and $\alpha_{i,j}(t)$ is the angle between the surface normal and the observer's line of sight at

a time t. The cosine of this angle is calculated at any time by the dot product between the normal to the surface and the sub-observer's point vector, where the latter is defined by its geographical coordinates, as previously mentioned (Fig 2.2):

$$F_{i,j}(t) = \int I^n_{i,j} \cos\alpha_{i,j}(t)\, \mathrm{d}\Omega \tag{2.5}$$

In the model, the flux $F_{obs}(t)$ received at a distance d and at a time t is given by the sum of the contribution of each cell (i, j) in the solid angle towards the observer by:

$$F_{\mathrm{obs}}(t) = \frac{1}{d^2} \sum_{i,j} \left[a_{i,j} \cdot \cos\alpha_{i,j}(t) \cdot \left(\frac{F_{i,j}(t)}{\pi} \right) \right], \tag{2.6}$$

where $a_{i,j}$ is the area of each grid cell (Eq. 2.4), $F_{i,j}(t)$ is the emission flux value of each grid cell and $F_{i,j}(t)/\pi$ is the correspondent specific intensity in the Lambertian approximation. As a result, a flux time series is obtained with the time resolution of the input sequence.

v) Limb Darkening.– In order to convert the TOA flux into the disk-integrated flux received by a distant observer, we have previously assumed an isotropic (Lambertian) distribution of specific intensities at the TOA. The Lambertian emission is only dependent on directionality by the $\cos\alpha$, being α the viewing angle respect to the surface normal (Eq. 2.6). However, the specific intensities are not isotropic, but they produce a darkening or brightening effect towards the limb of the planetary disk depending on the thermal structure, the composition of the atmosphere, the emission wavelength and the geometry of observation. The deviations from the isotropic case can be classified into four components:

a) Horizontal inhomogeneities produced by the variation of the nature of the source and its emissivity. For instance, a parcel of desert emits more energy than the same area of ocean.

b) Vertical variations are related to the temperature profile and to the extinction of the atmosphere. In the first case, the contribution function that depends on the

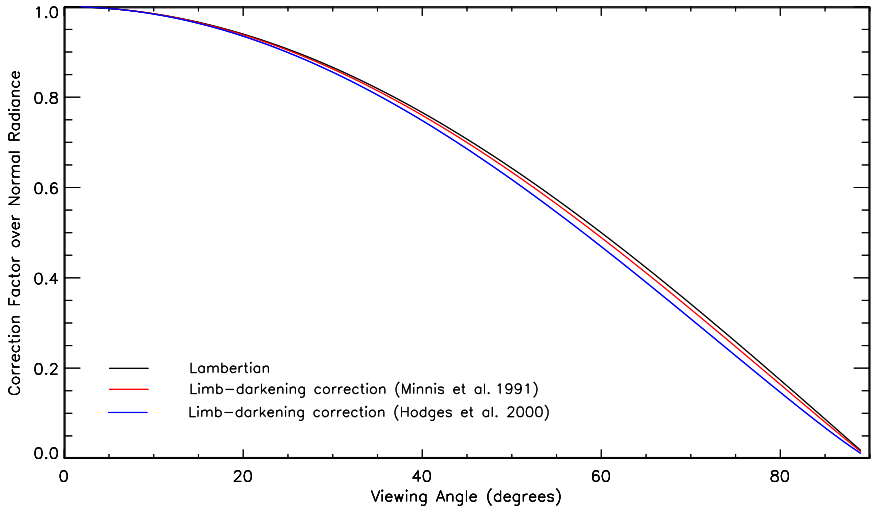

FIGURE 2.4 Correction factor L(α): radiance over normal radiance. Comparison between the Lambertian emission (black), the mean limb-darkening correction from Minnis et al. (1991) (red) and from Hodges et al. (2000) (blue).

wavelength band of observation, indicates the height of the emission layer in the atmosphere. In the second case, the emission is scattered and absorbed by the air mass along its path, depending on the emission wavelength and on the components of the atmosphere (aerosols, H_2O, O_2, etc.). Smith et al. (1994) studied the limb darkening in the broadband of (5-50) μm using the scanning radiometer data of the Earth Radiation Budget Experiment (ERBE)[2], reporting a limb brightening for winter polar nights as a result of night-time atmospheric temperature inversion.

c) Temporal fluctuations are produced by the daily and seasonal changes in the atmospheric profile and by the presence of clouds that partially absorb the radiation. Brooks & Fenn (1989) observed a difference between the daytime and the night-time limb-darkening, which is amplified in the case of surfaces with large diurnal temperature cycles (i.e Sahara desert). This effect also changes along the year. Peculiarly, the fluctuations are less marked during summer than during winter, being

[2]http://science.larc.nasa.gov/erbe/

specially stronger for the Northern Hemisphere over the Southern one. This result is explained by the fact that during summer, the large water vapor contain and the convection clouds in the atmosphere mask the strong diurnal temperature cycle of the surface. This behavior is amplified during the Northern summer because the large masses of land produce higher temperatures and therefore a larger fraction of convection clouds.

d) Angular variations are due to the directionality of both the emission and the extinction. The light from the limb of the planetary disk suffers a larger atmospheric absorption as it travels a longer path through the atmosphere than in the normal direction. Limb-darkening is also produced by geometric effects dependent on the position of the observer, for instance in a cloudy day, there is a higher probability of seeing the surface at nadir and the cloud tops at the limb.

The attenuation of the emission towards the limb of the planet is the result of the combination of these four effects. In the case of the Earth, the resemblance of limb-darkening parameterizations for specific conditions of the atmosphere, allows to built several mean models by averaging over latitude, time and surface types. The models establish a correction factor $L(\alpha)$ over the radiance normal to the surface in function of the viewing angle:

$$I(\alpha) = I_n \cdot L(\alpha) \tag{2.7}$$

where α is the viewing angle respect to the surface normal and I_n is the radiance at normal. Minnis et al. (1991) derived the empirical function:

$$L(\alpha) = \begin{cases} 1 & \text{if } \alpha < 11^\circ \\ b + a \ln(\cos\alpha) & \text{otherwise} \end{cases} \tag{2.8}$$

where $a = 0.03247$ and $b = 1.000602$. However Hodges et al. (2000) find that this correction is not sufficient, probably due to the lack of clouds or aerosols in the radiative models used for the numerical calculation and gives a correction with

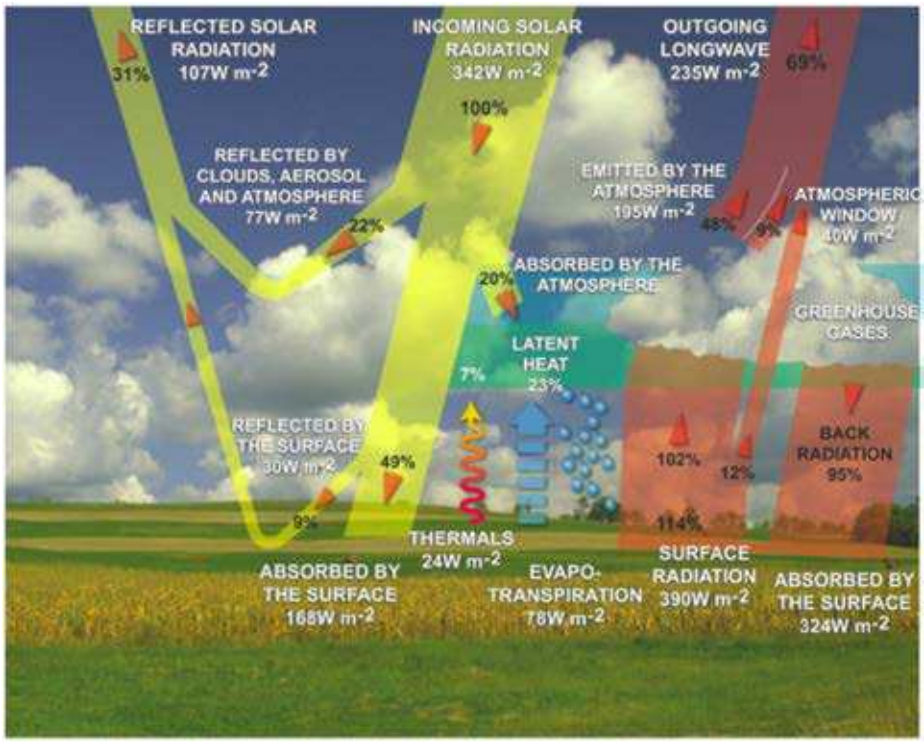

Figure 2.5 Earth radiation budget scheme.

$a = 0.09$ that it is in agreement with satellite measurements by GMS-4 and GOES-7. Figure 2.4 compares the Lambertian factor applied in this work and the correction factor for the mean limb-darkening models previously mentioned. Finally we have found that the limb-darkening corrections produce an attenuation of only (1.5±0.02)% for the model of Minnis et al. (1991) and an attenuation of (4±0.1)% for the model of Hodges et al. (2000) over the point-like signal derived by a Lambertian approximation. Thus, we conclude that the Lambertian approximation is valid to model the thermal point-like signal of an Earth-like planet.

2.2 Climate parameterization

2.2.1 Radiation Budget

The climate of an Earth-like planet is governed by the temperature of the surface, the atmosphere and the oceans, which in turn depend on the balance of energy fluxes. Considering the atmosphere as a whole, we can express the radiative balance equation as the equilibrium between the energy absorbed and the energy emitted by the planet.

The most fundamental sources of energy are the absorption of stellar radiation and the gravitational energy produced by the cooling of the planet, however this latter is negligible before the incoming energy from the star. The Solar mean radiative flux at Earth' distance is termed by the Solar constant $F_{\odot} = L/4\pi d_P^2 = 1366$ W/m^2, where L is the solar luminosity and d_P is the mean distance between the planet and the star (1UA), the actual flux varies along the seasons due to the eccentricity of the orbit. The mean incoming radiation is defined by the energy received by the illuminated side of the planet, which can be approximated by a disk of area πR_P^2. Planets do not behave like perfect blackbodies but they reflect part of the incoming energy. The ratio between the incoming and the reflected energies is represented by the Bond albedo A. The outgoing flux is expressed as the emission of a blackbody that radiates at the equilibrium temperature of the planet, also called effective temperature T_{eff}:

$$\pi R^2 (1 - A) F_S = 4\pi R^2 \sigma T_{eff}^4 \tag{2.9}$$

where R is the radius of the planet, σ is the Stefan-Boltzmann constant. In the case of the Earth, T_{eff} is $\simeq 255$ K and the emission of a blackbody at this temperature has a maximum at 11 μm which lies in the thermal (or longwave) infrared range (Fig 2.6), whereas the Sun emits primarily in the shortwave range (0.1- 5.0 μm). The effective temperature of the planet differs from its mean surface temperature ($T_S \simeq 288$ K), because of the action of the atmosphere. This effect, known as the greenhouse effect, works as follows: first, the radiation emitted by the surface is partially absorbed by the atmospheric compounds such as water vapor and carbon dioxide, and then these species warm up and re-emit the radiation to the atmosphere, warming the air around them. This mechanism is responsible of the temperature

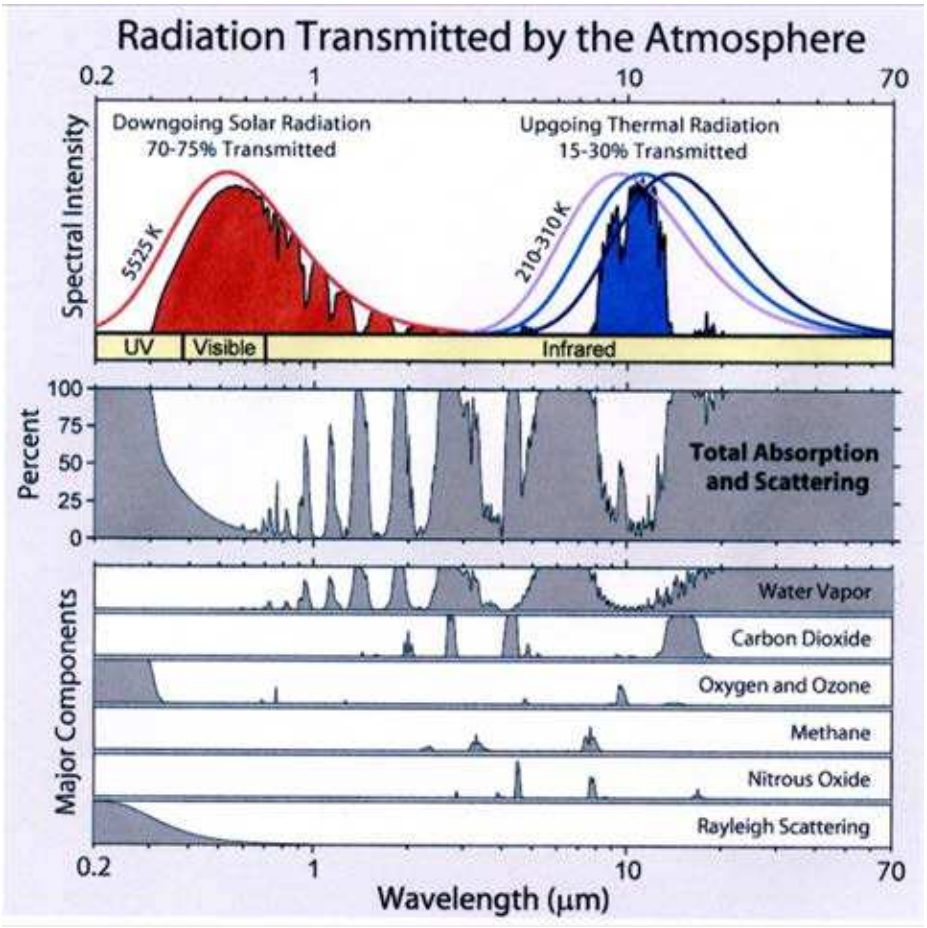

Figure 2.6 Transmittance of the Earth atmosphere and contributions of greenhouse gases. From Vázquez et al. (2010).

difference by trapping part of the infrared radiation in the atmosphere. It is termed by greenhouse parameter as:

$$\sigma T_{eff}^4 = (1-g)\sigma T_S^4 \tag{2.10}$$

Figure 2.6 illustrates the atmospheric transmittance of the atmosphere and the contribution of the most relevant greenhouse gases. We can see that water vapor is

responsible of most of the energy absorption and are a key factor in the study of the thermal emission of Earth-like planets. In the model, H_2O clouds are classified in two main groups depending on their response to radiation:

i) Low-level clouds are formed by water droplets and their bases lie below 2 km. They have a mean temperature at the top of $\simeq$ 280 K, a high optical depth in the shortwave range (4.7 at 0.6 μm), and a mean surface coverage of $\simeq$ 40 %.

ii) High-level clouds are formed by ice-crystals and lie above 6 km. They have a mean temperature at the top of $\simeq$ 227 K, a low optical depth in the shortwave range (2.2 at 0.6 μm), and a mean surface coverage of $\simeq$ 15 %. We have also included in this group vertically developed clouds. Although, they are formed mainly at low latitudes from thermal convection or frontal lifting, accumulating large amounts of energy through the condensation of water vapor, they can grow up to 12 km, thus they present similar properties to high clouds, having very cold cloud tops and absorbing most of the energy from below.

Low-level clouds have a pronounced effect in the planetary albedo, because of their large coverage fraction and high optical depth, they reflect 90 % of the incident solar energy and as a consequence the atmosphere below them is colder. At the same time, they re-emit the energy from the surface upwards at their top temperature, which does not differ considerably from the surface temperature, and they have a negligible greenhouse effect. On the contrary, high-clouds are not relevant to the albedo of the planet but have an important role on the greenhouse effect, they do not emit much radiation upwards as their cloud tops are very cold, then as a result, they block the surface emission, warming the atmosphere below them (Kitzmann et al., 2010, 2011).

Our aim is to infer certain characteristics of the planet from its thermal light curve. The brightness temperature of the planet can be determined from the thermal emission of the planet received by a distant observer ([e.g.]Gaidos & Williams (2004); Moskovitz et al. (2009); Cowan et al. (2012)): the flux F_e from a planetary disk can

be obtained by the integration of the Planck's law in the spectral band and in the solid angle of the observation:

$$F_e = \int_{\lambda_a}^{\lambda_b} \int_h B_\lambda(T_b)\, \mathrm{d}\Omega \tag{2.11}$$

where B_λ is the Planck's law, λ_a and λ_b are the limits of the spectral band, $d\Omega$ is the solid angle and h denotes the hemisphere exposed. As our spectral band of observation (5-50 μm) covers the whole emission of the planet, we can suppose the TOA-flux is bolometric and relate it to the global T_{eff} by $F_e \simeq \sigma T_{eff}^4$. Finally, the effective temperature of the planet is obtained relating Equation (2.11) with Equation (2.6) that relates the flux emitted by the planet with the flux received by the observer. Once the effective temperature is determined from the flux received and knowing the star incident flux at the mean planetary distance, the albedo (A) can be obtained from Eq. 2.9.

In addition, we can use the model information to derive some characteristics of its climate. The normalized greenhouse parameter g_N accounts for the fractional part of the thermal radiation that is absorbed and re-radiated back by the atmosphere, it depends on the wavelength range and on the difference between the mean surface flux obtained from the model and the mean TOA all-sky flux, supposing the flux is bolometric:

$$g_N^\lambda = \frac{F_s^\lambda - F_{TOA}^\lambda}{F_s^\lambda} \simeq \frac{\sigma T_{sur}^4 - \sigma T_{eff}^4}{\sigma T_{sur}^4} \tag{2.12}$$

where T_{sur} is the surface temperature, that is determined from the GCM data. The Cloud Radiative Forcing (CRF) quantifies the thermal emission absorption by the clouds. It is given by the difference between the emission for average conditions ($F_{all-sky}$) and cloud-free conditions (F_{clear}) at TOA:

$$CRF = F_{all-sky}^{TOA} - F_{clear}^{TOA} \tag{2.13}$$

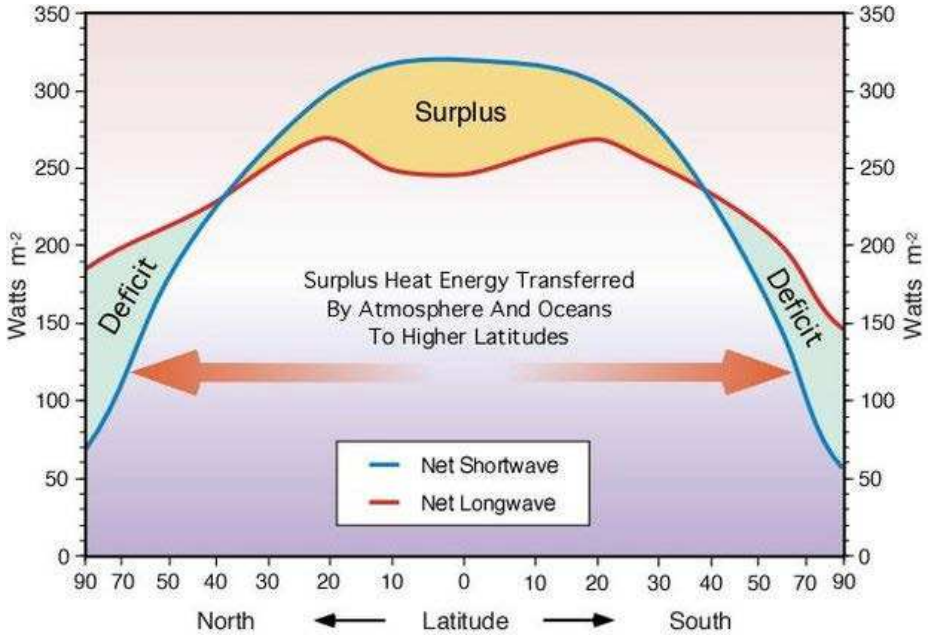

FIGURE 2.7 Earth net heat transport. The relations between the incoming (shortwave) radiation and the emitted (longwave) energy produce a net transport of heat.

In Section 5.2 and Section **??**, we have calculated T_{eff}, T_S, g_N, A, and CRF for our set of terrestrial planets and water worlds respectively, in order to typify the variety of their global properties and climates.

2.2.2 Circulation of the atmosphere

The incoming radiation is not the same for every point of the planet but it depends on the angle of incidence of the solar rays. Because of the sphericity of the planet, high latitudes receive less energy than low ones. There is also an insolation variation along the orbit, produced by the obliquity of the planet. In the case of the Earth, the rotation axis is tilted 23.5° respect to the normal to its orbital plane. For this reason, the subsolar point is not fixed at the equator along the orbit, but it moves inside the intertropical band, 23.5° north and south the equator, producing the seasons. The track followed by the subsolar point during one rotation is called thermal equator and

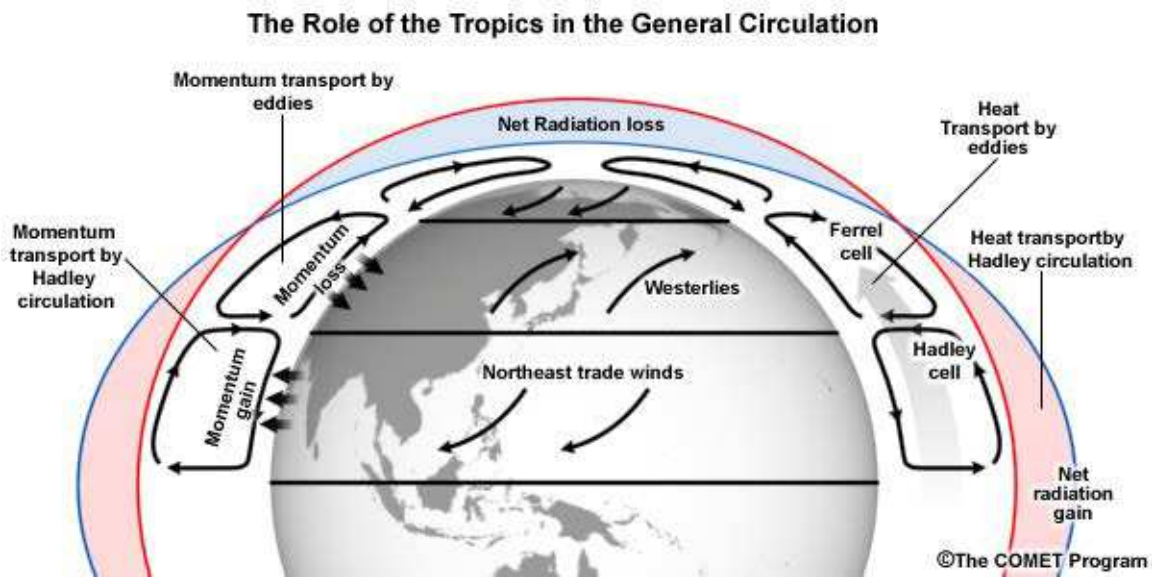

Figure 2.8 Earth atmospheric circulation and heat transport.

it is the place where the main circulation patterns of the atmosphere converge. The latitudinal variation on the energy over the planet is one of the main agents of the atmospheric circulation (along with the rotation rate, Section 2.2.3). The tropics, the region below 23.5° latitude, receive and emit more radiation than the poles, however the relation between the incoming and the outgoing energy is different, there is an excess of heat in the tropics and a deficit in the poles, as it is shown in Figure 2.7. As a consequence of this temperature gradient, heat is transported polewards by three main mechanisms:

i) Large scale circulation of the atmosphere.– In the case of the Earth, three latitudinal air cells are stablished in each hemisphere (Fig 2.8), the Hadley cell (0°-30° latitude), the Ferrel cell (30°- 60°) and the Polar cell (60°- 90°) . The Hadley cell is the most important circulation pattern, some slow rotating bodies, such as Venus and Titan, exhibit a single large cell in each hemisphere. On the contrary, in Earth, the Hadley cell extends from the thermal equator to 30° latitude. At the thermal equator, warm moist air rises to the tropopause creating a cloudy band called

Intertropical Convergence Zone (ITCZ), then the air is carried poleward and descends at about 30° latitude, part of the air moves back to the equator at the surface level creating the trade winds. The Ferrel Cell is not a closed loop driven by convection currents, but it is the result of the eddy circulations (high and low pressure regions) of the mid-latitudes, it extends from the 30° to 60° latitude and acts as a zone of mixing between the Polar and the Hadley cells. At 60° latitude in the polar cell, the air is moist and warm enough to be risen to the top of troposphere again and carried poleward, it descends at the cold and dry conditions of the polar latitude, and then finally it is driven southwards by the polar easterlies.

ii) Large scale circulation of the oceans.– In the oceans, the circulation is divided in two types of currents, surface currents and deep currents. Surface currents are driven by winds and modified by the Ekman transport, by which the direction of the ocean current is deflected in an angle to the stress of the wind, dependent on depth. The deep currents, as the thermohaline circulation, are slow and depend on temperature and salinity gradients.

iii) Weather systems.– Low-pressure areas, specially tropical cyclons, accumulate and transport latent heat.

2.2.3 The effect of rotation on the atmospheric circulation

The rotation rate of the planet has a major role in the circulation patterns of the atmosphere (Section 5.1): larger rotation periods produce a large meridional scale of the stationary wave that produces equatorial jets (Edson et al., 2011), and slow rotating planets, like Venus and Titan exhibit superrotating winds. At superrotating regimes, the zonal wind has a greater angular momentum than the correspondent solid-body, instabilities in the mid-latitude jets produce planetary scale waves that transport angular momentum from this region to the equator, where they maintain a superrotating flow. In general, the phenomenon appears in a band at the equator and becomes inertially unstable at higher latitudes, depending on the rotation rate of

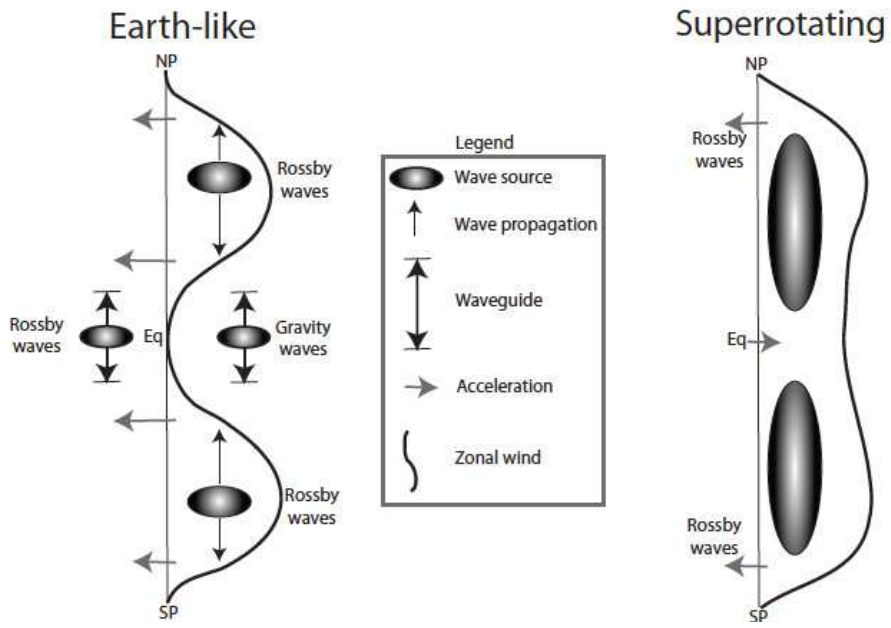

Figure 2.9 Schematic representation of eddy-mean-flow interaction in the Earth (left) and in a superrotating regime in Titan (right). From Mitchell & Vallis (2010).

the planet. Earth's troposphere does not show superrotation as it has easterly winds at the equator.

A mechanism that may lead to a superrotating state is a meridional transport of angular momentum to the equator by Rossby waves. A characteristic of these waves is that the momentum is transported in the opposite direction of their group velocity and may produce superrotation under certain conditions (Figure 2.9). In the Earth, Rossby waves are small, propagate from mid-latitudes towards the equator, then they break, decelerating the equatorial flow, and produce the easterly winds. However in the superrotating case, the scale of the baroclinic instability becomes larger than the planetary radius, a global disturbance is produced providing an eastward momentum at the equator that accelerates the zonal wind and as a result the superrotating westerly winds are generated (Mitchell & Vallis, 2010).

We evaluate three criteria to characterize superrotation on Earth-like planets:

i) The thermal Rossby number Ro_T.– A first criterion is to estimate the thermal Rossby number Ro_T, that express the force of the westerly wind as the balance between the inertial force due to the thermal (zonal) wind and the Coriolis force:

$$Ro_T = \frac{U_T}{2\Omega_r R_P} = \frac{R_{sp} T_S \Delta_T}{(2\Omega_r R_P)^2} \tag{2.14}$$

where U_T is the zonal wind velocity, Ω_r is the rotation rate of the planet, R_P is the radius of the planet, R_{sp} is the specific gas constant of dry air, T_S is the mean surface temperature, and $\Delta_T = 1. - T_{pole}/T_{equator}$ is the fractional meridional temperature gradient. Mitchell & Vallis (2010) show that the superrotation regime in Earth-like atmospheres arises when $Ro_T > 1$, although the superrotation and non-superrotating co-exist at Ro_T=1.3.

ii) The zonal wind velocity u_L.– A second method to evaluate superrotation is to calculate the condition of the zonal wind velocity to be in a superrotation state. Being $M_0 = \Omega R^2$ the angular momentum at the equator, in general using the thin shell approximation the zonal wind will at a certain latitude δ have an angular momentum M:

$$M = \Omega_r R_P^2 \cos^2 \delta + u R_P \cos \delta \tag{2.15}$$

A superrotating regime implies $u > u_0$, and then threshold zonal wind speed u_L is stablished as:

$$u_L = \frac{\Omega_r R_P \sin^2(\delta)}{\cos \delta} \tag{2.16}$$

iii) The Equatorial Rossby deformation length l_R.– A third parameter to delimit superrotation regimes is the Rossby radius of deformation, which gives us the length scale at which the effects of stratification and rotation balance under geostrophic

conditions (Coriolis and the horizontal pressure gradient forces are in equilibrium):

$$l_R = \frac{NH}{f} \tag{2.17}$$

where N is the Brunt–Väisäla frequency, H is the scale height, f is the Coriolis parameter, which can be written in terms of the rotation rate Ω_r and the latitude θ as $f = 2\Omega_r sen\theta$. Following the β-plane approximation, near the Equator f can be expressed as $f = f_0 + \beta y$, where $\beta = 2\Omega_r(cos\theta)/R_P$ and R_P is the radius of the planet, and the Rossby radius of deformation is given by (Chelton et al., 1998):

$$l_R = \sqrt{\frac{NH}{2\beta}} = \sqrt{\frac{NHR_P}{4\Omega_r}} \tag{2.18}$$

We can also define a dimensionless equatorial Rossby deformation length by comparing l_R with the radius of the planet:

$$L_R = \frac{l_R}{R_P} = \sqrt{\frac{NH}{4R_P\Omega_r}} \tag{2.19}$$

where R_P is the planetary radius. According to del Genio & Suozzo (1987), superrotation develops when the length scale of the perturbation, which is proportional to the Rossby deformation radius, is greater than the radius of the planet ($L_R > 1$).

The Earth's atmosphere can be considered as a dry stably stratified atmosphere up to 10 km, corresponding to the extension of the troposphere. The Brunt–Väisäla frequency is given by:

$$N^2 = \frac{g}{T}\left(\frac{g}{c_p} + \frac{dT}{dz}\right) \tag{2.20}$$

where c_p is the heat capacity of the air at constant pressure. Assuming a lineal atmosphere $T(z) = T_0 - az$, where $a = -dT/dz$ is the lapse rate, and replacing the scale height by $H = RT_S/m_a g$, where R is the ideal gas constant, T_S is the mean surface temperature, m_a is the molecular mass of the air, and g is the gravitational acceleration, L_R can be written as:

$$L_R = \sqrt{\frac{R}{4R_P\Omega_r m_a}\left(\frac{g}{c_p} - a\right)} \tag{2.21}$$

where the lapse rate a is obtained by integrating the barometric formula for a lineal atmosphere:

$$a = \frac{-g \ln (T_z/T_0)}{R \ln (p_z/p_0)} \tag{2.22}$$

where p_0 and T_0 are the surface pressure and temperature, and p_z and T_z are the pressure and temperature at an altitude z.

This three criteria are considered in Section 5.2 (Table 5.3) and Section 6.2 (Table 6.3) in order to identify superrotation regimes in our set of Earth-like planets.

2.3 Analysis of the signal

The analysis of the time series is done in three steps: the study of the origins of the variability of the signal (diurnal cycle, rotational movement, seasonality, weather patterns, etc...) according to the planetary characteristics; the retrieval of the rotation period by autocorrelation and the analysis of the average rotation light curves. The first is explained with the results in Section 4.2 for the Earth (NASA-SRB data), in Section 5.3 for the set of terrestrial planets, and in Section 6.3 for the set of aquaplanets. Here we explain the method of autocorrelation and the construction of the longitudinal curves.

2.3.1 Autocorrelation

The analysis of the cross-correlation of the time series with itself or autocorrelation, shown in Figure 2.10 (left), is a technique that allows to determine the rotation period of the planet and the lifetime of the cloud structures. The autocorrelation A can be computed as:

$$A(L) = \frac{\sum_{k=0}^{N-L-1} \left(F(k\Delta t) - \overline{F}\right) \left(F((k+L)\Delta t) - \overline{F}\right)}{\sum_{k=0}^{N-1} \left(F(k\Delta t) - \overline{F}\right)^2}, \tag{2.23}$$

where L is the time lag in number of 3 hr points, N is the total number of points in the time series, and $\overline{F}$ is the mean flux. The autocorrelation is maximum

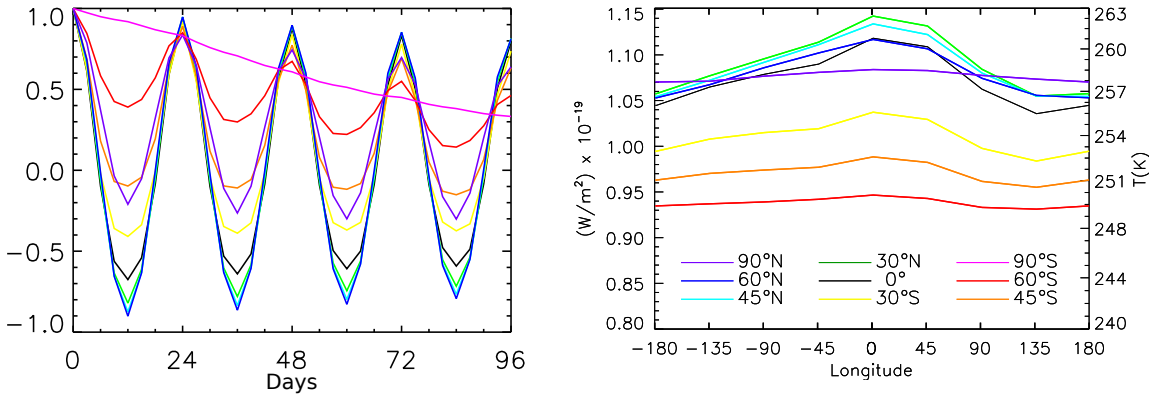

Figure 2.10 *Left:* Autocorrelation of the time series in Fig. 2.3 during northern summer. *Right:* Correspondent rotation light curve. Colours correspond to the latitude of the sub-observer point.

when values are similar within a time lag distance and it is sampled according to the time resolution. This method was chosen before the Fourier Transform to avoid the harmonics of the rotational period. The duration of the statistically significant peaks in the autocorrelated time series can give us an estimation of the lifetime of the cloud structures, typically of around one week for Earth clouds (Pallé et al., 2008).

The use of this method is limited by three factors: the number of periods contained in the series, the time resolution, and climatic effects over the signal. In order to get good statistics on the results, the observation needs to cover a large number of periods. It is also important to have an adequate time resolution to obtain a good sampling of the periodicity, if the latter is not a multiple of the time resolution, there is a longitudinal angle phase $\Delta\phi$ between the real period and the measured period that is cumulative over time, and as a consequence, the longer the time considered, the worser the autocorrelation. Some climate effects, as the seasonal flux change or the random effect of clouds, have an influence on the autocorrelation function and they are also cumulative. In our case we have made the best compromise between these factors and found that the most accurate results are obtained with a length of the series of $\sim$10 days. The autocorrelation of the Earth (NASA-SRB data) is

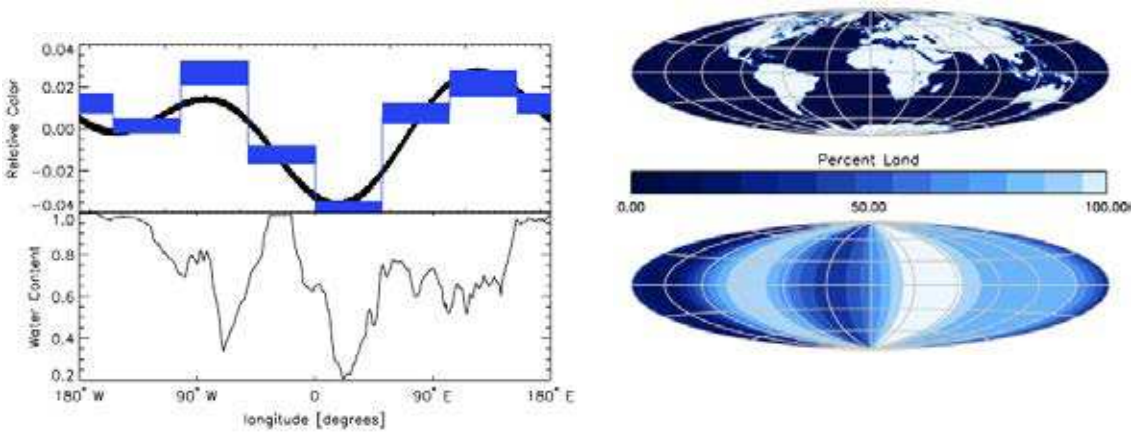

FIGURE 2.11 *Left:* Longitudinal curves of the oceanic distribution on Earth: N-slice model (blue) and sinusoidal (black) for June EPOXI simulations (top panel) and MODIS cloud-free, equator weighted observations (bottom panel). *Right:* Land distributions for a MODIS map (top panel) and an June EPOXI longitudinal map. (From Cowan et al. 2009).

discussed in Section 4.3 (Fig. 4.3) and the results for our set of planets (LMDZ data) are presented in Section 5.4 (Table 5.5) and Section 6.4 (Table 6.5).

2.3.2 Rotation light curves

Once the rotation period is identified, the observer can produce a typical rotation light curve by folding the time series obtained during weeks or months over the rotation period Figure 2.10 (right). The average flux obtained at each fraction of the period, according with the time resolution of the data, constitutes the points of the final rotational light curve. This process averages out the random cloud variability, the effect of the clouds disappears averaging over long periods of time whereas the strongest features of the emission prevail. The observer can plot this average rotation light curve as a function of an arbitrary longitude (in our case the longitude that we have chosen is the conventional geographic longitude for commodity), and the shape of this rotational light curve can then reveal brighter/fainter areas of the planet

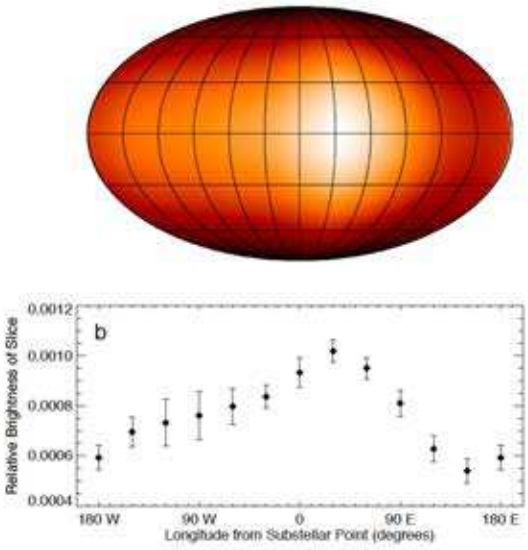

FIGURE 2.12 A map of the day-night contrast of the extrasolar planet HD 189733b (from Knutson et al., 2007).

distributed in longitude. Several authors (Rutten, 1996; Knutson et al., 2007; Cowan & Agol, 2008; Cowan et al., 2009) have reproduced exoplanet longitudinal maps by similar methods (Figure 2.12). We present the longitudinal light curves of the Earth (NASA-SRB data) in Section 4.4 (Fig. 4.3 and Fig. 4.4), those of our set of terrestrial planets in Section 5.5 (Fig. 5.18), and those of our set of aquaplanets in Section 6.5 (Fig. 6.12).

2.4 Summary

We have built a geometrical model that can simulate the point-like emission signal of an Earth-like planet received by an observer at any geometry and distance. By the comparison of mean limb darkening models and for the sake of simplicity we conclude that the Lambertian approximation is applicable on the simulation of the thermal emission of the Earth-like planets of our set. Our model can also calculate the global characteristics of the planet as the effective temperature, the Bond albedo,

the greenhouse parameter, or the cloud radiative forcing to study the climate and to analyze the influence of the variation of these parameters on the signal. In addition, by the further analysis of the light curves, we can retrieve certain parameters such as the rotation rate, the albedo and the effective temperature. We can also built longitudinal maps to reveal warm and cold regions of the planet and include the effect of natural satellites.

Chapter 3

Types of input data

We have benefited of several types of data in order to obtain the thermal emission of a variety Earth-like planets. First, we have used high-resolution thermal emission data of the Earth (Section 3.1), the data are implemented with satellite observations and validated by ground measurements, thus the time series built by the model is an accurate reproduction of an ideally observed light curve of the Earth. Second, we have used global climate model (GCM) simulations (Section 3.2) and by the modification of some specific parameters, we have build the thermal emission of nine Earth-like planets, including the Earth for validation (Section 3.2.1). Finally, we have simulated some of the planets of the previous set by a generic spectral version of the LMD GCM (Section 3.3). Adding the spectral information to the time series, allows us to determine the contribution to the emission, the state and the dynamics of important atmospheric species as carbon dioxide or water vapor. Some of these compounds are called biomarkers as their abundances may indicate the presence of life.

3.1 NASA-SRB Earth data

In Chapter 4, we simulate the thermal emission of the Earth using top-of-the-atmosphere (TOA) all-sky upward longwave (LW) flux maps integrated over the 5-50 μm wavelength interval. The data were obtained from the NASA Langley Research Center Atmospheric Sciences Data Center, they belong to the NASA/GEWEX SRB Project[1] (Suttles et al., 1989; Gupta et al., 1992), whose aim of this project is to determine surface and TOA atmospheric shortwave (SW) and longwave (LW) radiative fluxes with the precision needed to predict transient climate variations and

[1] http://www.gewex.org/

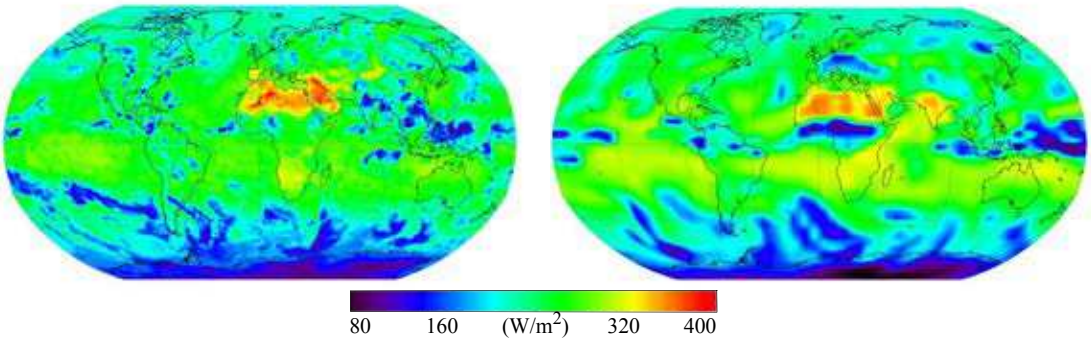

Figure 3.1 Maps of Earth's outgoing mid-infrared radiation. SRB data (left) and LMDZ Earth GCM data (right) at midsummer noon.

decadal-to-centennial climate trends for the Earth.

The GEWEX LW algorithm, uses real measurements to build the emission data (Fu et al., 1997), appliying a thermal infrared radiative transfer code with input parameters derived from the International Satellite Cloud Climatology Project[2] (ISCCP; Rossow et al. (1996), the Goddard EOS Data Assimilation System level-4[3] (GEOS-4), the Total Ozone Mapping Spectrometer[4] (TOMS) archive, and the TIROS Operational Vertical Sounder[5] (TOVS) data set.

An assessment of the quality of the global fluxes was accomplished by comparisons with corresponding ground measurements obtained from the Baseline Surface Radiation Network (BSRN), the Swiss Federal Institute of Technology's Global Energy Balance Archive (GEBA) and NOAA's Climate Montitoring and Diagnostics Laboratory (CMDL). LW flux uncertainties are within ± 5 W/m^2 (σ=1.5%). The data have a time resolution of 3 hr over the whole globe, and a spatial resolution of 1°x1° square cells in latitude and longitude. We used a set that covers a 22 year

[2]http://isccp.giss.nasa.gov/
[3]http://daac.gsfc.nasa.gov/
[4]http://jwocky.gsfc.nasa.gov/
[5]http://www.ozonelayer.noaa.gov/action/tovs.htm

period from 1983 to 2005. A typical map of the outgoing mid-infrared radiation of the Earth, directly represented from the GEWEX data, is shown in Figure 3.5 (left). The map represent the average flux over the period 18:00–21:00 UT for 1 July 2001. It is important to note that in mid-infrared maps, desert zones such as the Sahara-Arabian region appear as warm spots and cold or very humid regions such as clouds over the Antarctica or Indonesia appear as cold spots.

3.2 LMDZ GCM data

In chapters 5 and 6, we use Earth-like planet simulations build with the LMDZ GCM, a Global Climate Model developed by the Laboratoire de Météorologie Dynamique de Paris[6]. The model has 48 grid points regularly spaced in latitude and longitude, yielding a horizontal resolution of 3.75 by 7.5 degrees, and 19 atmospheric pressure levels on the vertical dimension. Sub-grid scale processes such as radiative transfer, clouds, convection, and small-scale turbulence are parameterized as described in Hourdin et al. (2006). The 2-dimensional fields used to compute the thermal emission are output every 3 hours, giving the same time resolution than SRB data. In water-world simulations, the surface is covered by a global ocean – a configuration known as an "aquaplanet" – modeled by a "slab" of a uniform depth of 50 m representing the oceanic surface mixed layer. The evolution of the slab temperature is determined by the surface energy fluxes, as well as heat transport by horizontal diffusion and parameterized wind-driven ocean currents (Codron, 2012). In addition, a simple thermodynamic sea-ice model is used wherever the surface temperature drops below freezing.

3.2.1 Model Validation

With the purpose of validate LMDZ GCM data reproduction of the thermal emission of an Earth-like planet, we have compared the results obtained for the

[6] `http://lmdz.lmd.jussieu.fr/?set_language=en`

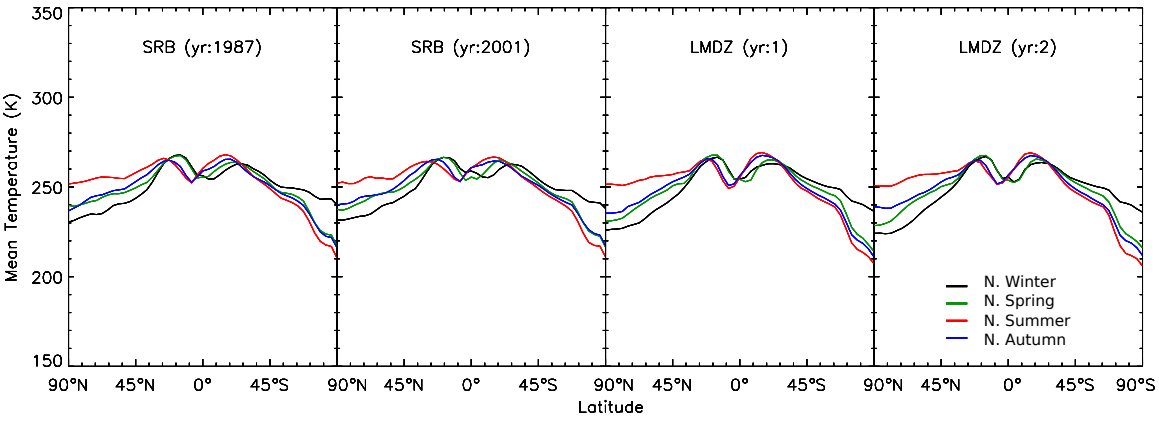

Figure 3.2 Mean Temperature vs latitude, for SRB data (years 1987 and 2001) and LMDZ data (2 years of the sample). Colours represent the position of the planet on the orbit, corresponding to seasons in the northern hemisphere: winter (black), spring (green), summer (red) and autumn (blue).

Earth for both SRB (Chapter 4) and LMDZ GCM (Chapter 5) models. Whereas NASA-GEWEX SRB model is implemented and validated by satellite and ground-based observations, LMDZ calculates the meteorological variables, the transport of numerous constituents (aerosols, chemical compounds of the atmosphere, radio-elements, stable water isotopes, etc...) and benefits from several models to obtain variables such as the vegetation cover, the cycles of water and carbon, the ocean circulation, the marine biochemistry or the dynamics of sea ice.

The main differences between the two models (Fig. 3.1) are the horizontal resolution, which is of 1 by 1 degrees in the case of the SRB model and of 3.75 by 7.5 degrees in the case of the LMDZ model, and the cloud covering. Unfortunately, the representation of clouds in climate models is still unsatisfying. Most cloud properties cannot be resolved by global-scale models and they have to be parameterized in terms of the model variables. Clouds cover the Earth's surface by about 70% and have a very strong effect on the radiation balance of the planet (Section 2.2). Parameterizations are complicated by the fact that clouds cover a large range of scales

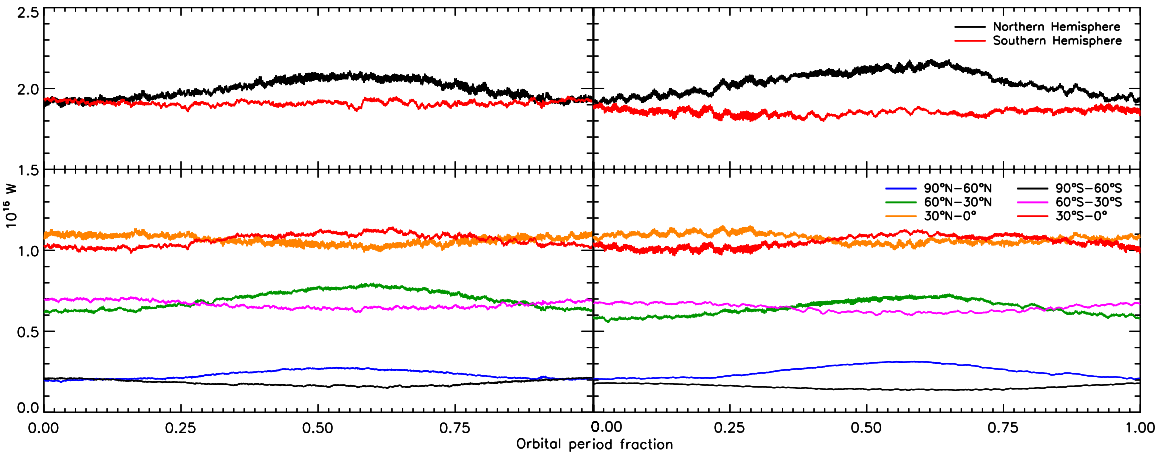

FIGURE 3.3 TOA-flux radiant power of the Earth during one orbit, starting January the 1st, for SRB data (left) and LMDZ data (right). Northern and Southern hemispheres (top) and latitude bands (bottom).

(from microphysics to meso-scale systems), and moreover liquid and ice phases have to be treated separately. Cloud water is predicted by a budget equation where both ice and liquid phases have to be considered jointly. The condensation scheme uses a "hat" probability density function for total water in a grid box, which allows to account for fractional cloudiness, and then the total condensed water is partitioned between liquid water and ice, depending on the local temperature. LMDZ GCM LW cloud radiative forcing has been validated by satellite observations. Doutriaux-Boucher & Quaas (2004) found a discrepancy up to the 40% for mid- and high-latitudes. However, equatorial latitudes, which account for most of the emission, fit to the observations and then global climate parameters are valid.

The mean surface temperature is 288 K in both SRB and LMDZ models, the Bond albedo have a value of 0.31 for SRB-model and of 0.30 for the LMDZ, the effective temperature of the planet is 254 K and 255 K respectively and the normalized greenhouse parameter is 0.39 in both models.

The annual mean brightness temperature per latitude at TOA in both models

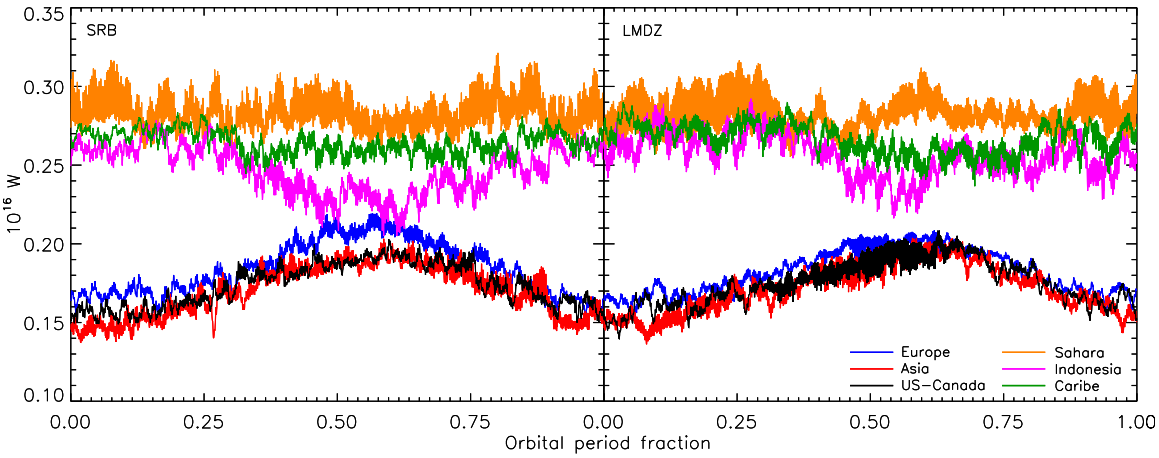

Figure 3.4 TOA-LW radiant power of continental regions of the Northern Hemisphere during one orbit, starting the 1st of January. In the 60°N-30°N latitude band: Europe (blue), Asia (red) and US-Canada (black). In the 30°N-0° latitude band: Sahara-Arabian (orange), Indonesian (magenta) and Caribbean-Mexico area (green). Regions at the same latitude band have equivalent areas.

is also very similar (Fig. 3.2). The profiles show the seasonal variation and the asymmetry between hemispheres: in the Northern Hemisphere, summer and winter are respectively warmer and colder than in the Southern Hemisphere. The prevalence of oceans in the mid-latitudes of the Southern Hemisphere, explains the mild seasonal variation, as water has a low thermal inertia and the temperature does not suffer a great change. Both seasonal and mean temperatures of the poles are similar with slightly colder temperatures in the LMDZ model. The convection clouds assembled at the Intertropical Convergence Zone (ITCZ) have a lower thermal emission at the top than clearer regions, producing the decrease in temperature at the equatorial zone. The seasonal shift of the ITCZ is similar in both models but the central temperature is also colder in the LMDZ. The interannual standard deviation from the mean is around 0.5% in the SRB model, 0.4% in the LMDZ, with 0.7% of variation between the two models.

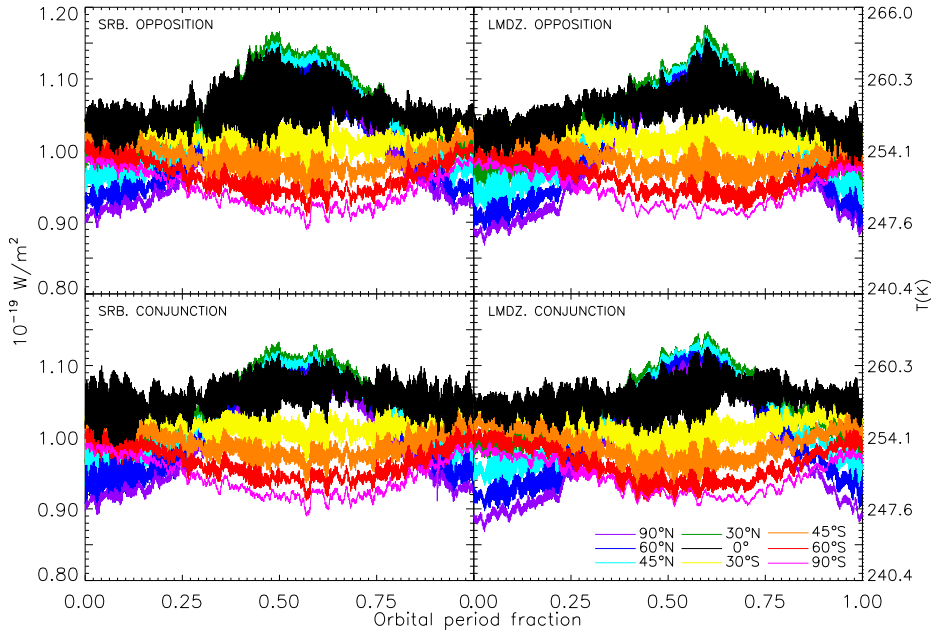

FIGURE 3.5 TOA-all-sky flux towards an observer at opposition (top row) and at conjunction (bottom row) during one rotation for the Earth, SRB data (left) and LMDZ (right) scaled in flux and brightness temperature.Colours indicate the latitude of the sub-observer point.

Once the global parameters are validated, we proceed to check the behavior of the non-averaged emission. We compare the TOA radiant power at different latitudes, with special attention to extreme climate regions, the observed thermal emission for several geometric configurations, the autocorrelation of the series, and the averaged longitudinal curves produced by both models. Figure 3.3 shows the mid-infrared radiant power of the Earth along one orbital period for SRB and LMDZ data respectively. The radiant power is very sensible to the the variability of the emission and contribution of each region to the global mean. We have divided each hemisphere in three latitude-bands: 90°N-60°N (blue), 60°N-30°N (green), 30°N-0° (orange), 90°S-60°S (black), 60°S-30°S (magenta), 30°S-0° (red), and we have computed separately the emission of each hemisphere as long as the emission from the bands.

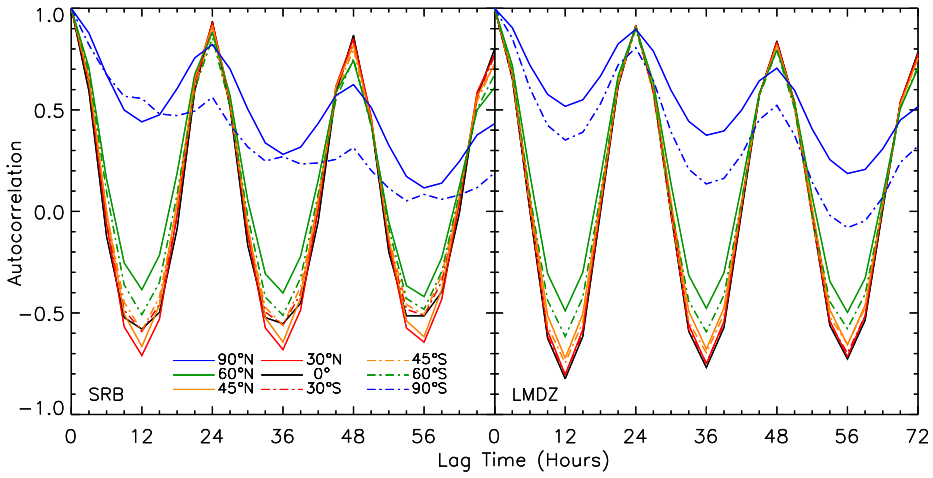

Figure 3.6 Earth autocorrelation at opposition during northern winter for SRB data (left) and LMDZ (right). Colours indicate the latitude of the sub-observer point.

Although the global values are in general in agreement with SRB data, temperatures are slightly colder in the LMDZ, except for the band from 90°N-60°N during summer. As we explain in Chapter 4, tit is interesting to note that the thermal emission of the Earth has a particular characteristic: the Northern Hemisphere emits more radiation than the Southern one (top charts). Comparing both models, the excess during Northern Summer in the LMDZ comes from a warmer Northern Pole during this season. The colder temperatures of the Southern Hemisphere come from a combination of several factors: a higher CRF (specially during the Southern Summer, it appears as a short-frequency variability at equatorial latitudes, Fig. 3.3, red lines) and the colder LMDZ temperatures at the winter poles as the Antarctica (Fig. 3.3, black bottom lines).

Figure 3.4 illustrates the emitted flux along one orbit by certain areas of the planet: Europe, Asia, US-Canada, Sahara-Arabia, Indonesian, and Caribbean-Mexico regions. The short frequency corresponds to the mean temperature variation in the region along the day. This diurnal variability of the signal is modified by the existence

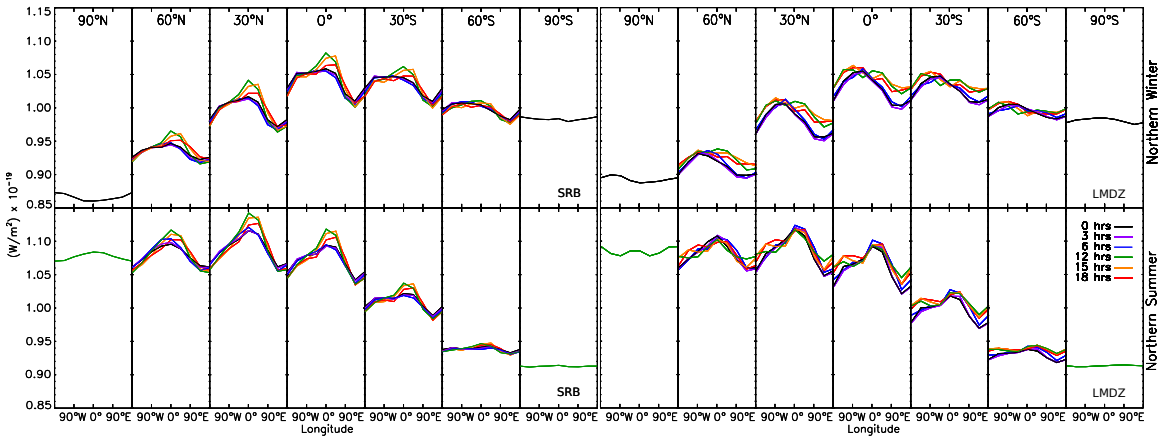

FIGURE 3.7 TOA-all-sky flux Earth rotational curves at opposition during northern winter (top) and northern summer (bottom) for SRB data (left) and LMDZ (right) scaled in flux and brightness temperature. Colours indicate the latitude of the sub-observer point.

of high clouds, the emission coming from the surface is absorbed by the cloud, and then the emission from the cloud top is radiation that actually contributes to the signal. As previously mentioned, in general, temperatures are well reproduced by the LMDZ model but the longwave CRF deviate from the observations. The signal is also less uniform in this case, as the emission shows high values all along Northern Winter with very few perturbations, meaning that the Sahara region is less cloudy during this season. During Northern Summer, a stable cloudy ITCZ appears over the african forest-savanna in LMDZ data (Fig. 3.1, left), as a consequence, the value of the emission from the area considered (0°-30° in latitude) is lower.

Figures 3.5, 3.6, and 3.7 illustrate respectively the TOA thermal emission flux time series, the autocorrelation and the average longitudinal light curves of the Earth in both models. The brightness temperatures, the seasonal cycle and the rotational variability of the time series are well reproduced. The regularity of LMDZ autocorrelation during northern winter is explained by the fact that LMDZ is less cloudy during this season. The deviations in the rotational light curves between the two models are explained by the differences in the cloud treatment and in the

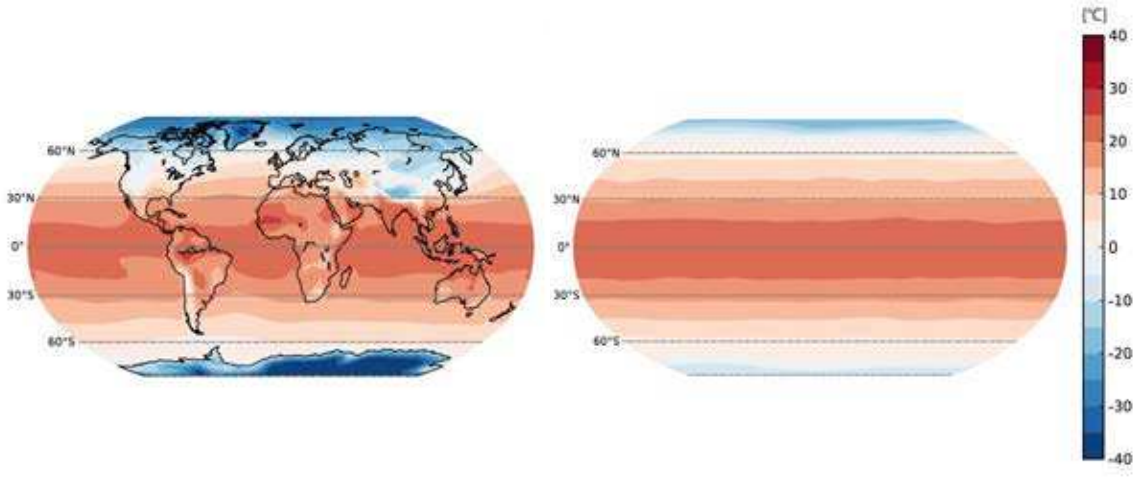

Figure 3.8 LMDZ-generic-GCM surface temperature for the Earth (left) and the aquaplanet O–1 (right) (courtesy of Benjamin Charney, Laboratoire de Météorologie Dynamique, Université P&M Curie (UPMC)).

horizontal resolution. However, the main results are consistent and the deviations that are not critical for this study.

3.2.2 Earth-like planet set

Once we have proven the validity of LMD GCM to reproduce the signal of a terrestrial planet, we obtain the simulations varying one or few parameters at a time, to study the effect on the signal. We have organized our work in two parts:

i) Planets in a terrestrial orbit.– In Chapter 5, we have reproduced the Earth (Ete–1) at first, and then we have built three different planets, keeping the atmospheric composition and the orbital parameters of the Earth and varying the rotation rate and the albedo, in order to study the influence of these two parameters on the climate and the emission. The three planets are: an Earth-like planet with a rotation period of 10 days (Ete–10), an aquaplanet (Ote–1) and a snowball aquaplanet

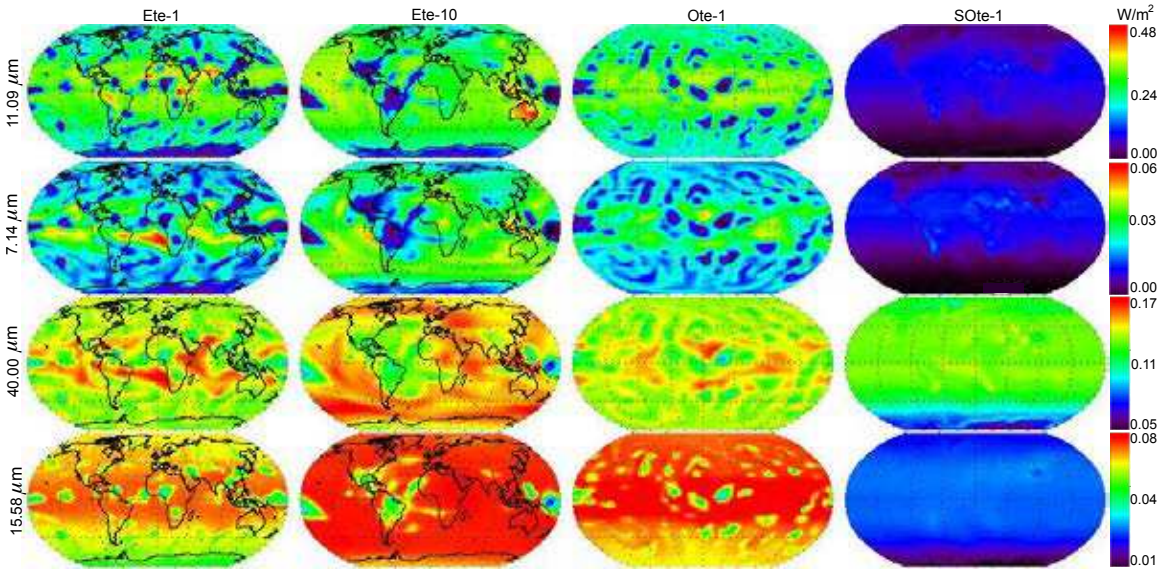

FIGURE 3.9 TOA-flux emission for the bands (from top to bottom): 11.02 μm, 7.14 μm, 40.00 μm, 15.58 μm for the planets (from left to right) Ete–1, Ete–10, Ote–1, SOte–1. The respective wavelength intervals are: (10.63, 11.43) μm, (6.90, 7.41) μm, (35.71, 45.45) μm, and (14.99, 16.21) μm.

(SOte–1) on which the solar constant is diminished to 80% in order to achieve the snowball state.

ii) Water worlds.– In Chapter 6, we study the thermal emission of Earth–like planets covered by a global ocean (aquaplanets). The homogeneous surface of an aquaplanet and the high thermal inertia of water make the rotation rate hard to detect. We have studied five different configurations for a water world. All the planets of the study have the same solar constant as the Earth – with different distance to the star for the synchronous ones– and zero eccentricity and obliquity, to suppress the influence of a seasonal cycle. We have two aquaplanets, named as O–1 and O–10. The first one has a rotation rate of 1 day, and the latter has a rotation rate of 10 days. Then we have build three synchronous aquaplanets, Os–1, Os–10 and Os–360, with rotation rates of 1, 10 and 360 days, respectively. We have compared our results

with those obtained for the Earth and the aquaplanet Ote–1.

3.3 LMD generic GCM spectral data

We have used a new generic version of the LMD Global Climate Model to simulate the spectral light curves of the set of Earth-like planets in a terrestrial orbit (Chapter 5): the Earth, the Earth with a rotation rate of 10 days (Ete–10), the aquaplanet Ote–1 and the snowball aquaplanet SOte–1. This model is derived from the LMDZ Earth GCM (Hourdin et al., 2006), it has been used to study early climates in the solar system (Forget et al., 2012; Wordsworth et al., 2012) and climates on extrasolar planets (Wordsworth et al., 2011; Leconte et al., 2013).

The simulations have a horizontal resolution of 3.75 degrees latitude by 5.625 degrees longitude, a time resolution of 3 hrs and, for comparison with the results obtained from the LMDZ Earth GCM, we have 38 narrowbands with 25 in the broadband of (5-50) μm. In the vertical, the model uses hybrid coordinates, which consist of a terrain-following coordinate system in the lower atmosphere, and pressure levels in the upper atmosphere.

The evolution of the surface temperature is governed by the balance between radiative and sensible heat fluxes, which takes in account the direct solar insolation, the thermal radiation from the atmosphere and the surface, and turbulent and latent heat fluxes, and the thermal conduction in the soil. The parameterization of this last process is based on an 18-layer soil model solving the heat diffusion equation using infinite differences. The depth of the layers were chosen to capture diurnal thermal waves as well as the deeper annual thermal wave. A vertically homogeneous soil is assumed, while the thermal inertia of the ground is set to 2000 $Js^{-1/2}m^{-2}K^{-1}$ everywhere. In equilibrium, the globally averaged difference between outgoing longwave radiation (OLR) and the absorbed solar radiation (ASR) was found to be lower than 2 W/m^2. Simulations for temperate climates are typically

run for 40 years, however as cold climates attain the equilibrium after a longer time, in this model the simulations are run over 80 years to be sure not to miss a full glaciation.

3.4 Summary

To obtain the planetary integrated mid-infrared emission in the direction of a remote observer randomly located, three types of data have been implemented by our model. First we have used satellite validated data from NASA-SRB project in order to obtain an accurate reproduction of the thermal light curve of the Earth (Chapter 4). Secondly, we have used the Earth climate model LMDZ to reproduce the Earth and the results obtained are validated by the comparison with SRB data. Then, we have modeled nine Earth-like planets including: a slow Earth, an aquaplanet and a snowball planet with the orbital parameters of the Earth (Chapter 5), two aquaplanets with circular orbits and three synchronous aquaplanets (Chapter 6). Finally, we present the research possibilities of the multiband LMDZ GCM (Chapter 7).

PART III.

PHOTOMETRIC VARIABILITY OF THE EARTH

Chapter 4

NASA SRB data

We present the analysis of the global-integrated mid-infrared emission flux of the Earth based on data derived from satellite measurements. We have studied the photometric annual, seasonal, and rotational variability of the thermal emission of the Earth to determine which properties can be inferred from the point-like signal. We are interested in the relevant conditions to retrieve the physical characteristics of the planet from the thermal light curve: geography, weather, eccentricity, axis tilt, phase angle, etc. Section 4.1 is an introduction to Earth seen as an exoplanet, the analysis of the time series, rotation rate and longitudinal light curves is presented in Section 4.2. Section 4.5 discuses the contribution of a satellite to the planetary signal and particularly the case of the Earth-Moon system and the conclusions are given in Section 4.6.

4.1 Introduction

Although the aim of numerous studies in transit spectroscopy is the characterization of terrestrial planets around M stars, in this thesis, we are focused in the characterization of an Earth analog around a G star. This case is more challenging for several reasons: G stars are less numerous than M stars, the transit probability in the habitable zone is 10 times lower than it is for M stars, the orbital period (and thus the duration between two transits) is significantly longer for G stars, and the planet-to-star contrast ratio is less favorable for secondary eclipse spectroscopy. For this matter, direct detection seems to be necessary to study Earth analogs around G stars and several instrument concepts have been proposed (Traub et al., 2006; Danchi & Lopez, 2007; Trauger & Traub, 2007; Cash et al., 2009); depending on the concept, it is either the light scattered in the visible or the infrared emission that can be detected. Then, both spectroscopy and photometry can then be used to derive

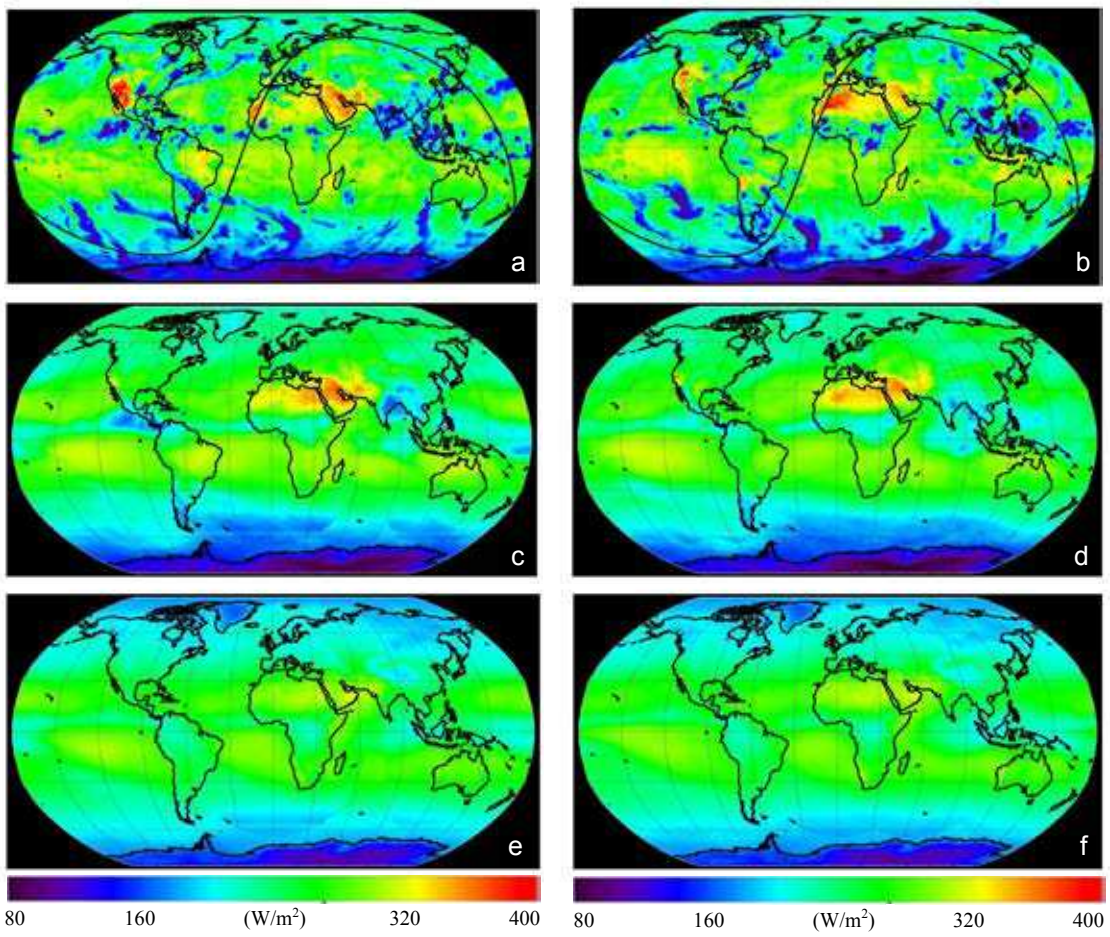

FIGURE 4.1 Maps of Earth's outgoing mid-infrared radiation. Average over the period 18:00–21:00 UT of 1987 July 1 (a) and 2001 July 1 (b) together with the subsolar point and the terminator at the mean time. At that time the brighter regions of the Earth correspond to the deserts of Sahara, Arabian Peninsula, Atacama, and Arizona. Average over the months 1987 July (c) and 2001 July (d). Average over the years 1987 (e) and 2001 (f).

some planetary properties. An important step toward these ambitious programs is to determine what level of characterization could be achieved when observing the Earth as a distant *pale infrared dot*. For instance, in the optical range, broadband photometry can potentially give us information about the albedo and the cloud cover.

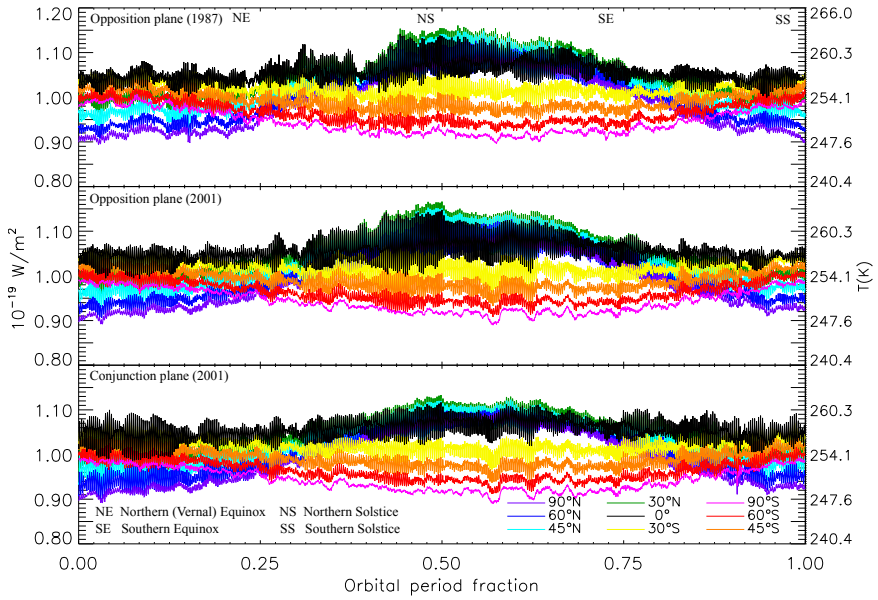

FIGURE 4.2 Time series of the mid-infrared emission flux for the two years of 1987 (top) and 2001 (middle and bottom). The sub-observer's point is represented by the latitudes 90°N, 60°N, 45°N, 30°N, 0°, 30°S, 45°S, 60°S, 90°S, and 0° longitude at the initial time (January 1, 0:00 UT) and the direction planes of opposition (O) (top and middle) and conjunction (C) (bottom).

The uneven distribution of oceans and continents enables the measurement of the 24 hr rotation period by the autocorrelation of the signal for several viewing inclination angles despite the presence of active weather (Pallé et al., 2004, 2008). Visible and near-infrared spectroscopical studies have been made by, e.g., Hearty et al. (2009), Cowan et al. (2011), Robinson et al. (2011), and Livengood et al. (2011) observing rotational and seasonal variations of the Earth spectrum and their influence on the detectability of the spectral signatures of habitability and life.

In this chapter, we provide an integrated mid-infrared (5–50 μm) photometric time series model of the Earth, with 3 hr time resolution, over a period of 22 years of available satellite data. From this geographically resolved data set, we derived the disk-integrated photometric signal of the Earth seen as a point-source planet. The NASA-SRB thermal emission maps of the Earth clearly show warm areas over the

Table 4.1. Photometric Variability of the Integrated Earth Mid-infrared Flux (Percentage Over the Mean Value)

Viewing Angle	Orbital Amplitude		Rotational Amplitude			
	1987	2001	Jan	Apr	Jul	Oct
90°N (N. Pole)	20	19	1	1	2	1
45°N (Mid-lat)	14	14	4(6)	4(4)	8(5)	5(5)
0° (Equator)	6	5	5(8)	5(4)	8(5)	4(5)
45°S (Mid-lat)	7	7	3(5)	3(2)	3(2)	2(3)
90°S (S. Pole)	11	10	1	1	1	1

Note. — Mean amplitude values of the orbital (seasonal) variability for the years of 1987 and 2001 and of the rotational variability over the months of 2001 January, April, July and October for (O) and (C) (in parenthesis) observers situated at different latitudes. Each value is calculated as the percentage of the average variation over the mean value. Data analysis for different years/months retrieves similar results.

deserts and cold spots over cold or humid regions of the planet (Fig. 4.1 a-b). These features are still relevant over monthly (Fig. 4.1 c-d) and annual averaged maps (Fig. 4.1 e-f). As we will see in this chapter, along with the uneven distribution of land and oceans over the planet, with a predominance of land masses in the Northern Hemisphere (NH), are the major factors that modulate the particular thermal emission of the Earth.

4.2 Time series analysis

Two examples of the annual time series of Earth's outgoing mid-infrared radiation are plotted in Figure 4.2. The high frequency variability corresponds to the emitted mid-infrared flux due to Earth's rotation superimposed to the seasonal variation during the year. It is readily observable from the figure that the amplitude of the rotational variability is larger for an observer in the equatorial plane (black) and decreases toward more poleward views (violet, magenta). On the contrary, because the obliquity of the Earth is about 23.44° and then the variation of the annual insolation is larger at higher latitudes, the amplitude of the seasonal variability increases for the polar geometries and decreases towards an equatorial view.

As it is expected, the seasonal variation of the northern latitude time series is opposite to the southern one due to the seasonal cycle of solar insolation. For observers over the Northern Hemisphere, the time series reach a maximum during the boreal summer near the beginning of August (orbital period fraction)(opf)~ 0.6). The equatorial view follows the same pattern, showing a "northern-biased" behavior of the planet. As we have explained in the previous section, this is due to the existence of large landmasses in the Northern Hemisphere that emit more infrared radiation than the oceans and make the northern summer hotter. In the time series, this effect is accentuated by the planetary view.

Table 4.1 shows the amplitude values of the seasonal variability of the globally integrated mid-infrared flux for the years of 1987 and 2001 and for five viewing geometries: 0° (Equator), 45°N, 45°S, 90°N (North Pole) and 90°S (South Pole). The amplitude is given in percentage change over the annual mean value. In order to conduct a seasonal study of the mid-infrared Earth emission, four representative months (January, April, July and October) were selected per year. For the sake of simplicity, we present in particular the results of the year 2001, however the rest of the data set give similar results. For comparison, we give the values taken by the observers placed in the opposition and in the conjunction planes (in parenthesis), because they have the same view of the planet at different local hours. We can see that the orbital amplitude variation of a northern latitude is twice the value of the

southern equivalent latitude. The seasonal variability dominates the signal in most latitudes except for the equator, where seasonal and rotational variability are similar. It is notable that whereas the mean temperature varies with the season, the rotational variability depends strongly on the local hour (Section 2.2). This effect can be seen in the black graphs of the two bottom charts of Figure 4.2, each graph correspond to two observers at the equator plane at opposite sides of the planet. The observer placed at opposition the 1st of January (opf=0) sees the planet at midnight, whereas the observer placed at conjunction sees the planet at midday. In summer (opf$\sim$ 0.5), the planetary view is the opposite, the observer at opposition sees the planet at midday and the observer at conjunction sees the planet at midnight. Mid-latitude and equatorial viewing geometries show a pronounced and synchronized rotational variability (up to 8% in change), whereas the polar light curves present almost no variations.

4.3 Periodicities

The duration of the statistically significant peaks in the autocorrelated time series can give us an estimation of the lifetime of the cloud structures, typically of around one week for Earth clouds (Pallé et al., 2008). In the outgoing mid-infrared radiation flux, a 24 hr rotation period is clearly shown, a value close to the true rotation period. This rotational signature has two origins. First, some large regions exhibit systematically high or low brightness temperatures. This is the case for Indonesian and Sahara areas, as the former is one of the most humid and cloudy regions on the planet, whereas the latter is warmer and drier than Earth's average. Therefore, the two regions appear as fixed cold and hot features respectively, even on averaged outgoing flux maps, as we can see in Figure 4.1(c) and (d) where the TOA emission is averaged over a month and in Figure 4.1(e) and (f) where it is averaged over a year.
A smaller effect comes from the diurnal cycle (the change of brightness temperature between day and night in a region), which is negligible in most locations, because of humidity, clouds, or ocean thermal inertia, but noticeable in some dry continental areas as we discuss in the next section. In fact, it is the diurnal cycle of the dry

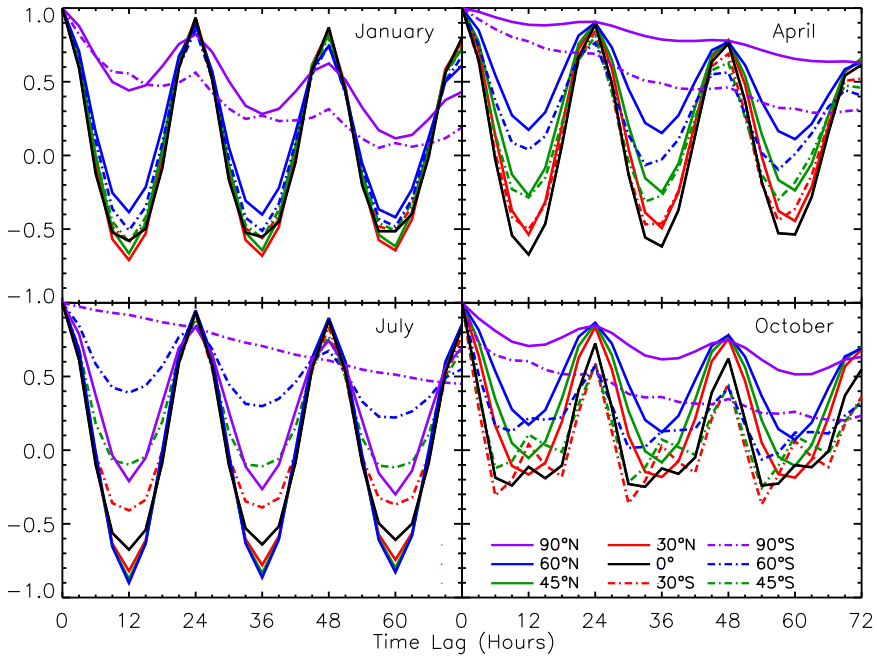

FIGURE 4.3 Autocorrelation functions of the mid-infrared emission flux from Earth. 2001 January, April, July, and October for the latitudes 90°N, 60°N, 45°N, 30°N, 0°, 30°S, 45°S, 60°S and 90°S.

lands, which makes possible the detection of the rotation period for the case of the North-polar view during the more stable seasons (winter and summer), as it is shown in Section 2.2. Although it is always the same fraction of the planet (the whole northern hemisphere) in the field of view, the change in temperature along the day in the dry continental areas causes the rotational modulation, as it is shown in Figure 4.3 (violet solid line). However, an observer looking at the South Pole does not detect a significant rotational variability, Figure 4.3 (violet dash-dotted line), not even for the austral summer when the effect of clouds would be minimized. In the Southern Hemisphere, the distribution of land is largely dominated by oceans whose high thermal inertia make diurnal temperature variability negligible.

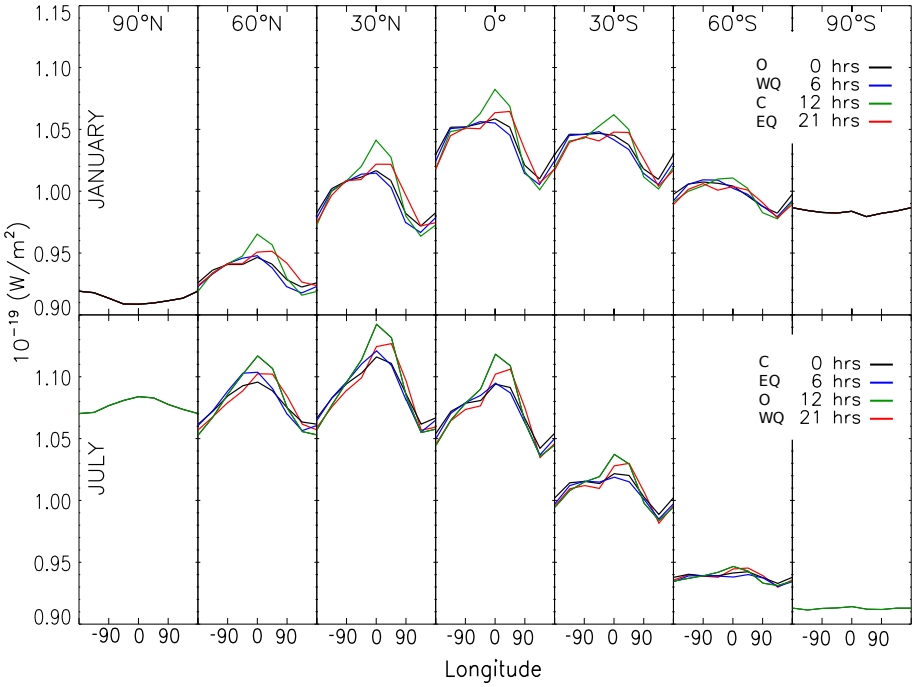

FIGURE 4.4 Rotational light curves of the mid-infrared radiation emitted from the Earth. 2001 January (top row) and July (bottom row) for the latitudes 90°N, 60°N, 30°N, 0°, 30°S, 60°S, and 90°S latitudes, the colors correspond to local hours, 0 hr (black), 6 hr (blue), 12 hr (green) and 18 hr (red) and the direction planes of opposition (O), conjunction (C), western quadrature (WQ) and eastern quadrature (EQ).

4.4 Average Rotation Light Curves

Once the rotation period is identified, the observer can produce a typical rotation light curve by folding the time series obtained during weeks or months over the rotation period. This process averages out random cloud variability. It is clearly seen on the maps of Figures 4.1(c)–(f), where the clouds disappear for longer average times whereas the strongest features mentioned on the previous section prevail. Then the observer can plot this average rotation light curve as a function of an arbitrary longitude (in our case the longitude that we have chosen is the conventional geographic longitude for commodity). The shape of the light curve can then reveal

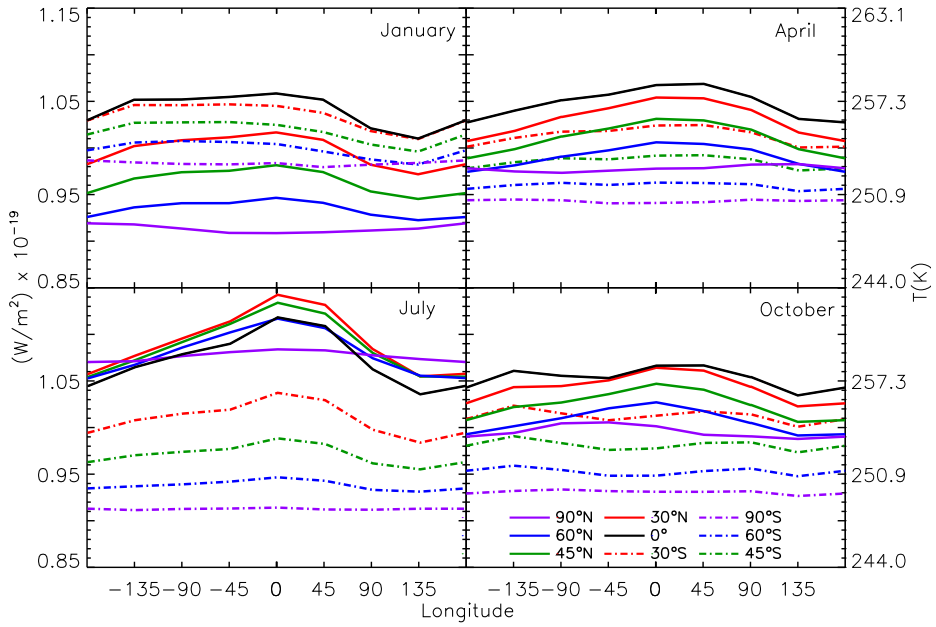

Figure 4.5 Rotation light curves of the mid-infrared radiation emitted from the Earth. For the months of 2001 January, April, July and October, 0° longitude and latitudes: 90°N, 60°N, 45°N, 30°N, 0°, 30°S, 45°S, 60°S, and 90°S.

brighter/fainter areas distributed in longitude. For instance, observers over a latitude of 30°N would note that the brightest and faintest point of the light curve occur when the longitude 0° (Sahara) or 135° (Indonesia) are respectively centered on his view. The results are represented in Figure 4.4 and Figure 4.5.

Figure 4.4 represents the rotational variability respect to the local hour for several latitudes (in column) at the months of January (top row) and July (bottom row). Each graph corresponds to four observers initially placed at the four astronomical longitudes (meridional planes) O, C, WQ, EQ, previously defined, at the same latitude (at the top of each chart). Each of these four meridional planes correspond to a certain local hour that changes with the orbital movement of the planet. With this information, we can compare the temperature evolution for a given planetary region along the day (diurnal variability). The figure shows that the longitudes that reach the maximum of temperature, have also the largest variation along the day; whereas the

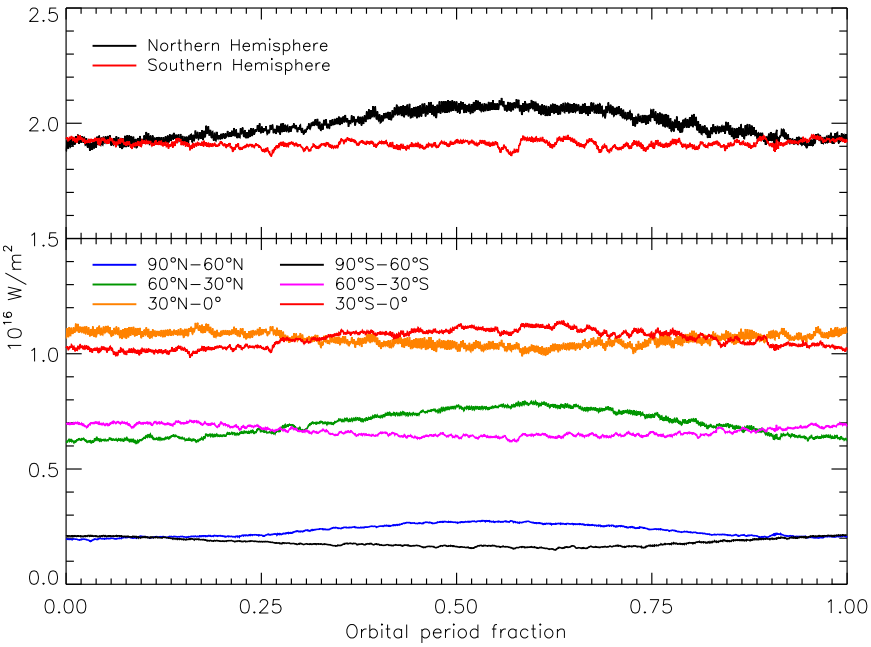

FIGURE 4.6 TOA–LW infrared emission flux of the Northern and Southern hemispheres. Total emission (top) of the Northern Hemisphere (black) and Southern Hemisphere (red). Latitude bands (bottom) of 90°N–60°N (blue), 60°N–30°N (green), 30°N–0° (orange), 90°S–60°S (black), 60°S–30°S (magenta) and 30°S–0° (red).

longitudes where the minimum is attained, show a little variation. For the cases where the observers are placed over the poles, the planetary view does not change with time so the local hour of the graph is taken just as reference of the observation time (Section 2.1). For the North Polar view, not only during summer but also during winter, the minima occurs when it is 0 UT (0 hr at 0° longitude or 12 hr at 180° longitude) and the maxima when it is 12 UT (0 hr at 180° longitude or 12 hr at 0° longitude), which illustrates the diurnal cycle effect previously mentioned. These hours coincide respectively to midnight and midday in the Sahara desert. The greatest influence of this region is noticed at the chart of 30°N latitude when the Sahara-Arabian region (15°W-50°E) is in the center of the planetary disk. The rotational amplitude is also influenced by the seasonal cycle, as we can see in the flux difference between January and July. Either in summer or winter the diurnal variability reaches the 2% at low

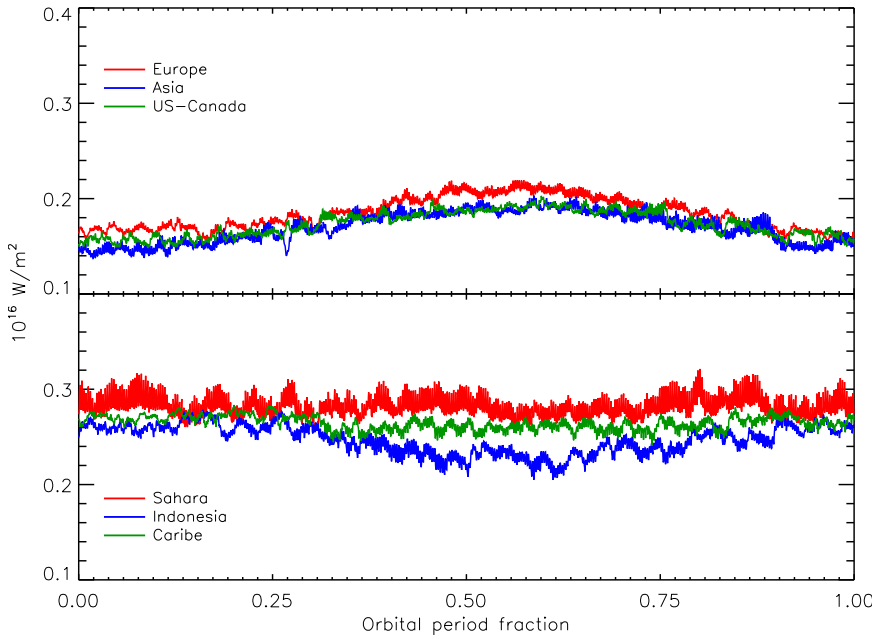

Figure 4.7 TOA–LW infrared emission flux of some continental regions in the Northern Hemisphere. In the 60°N–30°N latitude band (top): Europe (red), Asia (blue), and US-Canada (green). In the 30°N–0° latitude band (bottom), Sahara-Arabian (red), Indonesian (blue), and Caribbean-Mexico area (green).

latitudes, although the main contribution to the flux is due to the solar insolation along the year (seasonal cycle) and to the rotation variability. For Polar views, the amplitude is only due to the diurnal variability.

Figure 4.5 represents the rotational variability for observers placed at 0° longitude and different latitudes. It is important to note the temperature evolution with time for each geometry, implying a seasonal behavior. The equator shows a warm stable temperature during the year, whereas the summers of each hemisphere differ being the northern summer hotter, as it is shown in Figure 4.4. The maximum and minimum regions do not change with the seasons, except for April and October when the presence of the clouds can mask the signal.

In order to check the possible source of the diurnal variation on the Northern Hemisphere, we have made a further analysis of the emitted flux by geographic

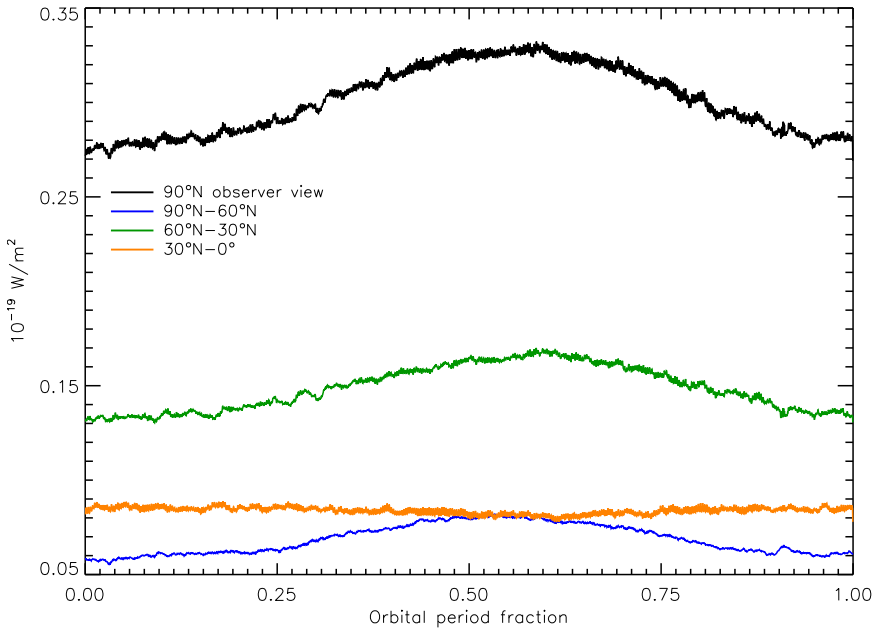

FIGURE 4.8 Time series for a North Polar observer (black) and the contribution of each latitude band to the signal. 90°N–60°N latitude band (blue), 60°N–30°N (green) and 30°N–0° (orange).

latitude bands. Figure 4.6 shows the mid-infrared emission of the Earth along one orbital period. Each hemisphere is divided in three latitude bands of flux: 90°N–60°N (blue), 60°N–30°N (green), 30°N–0° (orange), 90°S–60°S (black), 60°S–30°S (magenta), 30°S–0° (red). We can see that the Northern Hemisphere exhibits a larger seasonal variation than the Southern Hemisphere and this variation is more important for mid-latitudes. As it was previously mentioned, the greater diurnal variability comes from the latitudinal band 30°N–0°, also in this band, there is a decrease in flux during summer. This is due to the migration of the Intertropical Convergence Zone to these latitudes, which produces large bands of humidity and clouds with low brightness temperatures. As expected, we can observe that the Southern Hemisphere is in general colder than the North Hemisphere, and this difference is particularly remarkable between the South and the North poles.

For the identification of the region that produces the largest variability, we have

analyzed the emission of six regions of the planet (Figure 4.7). The chosen regions have an area of 30°×60° latitude–longitude, then fluxes from the same latitude band can be compared. For the 60°N–30°N band we have chosen three regions centered in Europe (red), Asia (blue) and US-Canada (green). For the 30°N–0° band the regions are centered in the Sahara-Arabian deserts (red), Indonesia (blue), and the Caribbean-Mexico area (green). As expected, the regions in the same latitude band have similar seasonal variabilities but the Sahara region emits more infrared flux and has greater diurnal variability.

However, the emission received by the observer changes with the view of the planet. In the most favorable case, an observer placed over the North Pole, the Sahara desert lies near the limb of the planetary disk and its influence on the signal is lessened by the perspective. In Figure 4.8, we can see the contribution of high- (blue), mid- (orange), and low- (green) latitudes to the signal received by an observer placed over the North Pole (black), a case in which the rotational variability is only produced by the diurnal cycle, as the planet presents the same face along its rotation. Then, the contribution to the diurnal variability of the signal is mainly due to low and mid-latitudes. Comparing Fig. 4.4, Fig. 4.5, and Fig. 4.6 with the signal received (Figure 4.2), we conclude that although there is a small difference between day and night produced by the warm areas, the signal is dominated by the seasonal behavior.

4.4.1 Phase Variation

While Earth's visible flux received by a remote observer is modulated by the changing phase of the planet, the Earth does not present significant phases when the integrated infrared flux is observed: the emission from the nightside contributes nearly as much as the emission from the dayside (Selsis, 2004).

As we have previously explained, the diurnal variability (1%-2%) is in general lower than the rotational (1%-8%) and the seasonal variability (5%-20%). This is shown in Figure 4.2 (middle and bottom), which represent opposite observers and then opposite visible phases of the planet. An observer at opposition (O) sees the winter midnight, the observer at conjunction (C) sees the winter noon which shows a

similar average temperature but a larger rotational variation. Figure 4.4 shows this difference between observers at O, C, WQ and EQ. The effect is amplified for warm areas at low latitudes, as the Sahara desert, as they have the larger contribution to the signal and it becomes more important for observers also at low latitudes, as the area pass by the center of the planetary disk. The equatorial observers of Fig. 4.2 (black) are represented by the graphs at 0 hr and 12 hrs at the central chart (0°), although we can see the difference of phase angle in the signal, the rotational and seasonal contributions dominate. Continental surfaces and the boundary layer above them (roughly the first 1500 m of the atmosphere) experience a drop of temperature between the day and night. This diurnal cycle is insignificant above the ocean (due to the high thermal inertia of water), hence over $\sim 70\%$ of the Earth surface. Day–night brightness temperature variations affect the outgoing thermal emission only in the 8–12 μm atmospheric window and above dry continents. This happens either over very cold regions which in this case do not contribute much to the global emission, or over deserts which represent a small fraction of the Earth surface. In addition, the diurnal cycle is much less pronounced above the boundary layer, at altitudes where most of the thermal emission is emitted to space. This is the reason why phase-correlated variations of Earth brightness temperature are negligible compared with seasonal changes. Even for the observing latitudes in the 30°N–0° range, in which the Sahara diurnal cycle appears in the modulation, the winter midday is colder than the summer midnight as it is seen in Figure 4.4.

4.5 Earth–Moon System Light Curves

We have modeled the mid-infrared flux of the Moon, with the purpose of study the combined light of a planet with a natural satellite. In the case of bodies with a negligible atmosphere, as it is the case of the Moon, the phase angle is relevant to compute the thermal emission. Due to a very low surface thermal inertia, the temperature map of the starlit hemisphere of the Moon can be calculated by assuming local radiative equilibrium at the surface (Lawson et al., 2007). When calculating the disk-integrated emission, the contribution of the dark side can be safely neglected

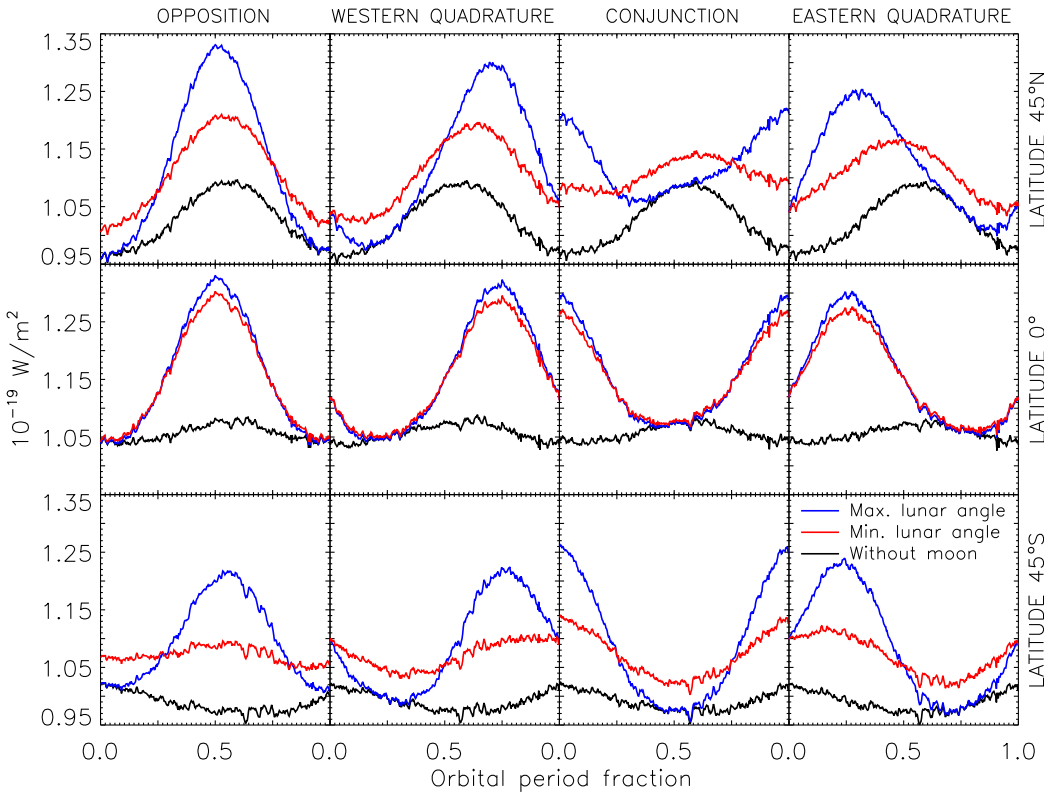

Figure 4.9 Earth–Moon mid-infrared emission light curves for one planetary orbit. 45°N (top row), Equator (second row), 45°S latitudes (bottom row), in columns the signals received by the observer's placed in opposition, western quadrature, conjunction, and eastern quadrature at the initial time. The colors correspond to the Earth (black) and Earth–Moon system, with lowest (red) and highest (blue) inclination angles of the Moon's orbit according to the observer's geometry (the possible orbits are comprehended between the two).

due to the high temperature difference. Thus, the flux received depends only on the phase of the Moon as seen by the distant observer. The amplitude of the lunar phase variations depends on the elevation of the observer above the lunar orbit, when we compute the Earth signal as a function of the latitude of the sub-observer point. As the the orbit of the Moon is not coplanar with the orbit of the Earth, a given observer latitude corresponds to a range of possible elevations above the

lunar orbit. In Figure 4.9, instead of calculating this elevation consistently with the chosen observer geometry, we bracket the orbital light curve of the unresolved Earth–Moon system with the two curves obtained by adding the lunar signal for the two extreme possible elevations. As pointed by Selsis (2004) and Moskovitz et al. (2009), it presents phase variations dominated by the Moon. We note that the modulation from the satellite becomes negligible for a Moon-like satellite with 20% of the Moon radius, a $\sim 5\%$ of the radius of the planet.

The two main annual variations that modulate the IR emission from the point-like Earth–Moon system are due to the seasons of the Earth and the phases of the Moon. These modulations present a phase shift that depends on the observer geometry. For some geometries, these two modulations are coincidental. This happens if the maximum of the lunar phase corresponds to Earth's annual emission maximum, which is for instance the case for an observer looking at northern latitudes that sees the Sahara at noon in July (see Figure 4.9, the first two panels of the left column). This particular observer will see only phase-correlated variations and may attribute this variability to a day–night temperature difference and conclude that the planet has less ocean coverage and a thinner atmosphere. With such particular geometry, seasonal variations could also be mistakenly attributed to the phases in the absence of a moon, unless the lunar origin of the modulation is identified using spectroscopy (Robinson, 2011).

4.6 Summary

In this chapter, we have constructed a 3 hr resolution model of the integrated mid-infrared emission of the Earth over 20 years in the direction of a remote observer randomly located.

The seasonal modulation dominates the variation of the signal. As expected, it is larger for the polar views because the planetary obliquity causes a bigger annual insolation change for these latitudes. For equatorial views, the seasonal maximum occurs during the summer of the Northern Hemisphere, as the latter contains large continental masses whereas the Southern Hemisphere is dominated by the oceans.

The rotational variability is detectable because of the uneven distribution of oceans and continents with geographical longitude. The daily maximum of the mid-infrared flux is shown when dry large masses of land, such as the Sahara desert, are in the observer's field of view. The daily minimum appears when cloudy humid regions such as the Indonesian area is visible, as iced big zone are confined to the poles. In the polar views, the distribution of land does not change with time but the diurnal temperature variation of large continental areas affects the signal, allowing the detection of the rotational period in the North Polar case. We find that the rotational variations have an amplitude of several percent, which is comparable to that of the seasonal variations for some latitudes. It is important to remark the strong influence of the weather patterns, humidity and clouds are sometimes able to mask the 24 hr rotation period of the signal for several days at a time. However, this effect can be solved by time folding.

It is important to point out that the Earth does not exhibit a significant modulation associated with phase variation (phase curve). This is because the integrated thermal emission does not generally probe the boundary layer (first km of the atmosphere) where the diurnal cycle takes place. If unresolved, the Earth–Moon system would however present a phase variation of Lunar origin. A satellite of the size of the Moon would introduce a strong phase variability that would completely dominate over the planet's signal. This effect adds high complexity to its interpretation by photometry.

At the light of these results it seems that future infrared photometric observations of terrestrial planets can be useful in order to characterize their atmospheric and surface features. If the planet is not completely covered by clouds, as Venus is, the presence of strong surface inhomogeneities (continents) can be extracted from the daily variations. The seasonal cycle can also give estimates of the planet effective temperature, the variability in the obliquity of its orbit, and the distribution of land at larger scale. A further study with a Global Circulation Model combining Earth's emitted flux is ongoing.

PART IV.

PHOTOMETRIC VARIABILITY OF EARTH-LIKE PLANETS

Chapter 5

Planets in a terrestrial orbit

In this chapter, we present a study of the thermal emission of four Earth-like planets. We are interested on the effect of its physical characteristics over the climate, the global infrared emission and the shape of the thermal light curve observed at different geometries. The method applied is analogue to the study of the emission of the Earth described in Chapter 4. With the aim of obtaining a variety of climates, we have used LMD Global Climate Model data of four planets with the orbital characteristics and atmospheric composition of the Earth, whereas the rotation rate, the surface or the stellar radiation have been modified in each case. Section 5.1 is an introduction to the climate characteristics of Earth-like planets and presents the parameters used to typify each planet. The results are given in Section 5.2. Then, in Section 5.3, we build and analyze the thermal light curves of each planet. The retrieval of the planetary period is discussed in Section 5.4, and the longitudinal light curves are presented in Section 5.5.

5.1 Climate on Earth-like planets

The climate of a planet is highly compelled by its global radiative budget. The incoming stellar energy is partially absorbed and balanced by the emitted thermal energy. The latitudinal insolation gradient produces an energy gain in the tropics and a deficit in the poles, and this temperature gradient becomes the primary mechanism of the general circulation of the atmosphere, playing a key role over the climatic conditions and the thermal radiation of the planet. In equilibrium, the net radiative flux at the top of the atmosphere (TOA) across a latitude belt can be written as (Stone, 1978):

$$\frac{dF}{d\phi} = 2\pi R^2 (\cos\phi) \left[Q_\phi (1 - A_\phi) - F_\phi^{IR} \right] \tag{5.1}$$

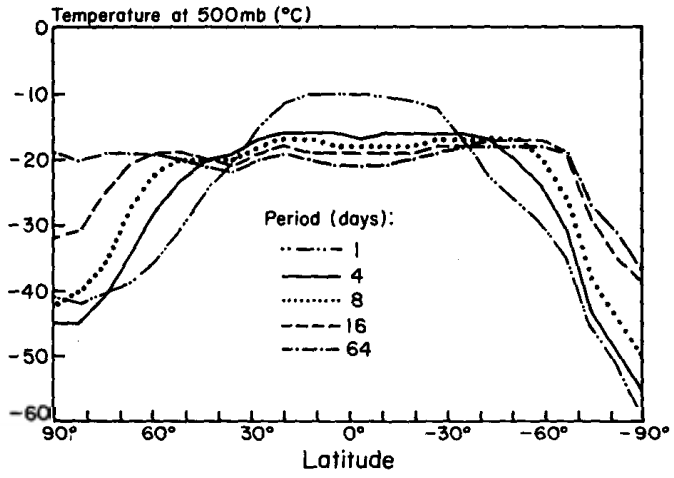

Figure 5.1 Latitudinal profiles of zonal mean 500 mb temperature at rotation periods of 1, 4, 8, 16, and 64 terrestrial days (adapted from del Genio & Suozzo (1987)). The meridional temperature gradient decreases with longer rotation periods.

where ϕ is latitude, R is the planet radius, Q_ϕ is the mean incident stellar radiation per unit area at latitude ϕ, A_ϕ is the mean albedo at latitude ϕ and F_ϕ^{IR} is the mean thermal emitted flux per unit area at latitude ϕ. In order to balance this temperature gradient, a meridional energy transport is stablished, forming the Hadley cell, which constitutes a fundamental feature of the planetary circulation. The influence of the physical characteristics of the planet (the rotation rate, the orbital parameters, the albedo or the global temperature) on the Hadley cell and its effects over the planetary climate has been studied by numerous authors:

Influence of the rotation rate.– The heat flux is related to the planetary rotation rate as a function of $(\partial\theta/\partial y)^2/f^2$, where $(\partial\theta/\partial y)$ is the local meridional temperature gradient, $f = 2\Omega\sin\phi$ is the Coriolis parameter, Ω is the angular velocity of the planet and ϕ is the latitude (Stone, 1972). The latitudinal temperature gradient is greater with faster rotation, the turbulence created by the Coriolis effect implies less efficiency on the meridional heat transport and, as a consequence the planet has warmer and wetter tropics and

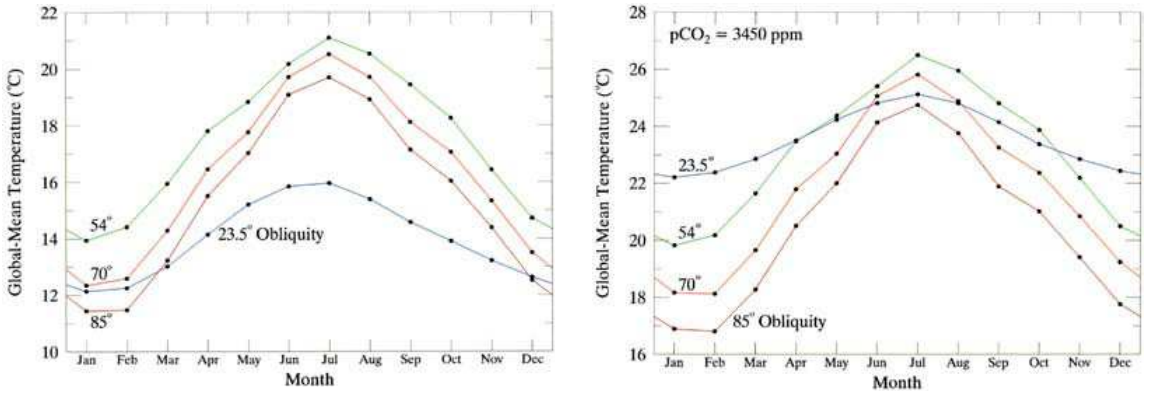

Figure 5.2 Global mean surface temperature for the present Earth (*left*) and the Earth with a high concentration of CO_2 (3450 ppm) (*right*) at planetary obliquities of 23.5° (present Earth), 54°, 70° and 85° (from Williams & Pollard (2003)).

dryer and colder subtropics. Slower rotations, on the contrary, have smaller temperature gradients because the decrease in turbulence makes the meridional heat transport more efficient (Fig. 5.1). Hadley cells are larger with warmer and moister poles and extense arid zones (Hunt, 1979). The regular 3-cell circulation pattern (Fig. 2.8) is replaced by one large Hadley cell and superrotation appears at high altitudes for periods larger than 4 days (del Genio & Suozzo, 1987).

Influence of the obliquity of the rotation axis.– Williams & Pollard (2003) (Fig. 5.2) investigates the effect of obliquity on the Earth climate (for 23.5°, 54°, 70°, and 85° of inclination) under the present conditions of the atmosphere and for high concentrations of CO_2 (3450 ppmv). Large obliquity angles ($\geqslant$54°) give extreme seasonal variations and, because of the continental distribution, the effect is specially amplified during northern summer with temperatures up to 100°C at mid-latitudes. In the case of an atmosphere with a high concentration of CO_2, the planet is globally warmer. The change on the mean surface temperature of the planet respect to the present atmosphere is particularly significant for the present Earth obliquity over higher angles of

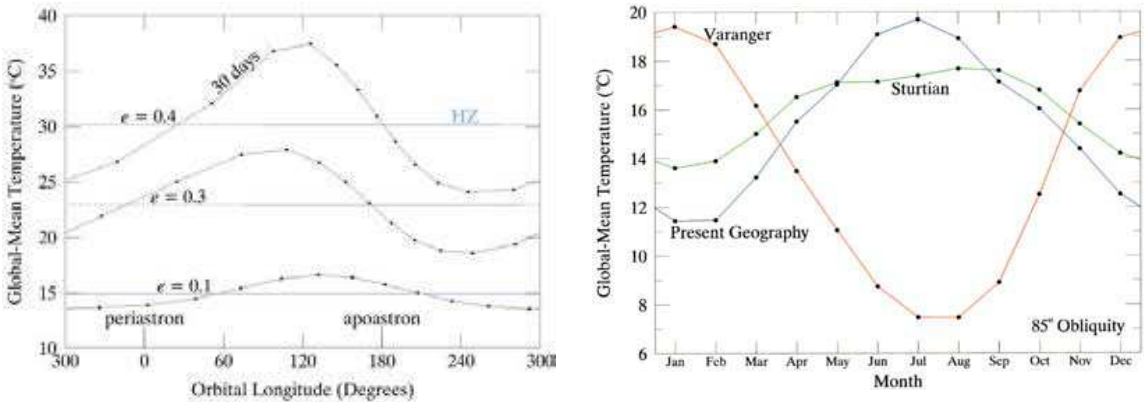

FIGURE 5.3 *Left*: Global mean surface temperature for the present Earth at eccentricities of 0.1, 0.3 and 0.4 (from Williams & Pollard (2002)), the time spent inside the HZ is indicated as a solid blue line. *Right*: Seasonal variation of the global mean surface temperature for three Earth-like planets with an obliquity of 85° and different continental distributions, the present Earth (blue) and the two paleo-climates of the Sturnian glaciation (∼750-720 Ma) with an equatorial ensemble of continents, and the Varanger glaciation (∼610-575 Ma) with a concentration of lands in the South Pole (from Williams & Pollard (2003)).

inclination of the rotation axis. The reason of this temperature increment is that the permanent and the semi-permanent snow-ice cover on the Earth poles is significantly reduced. The global temperature at higher obliquity configurations is less sensitive to an increase of CO_2, because the regions with a permanent snow-ice cover are rare and they have a little contribution to the global temperature of the planet. Although this increment in temperature is important, it is relevant to note that the planet does not turn into a runaway greenhouse (or snowball) state in any case.

Influence of the eccentricity of the orbit.– Williams & Pollard (2002) studies the effect of eccentricity on the habitability of the Earth, by testing the changes for the present Earth at eccentricity values of 0.1, 0.3, and 0.4 (Fig. 5.3

(left)). The time averaged flux $< F >$ over an eccentric orbit is given by:

$$< F > = \frac{L_*}{4\pi R_P^2 \sqrt{1-e^2}} \tag{5.2}$$

where L_* is the stellar luminosity and e is the eccentricity. Thus, at higher eccentricities, the global mean surface temperature rises. For an Earth-analogue at e=0.4, the global temperature is 15° higher, the seasonal variation is also more intense and these conditions lead to severe climates. However, the planet keeps liquid water on the surface in all the cases of the study.

Global warming impact.– An increment in the global temperature produces a tropospheric lifting and a greater static stability of the subtropics (Frierson et al., 2007). Consequently, the Hadley cell expands to higher latitudes, the jet streams and the storm tracks move poleward, the polar vortex is intensified and precipitation and moisture decrease in the subtropics (Lu et al., 2007). As a result, the subtropical regions are drier and extend to higher latitudes than on the present Earth, and therefore the planet has an extreme climate (Solomon et al., 2007).

Continental effects.– The presence of continental lands strengthens the Hadley cell transport during winter and weakens it during summer (Greene, 1998). The increase in surface friction and the development of strong monsoons are the sources of this behavior. In the case of the Earth, because of the predominance of continents on the Northern Hemisphere, they produce lower temperatures during the northern winter (NW) and higher temperatures during the northern summer (NSu) than in the absence of continents (Cook, 2003). Williams & Pollard (2003) studies three continental distributions: the present Earth, a south polar continent, similar to the Varanger glaciation (∼610-575 Ma) configuration, and an equatorial continent that corresponds to the conformation during the time of the Sturtian glaciation (∼750-720 Ma). At an obliquity of 85°, the equatorial distribution shows the mildest seasonal variation of surface temperature (∼4°), whereas the polar continental configuration suffers the most

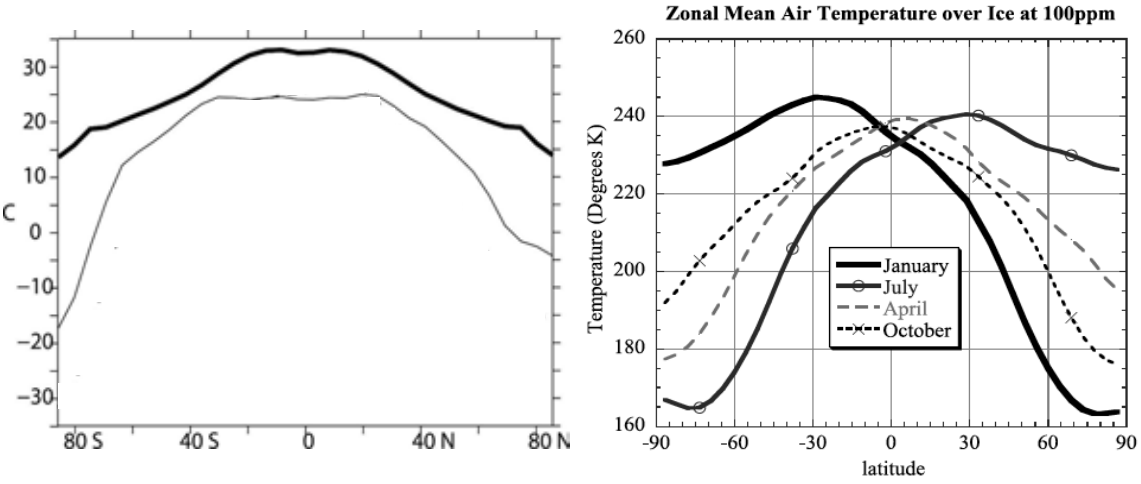

Figure 5.4 *Left*: Annual zonal average air surface temperature (°C) for an aquaplanet (thick solid), the present Earth (thin solid) (adapted from Smith et al. (2006)). *Right*: Seasonal cycle of the snowball zonal mean air temperature over the ice at a 100 ppm CO_2 concentration (from Pierrehumbert (2005)).

acute, with a change of ∼12° between the southern summer (SSu) and the southern winter (SW) (Fig. 5.3, right). In this case, the effect is amplified by the fact that the planet is near periastron – receiving a larger amount of stellar radiation– during the southern summer, and apastron during southern winter. Snow and ice cover the lands of the Varanger planet but the ocean is just covered on ice in certain areas near the coast.

Aquaplanets.– Water worlds have been proposed as possible bodies in the Habitability Zone (HZ) (Léger et al., 2003, 2004; Sotin et al., 2007). On an aquaplanet, the surface is covered by a 50 m deep slab ocean, in the absence of continents, which add surface friction and distort wind currents, the atmospheric circulation of this type of planets differs greatly from the circulation found on Earth. The distribution of the temperature field (Fig. 5.4, left) is essentially zonal (Smith et al., 2006) with a slight hemispherical asymmetry due the eccentricity of Earth's orbit, because of a higher insolation during the

SSu than during the NSu. Although the wind field is also zonal with jets both in the atmosphere and the ocean, the meridional heat transport is very effective, favored by the ocean Ekman transport on the subtropics that causes a meridional transport of water, and the eddy-driven subduction, that allows the exchange of water masses between the ocean surface and its interior (Smith et al., 2006; Marshall et al., 2007; Codron, 2012). The annual mean surface temperature of an Earth-like aquaplanet is 300 K, with a temperature gradient from 286 K on the poles to 306 K on the subtropics. The polar ice has a great influence on the climate as it increases the planetary albedo and at the same time absorbs a certain amount of heat that it is driven poleward in order to maintain equilibrium. The polar ice caps on the Earth-like aquaplanet reach $\sim 55^{\circ}$ latitude (Marshall et al., 2007). Smith et al. (2006) and Enderton & Marshall (2009) showed that continental barriers prevent the formation of polar ice caps.

Snowball planets.– The snowball Earth hypothesis sets that the planet surface became entirely frozen ("hard snowball" state) or nearly entirely frozen ("slush snowball" state) more than 650 Ma ago. This state might have been produced by several factors such as a decrease of the stellar energy, perturbations in the planetary orbit, a reduction of the atmospheric concentration of greenhouse gases or an increment in the volcanic activity. Any of these circumstances can derive in an initial cooling of the planet that would lead to a snowball state. The ice cover increases the global albedo, lowering the temperature of the planet and reinforcing the creation of ice and snow in a positive feedback. Because of the low concentration of water vapor in the atmosphere, surface temperatures drop below 170 K with a maximum temperature of 240 K, which 30 degrees below deglaciation, for the hard snowball (Fig. 5.4, right) (Pierrehumbert, 2005). Although in general a decrease in the stellar radiation or a decrease in the concentration of greenhouse gases can produce a snowball state, the planet remains globally iced despite an increase of solar energy to a present solar constant – in case the agent of glaciation was

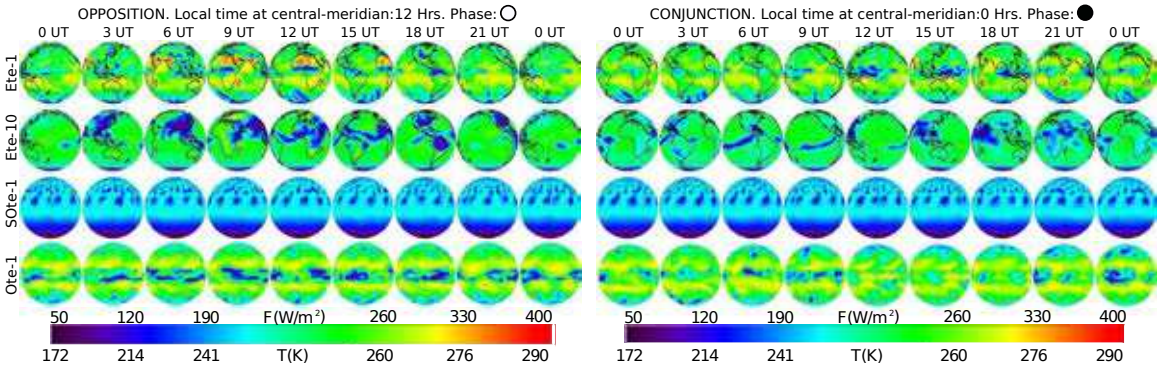

FIGURE 5.5 TOA-all-sky flux/brightness temperature towards an observer at opposition (left) and conjunction (right) during one rotation (UT time) at northern summer for the terrestrial planets (from top to bottom) Ete–1, Ete–10, SOte–1, and Ote–1.

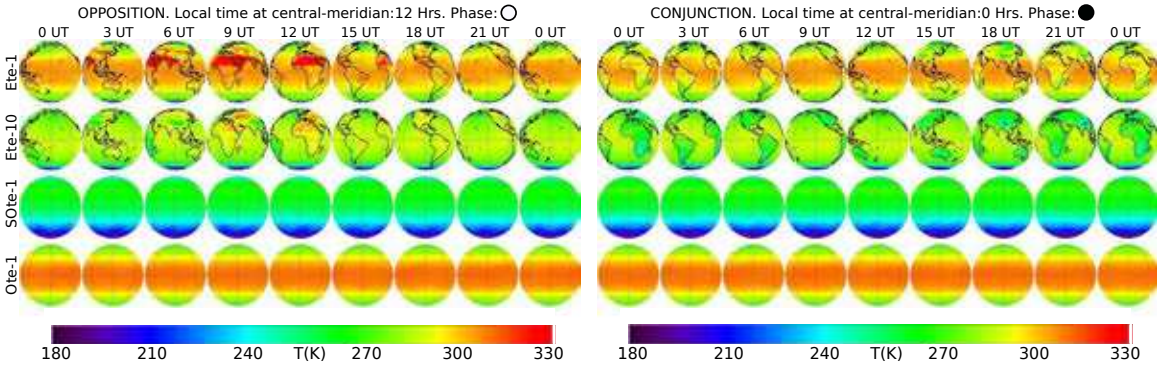

FIGURE 5.6 Surface temperature towards an observer at opposition (left) and conjunction (right) during one rotation (UT time) at northern summer for the terrestrial planets (from top to bottom) Ete–1, Ete–10, SOte–1, and Ote–1.

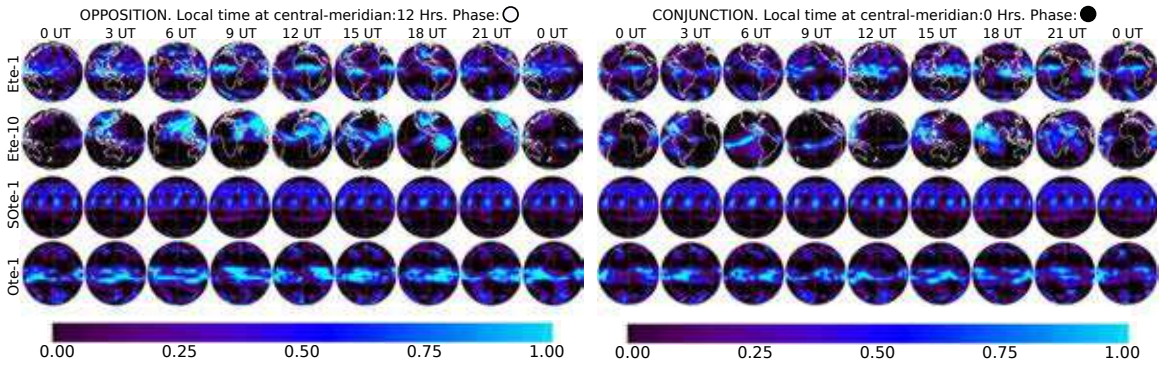

FIGURE 5.7 High cloud fraction for an observer at opposition (left) and conjunction (right) during one rotation (UT time) at northern summer for the terrestrial planets (from top to bottom) Ete–1, Ete–10, Ote–1, and SOte–1.

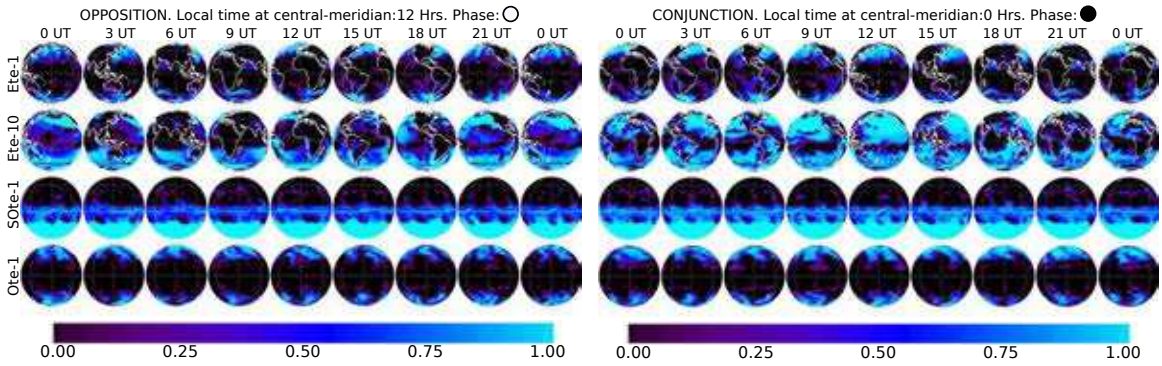

FIGURE 5.8 Low cloud fraction for an observer at opposition (left) and conjunction (right) during one rotation (UT time) at northern summer for the terrestrial planets (from top to bottom) Ete–1, Ete–10, Ote–1, and SOte–1.

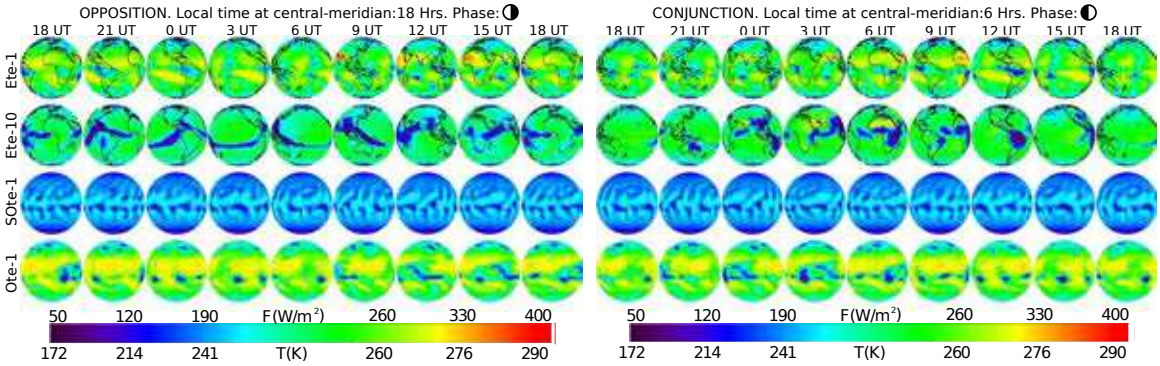

FIGURE 5.9 TOA-all-sky flux/brightness temperature towards an observer at opposition (left) and conjunction (right) during one rotation (UT time) at northern spring for the terrestrial planets (from top to bottom) Ete–1, Ete–10, SOte–1, and Ote–1.

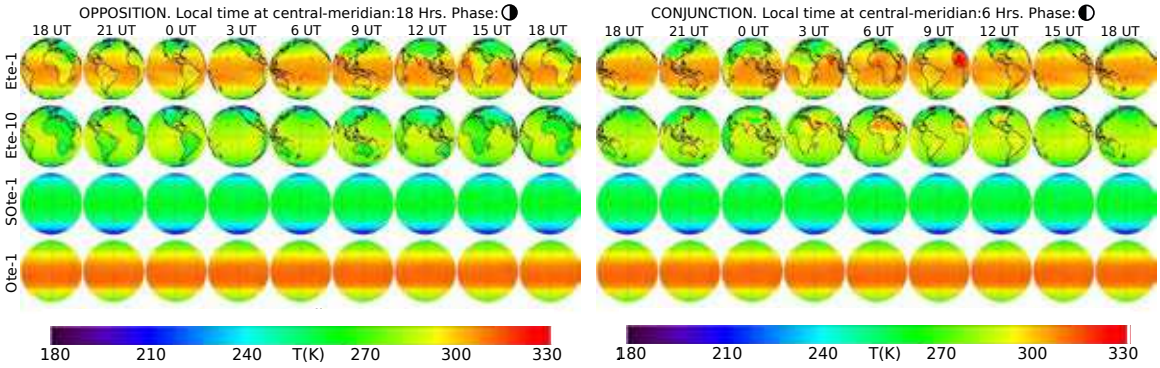

FIGURE 5.10 Surface temperature towards an observer at opposition (left) and conjunction (right) during one rotation (UT time) at northern spring for the terrestrial planets (from top to bottom) Ete–1, Ete–10, SOte–1, and Ote–1.

Table 5.1. Planetary specifics

	Rotation period (sidereal days)	Type of planet
Ete–1	1	Earth-like
Ete–10	10	Earth-like
Ote–1	1	Aquaplanet
SOte–1	1	Snowball Aquaplanet

Note. — **Notation**: *E*–earth-like, *O*–ocean planet, *S*–snowball, *t*–tilted, *e*–Earth's eccentricity, –(rotation period); i.e. *Ete-1* corresponds to the Earth. All the planets have Earth's orbital configuration: obliquity= 23.44°and eccentricity= 0.0167.

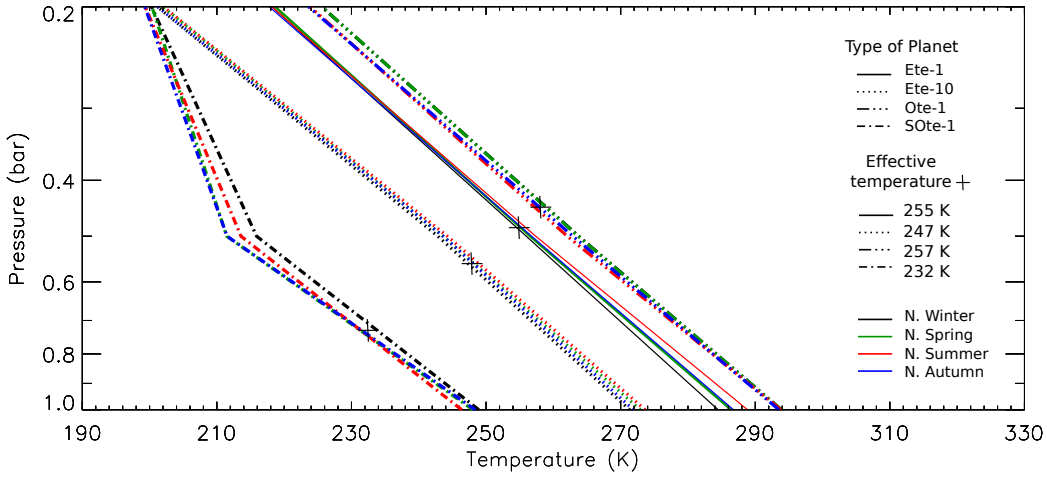

Figure 5.11 Atmospheric profiles for Ete–1, Ete–10, Ote–1, and SOte–1. Colours correspond to different points on the orbit, representing northern hemisphere seasons: winter (black), spring (green), summer (red), and autumn (blue).

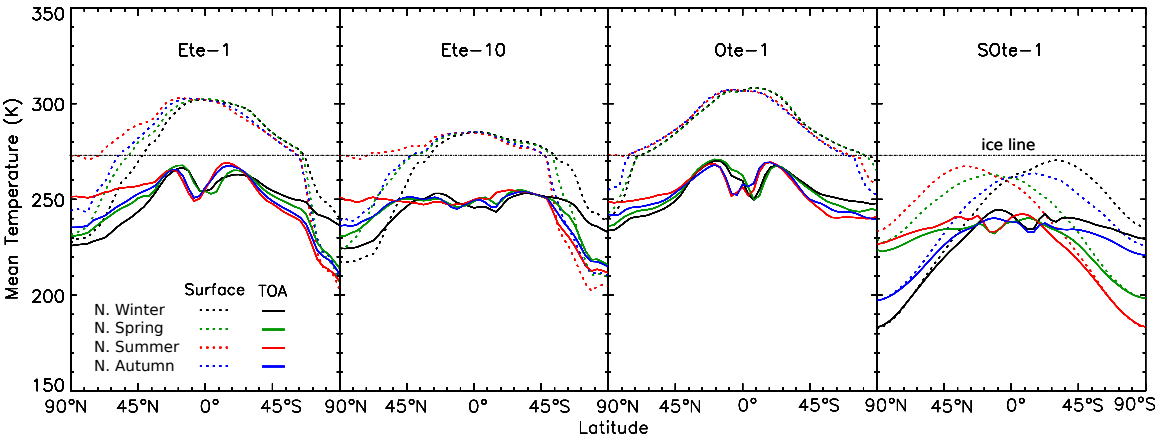

Figure 5.12 Mean temperature vs latitude at surface (dotted) and TOA brightness temperature vs latitude (solid) for the terrestrial planets Ete–1, Ete–10, Ote–1, and SOte–1. Colours represent orbital fraction and the corresponding seasons in the northern hemisphere: winter (black), spring (green), summer (red), and autumn (blue).

a decrease in the stellar energy–, or despite of a CO_2 concentration change to ∼10 times the present atmospheric level (PAL) (3480 *ppmv*). However, ice melting is produced at CO_2 concentrations of ∼100 PAL and result in lower fractions of ice covering than present Earth (Marotzke & Botzet, 2007).

5.1.1 Data

In this study, we have used LMDZ GCM data (Section 3.2) to build four different planets varying the rotation rate (1 or 10 days) and the planetary surface (Table 5.1). All the planets have the atmospheric composition, the axial tilt and the orbital configuration of the Earth. We have reproduced the Earth (Ete–1), in order to validate the application of the data. Then, we have built an Earth-like planet with a rotation period of 10 days (Ete–10), an Earth-like aquaplanet (Ote–1) and a hard-snowball aquaplanet (SOte–1) on which the solar constant has been diminished to 80% in order to achieve the snowball state.

Table 5.2. Global parameters of radiation

	T_{eff} [a](K)	A	CRF (W/m^2)	g_N	T_S(K)
Ete–1	255	0.30	-27.2	0.39	287
Ete–10	248	0.37	-27.5	0.31	272
Ote–1	258	0.26	-28.7	0.41	294
SOte–1	233	0.51	-16.7	0.22	248

Note. — The effective temperature T_{eff}, Bond albedo A, normalized greenhouse parameter g_N, cloud radiative forcing CRF and surface temperature T_S are determined according to the calculations shown in Section 2.2.

[a]The temperature uncertainty is $\pm 5{\cdot}10^{-4}K$, the precisions shown in the table are chosen for simplicity.

Table 5.3. Characteristics of the Troposphere[a]

	H (km)	N (σ_N) ($10^{-5}s^{-1}$)	L (σ_L) (10^{-3})	l (σ_l) (km)	a (σ_a) (K/km)	Δ_T	Ro_T
Ete–1	8.402	1250 (30)	238 (3)	1520 (20)	5.9 (0.6)	0.229	0.02
Ete–10	7.970	1300 (20)	746 (7)	4760 (40)	5.9 (0.6)	0.181	1.79
Ote–1	8.594	1230 (30)	239 (3)	1520 (20)	5.9 (0.2)	0.131	0.01
SOte–1	7.224	1140 (60)	211 (6)	1350 (20)	6.5 (0.2)	0.157	0.01

Note. — Stratification vs Rotation: H is the scale height, N is the Brunt-Väisälä frequency, L is the normal Rossby deformation radius, l is the Rossby deformation radius, a is the tropospheric lapse rate, Δ_T is the non-dimensional meridional temperature gradient, and Ro_T is the thermal Rossby radius (calculations according to Section 2.2.3).

[a]The values are restricted to the tropospheric pressure levels of each planet (Fig. 5.11).

5.2 Planetary characteristics

With the purpose of doing the comparative study the climate of these four planets, we have derived certain parameters from the planetary emission maps. Those parameters, presented in Section 2.2, are: the mean effective temperature T_{eff}, the Bond albedo A, the greenhouse parameter g, the mean surface temperature T_S, the cloud radiative forcing CRF, and the Rossby deformation radius l_R. The results are shown in Table 5.2 and Table 5.3. Figure 5.11 presents the atmospheric profiles of each planet and Figure 5.12 shows the mean surface temperature and the mean brightness temperature as functions of latitude for each season.

5.2.1 The Earth

The results of the global parameters of the planet (Table 5.2) are in agreement with satellite observations (Trenberth et al., 2009). The tropospheric profile (Fig. 5.11) shows the predominance of the planet northern hemisphere, warmer during northern summer and colder during northern winter although they correspond to the apastron and periastron positions respectively. This effect is given by the asymmetric distribution of the continental masses on the planet (Chapter 4, Gómez-Leal et al. 2012), and the surface temperature varies from 285-290 K with seasons.

The subtropical regions, where the circulation is driven by the Hadley cells and represented by the flat central zone of the surface temperature meridional gradient (STMG) (Fig. 5.11, dash), extend to $\sim$30° in latitude in both hemispheres and have a mean temperature of $\sim$300 K. The ice layer reaches $\sim$45°N during northern winter, and becomes a half-iced cap at $\sim$10°N during summer. In the South, the permanent polar cap of the Antarctica extends to $\sim$60°S. The polar surface temperatures vary from 230-270 K in the North and 200-240 K in the South.

At mid-latitudes, there is an asymmetry in the meridional surface temperature of both hemispheres. This difference in temperature is the result of the uneven distribution of land on Earth. The predominance of oceans in the southern hemisphere

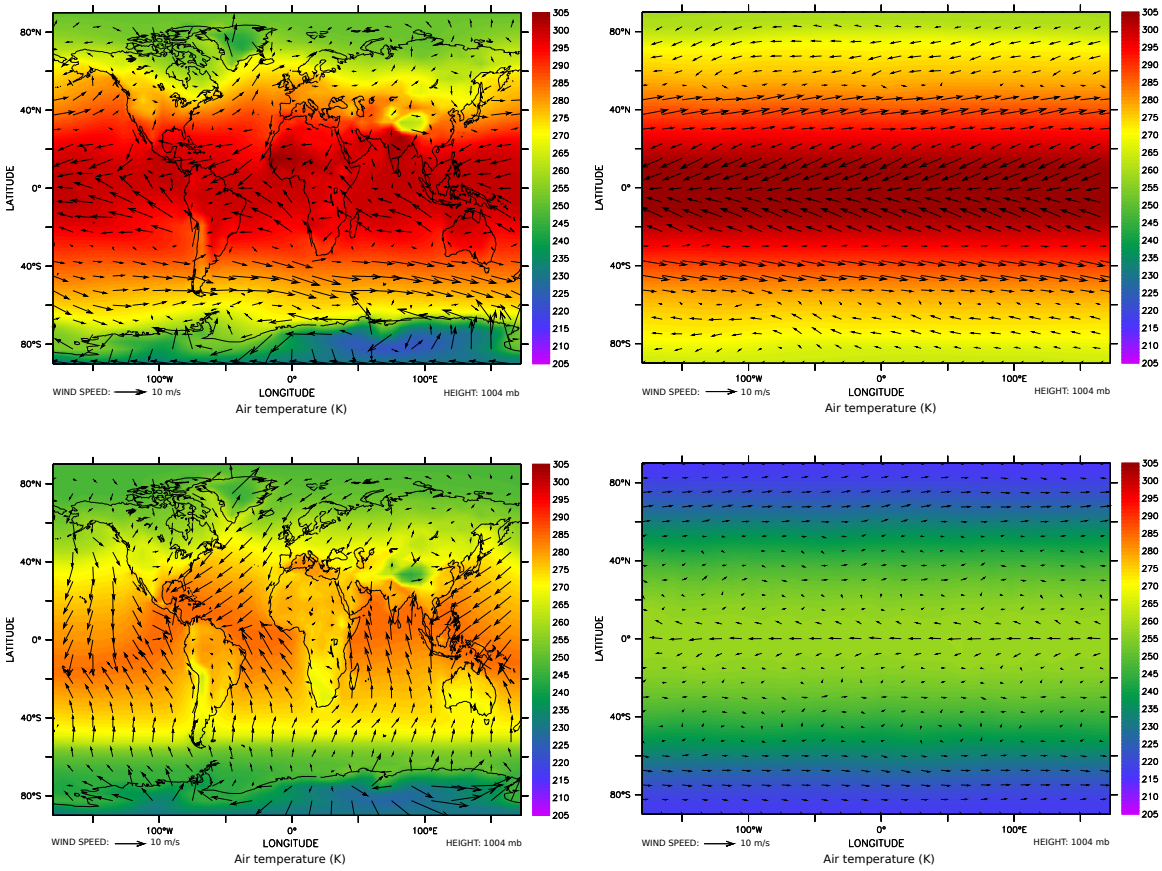

FIGURE 5.13 Mean surface temperature and mean surface wind field for Ete–1 (top-left), Ote–1 (top-right), Ete–10 (bottom-left) and SOte–1 (bottom-right).

produces a small seasonal variation in surface temperature due to the high thermal inertia of water. In contrast, the large continental masses in the northern hemisphere produce a larger variation because in general the emissivity of bare land (summer) is higher than the emissivity of water, whereas the emissivity of snow (winter) is lower.

The brightness temperature meridional gradient (BTMG) (Fig. 5.11, solid) decreases near the Equator, because of the absorption of convection clouds that condense over the Intertropical Convergence Zone (ITCZ). The ITCZ moves from one side to the Equator to the other, following the latitudinal change of the ecliptic

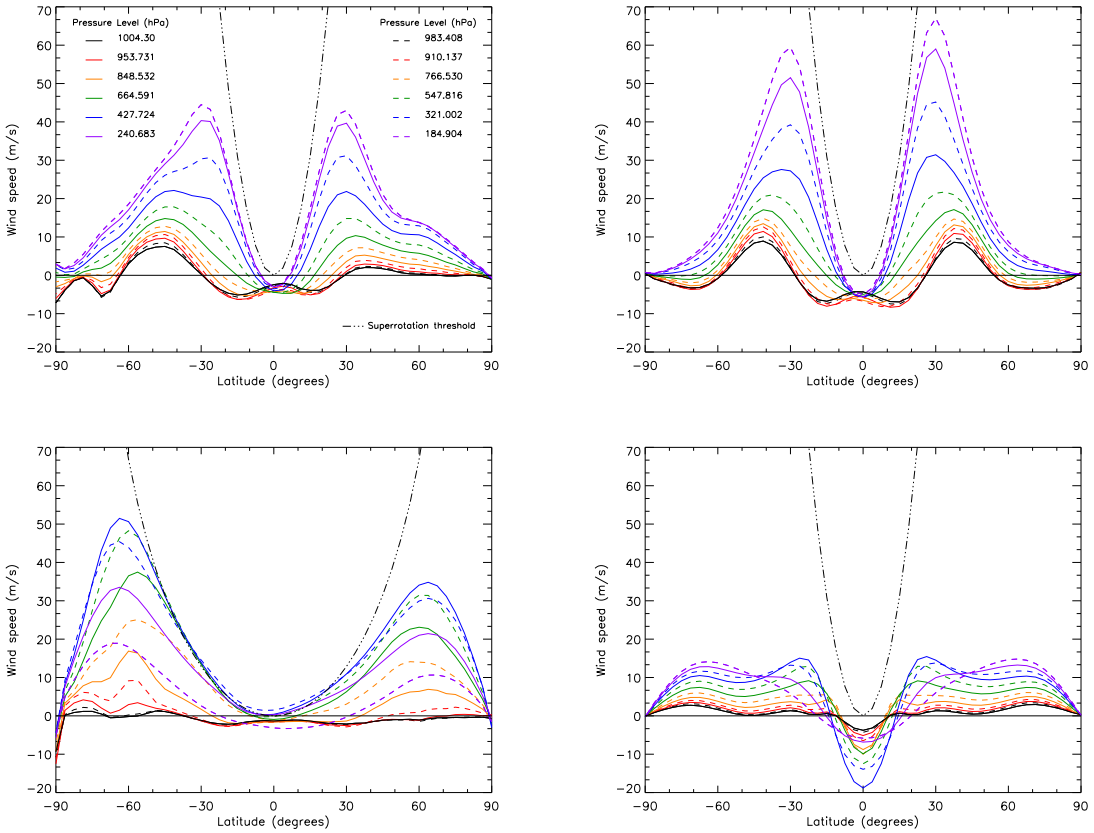

Figure 5.14 Mean zonal annual wind for the tropospheric levels of Ete–1 (top-left), Ote–1 (top-right), Ete–10 (bottom-left), and SOte–1 (bottom-right). Superrotating winds lie above the wind speed limit u_L(dash-dot black line), described in Section 2.2.3.

with seasons. The absorption is more relevant in the northern hemisphere, as the result of the continental distribution: the seasonal shifts of the ITCZ and the great seasonal temperature and humidity differences between the continent and the ocean create monsoons, which are particularly important on India and Indonesia (Philander et al., 1996). Figure 5.5 (northern summer) and Figure 5.9 (northern spring) show the TOA-emission flux of the Earth (Ete–1). We can distinguish the ITCZ clouds, the temperature differences between the subtropical regions and the rest of the planet, and the diurnal cycle of the arid zones, especially on the Sahara desert. There is

a large fraction of high clouds in the planet (Fig. 5.7), the clouds along the ITCZ have two stable zones, one over Indonesia and the other over the african equatorial savanna, whereas low clouds condense over the cold polar oceans (Fig. 5.8).

Figure 5.13 (top-left) shows the patterns of the mean horizontal surface wind field, with the convergence at the convection region of the ITCZ at the Equator, where the Hadley cells of each hemisphere meet and specially the convergence of winds over Indonesia, because of the coincidence of the Hadley and the Walker cells (a circulation over the Pacific ocean). The results of Earth's tropospheric parameters (Table 5.3) are in agreement with the literature (e.g., Mitchell & Vallis 2010). Figure 5.14 illustrates the zonal wind speed at several pressure levels of the troposphere. The figure shows that Earth zonal winds are outside the region of superrotation, where the speed is higher that the rotation of the solid body (region inside the black dot-dash-line), and the planet does not present superrotation by any of the criteria of Section 2.2.3, u$<$ u$_L$, Ro$_T$ $<$ 1.3 (Mitchell & Vallis, 2010), and L$_R$ $<$ 1 (del Genio & Suozzo, 1987) (Table 5.3). The Southern Hemisphere shows higher wind velocities than the Northern Hemisphere because of a greater latitudinal temperature gradient ($U_T \sim T_S \Delta_T$, from Eq. 2.14).

5.2.2 The slow Earth

In order to study the effects of the rotation period over the climate, we have study the case of an Earth with a rotation period of 10 days. Because of the weaker Coriolis force, the meridional transport is very effective and the global climate is colder (Fig. 5.11). The Hadley cells extend to higher latitudes with colder subtropical temperatures (Fig. 5.12). In summary, Ete–10 has lower mean surface temperature (272 K) and effective temperature (248 K), slower zonal winds, a diurnal convection cloud formation cycle over the continents and a thick layer of low clouds over the oceans (Fig. 5.8). As a consequence of the cold surface temperature (maximum$\sim$280 K), the seasonal variability is lower than on Earth.

The incoming stellar radiation is largely reflected by low clouds (high albedo), cooling the planet, and as a result a vast part of the surface is frozen (δ_{ice} $\geq$40° latitude). Convection clouds are formed along the ITCZ, which in this case is modified by the dominant meridional winds (Fig. 5.13).

It is interesting to note that as a consequence of the temperature contrast between the continental land and the ocean (Figs. 5.5 and 5.6), convection clouds also condense over large continental regions, in this case as massive monsoons. The absorption of light produced by these clouds is the cause of the general decrease in the brightness temperature along the subtropical regions (Fig. 5.12). The diurnal cycle influence the condensation of high clouds, which is increases during the afternoon. During summer, the cloud cover of the asian monsoon extends from Papua to half of Siberia (Fig. 5.7) and another monsoon covers America with the only exception of the Southern Cone.

Figure 5.13 (bottom-left) shows the predominance of the meridional component of the horizontal wind field and the modification of the ITCZ. The scale height H and the Brunt–Väisäla frequency N are modified by temperature (Table 5.3), whereas the Rossby deformation radius is determined by the rotation rate Ω_r. As on Earth, the distribution of the continents also determine the wind circulation, but here the surface winds are slower due to the low temperatures. Figure 5.14 (bottom-left) shows that there is a faint equatorial superrotation regime at the upper levels of the troposphere, confirmed by a value of the thermal Rossby number greater than 1.3 (Ro_T= 1.79). However, the criteria of a L_R >1 for a superrotation regime differs with the results (L_R= 0.746).

5.2.3 The Earth-like aquaplanet

In the absence of continents, the atmospheric circulation of an aquaplanet such as Ote–1 is less complex than in the case of terrestrial planets: The meridional gradient of the stellar insolation determines the temperature of the planet and its distribution.

The large surface specific humidity of the planet (50% higher than Earth's levels, Kalnay et al. 1996) favors the production of high clouds, the greenhouse effect is larger (Table 5.2) than on Earth, and as a consequence, the aquaplanet analogue has a warmer global surface temperature (Fig. 5.11).

The seasonal temperature variation in the highest part of the troposphere is given by the change in high cloud fraction, whereas the surface temperature does not vary considerably because of the large thermal inertia of water. The subtropical surface temperature rises to 310 K, the polar caps melt in summer, in winter (Fig. 5.12) the North Pole have a surface temperature of ∼240 K, whereas the South Pole winter reaches ∼260 K. We can see the effect of the eccentricity of the orbit, as the southern summer (at periastron) is slightly warmer than the northern one (at apastron). Figures 5.5 and 5.6 show the temperature dependence with latitude, with a large extension of the cloudy ITCZ and formation of low clouds over the polar regions.

The planet has a zonal wind pattern analogous to Earth without superrotation, and a similar tropospheric parameters (Table 5.3). However, in this case the higher wind speeds are in the Northern Hemisphere (Fig. 5.14) and have a different origin, because of the eccentricity of the orbit the mean surface temperature is slightly higher in the tropics during the southern summer (Fig. 5.12, black dash line), and specially in the south pole where the ice cap almost disappears, at the same time a large temperature gradient is created in the northern hemisphere ($U_T \sim T_S \Delta_T$) to maintain equilibrium, and then the north polar ice cap increases, reaching ∼70 degrees in latitude. As a result, winter surface temperatures are more severe at the North Pole than at the South Pole (red dash line).

5.2.4 The Snowball aquaplanet

In the case of the snowball planet SOte–1, the surface is completely frozen; with a mean surface temperature of 248 K (∼40 degrees colder than the Earth). The snow

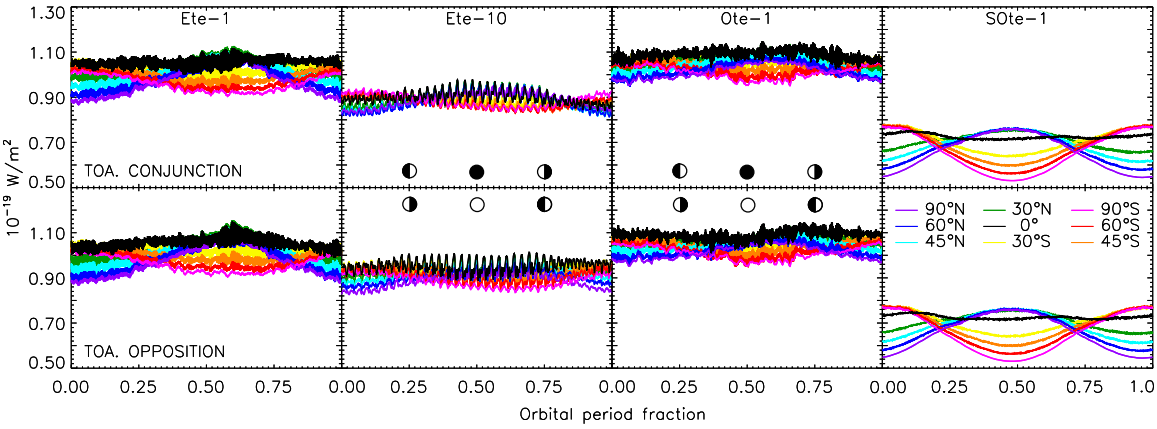

FIGURE 5.15 TOA-all-sky flux orbital series for the terrestrial planets Ete–1, Ete–10, Ote–1, and SOte–1, for an observer at conjunction (top row) and at opposition (bottom row). The circles indicate the illumination phase of the planet for an observer at the ecliptic plane.

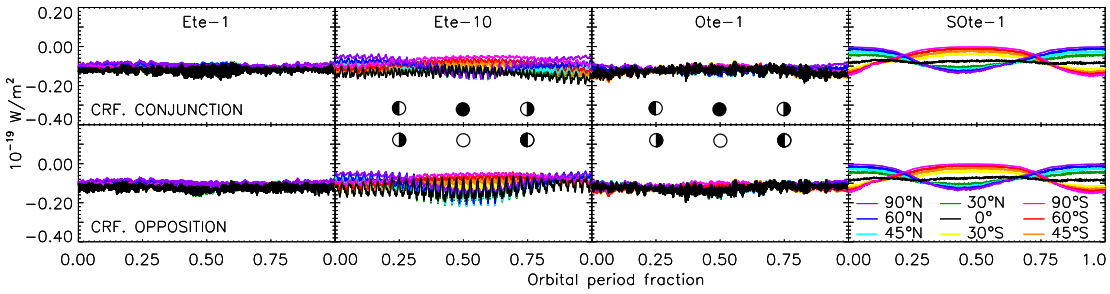

FIGURE 5.16 Corresponding cloud radiative forcing (CRF) for the terrestrial planets Ete–1, Ete–10, Ote–1, and SOte–1 during one orbit for an observer at conjunction (top row) and at opposition (bottom row). The circles indicate the illumination phase of the planet for an observer at the ecliptic plane.

and the high production of low clouds increase the planetary albedo (Table 5.2). The effective temperature is ∼233 K and the troposphere is constricted to higher pressure levels (∼0.7 bar) (Fig. 5.11). As in the aquaplanes, being at periastron the Southern summer is warmer, with an annual mean surface temperature of ∼270 K

in the regions that are most exposed to solar radiation (Fig. 5.12). Because of the general cold temperatures of the planet, zonal winds are very slow, and the poles are dry and very cold (180-240 K). The rate of cooling of a rising saturated parcel of air depends on the moisture content of the air, and then since cold air has less moisture content, the lapse rate a is higher than in the rest of planets (Fig. 5.11 and Table 5.3).

During winter the whole hemisphere is covered by a thick homogeneous layer of low clouds (Fig. 5.8) and winds are very slow (Fig. 5.14). During summer, there is a condensation of convective clouds mainly near the equator. These clouds are periodically distributed over the surface of the summer hemisphere, because the convective movements are in the scale of the space resolution. High clouds would have a different distribution in a real snowball planet. Taking in account this numerical artifact, the essentials of our results on the planetary characteristics and on the analysis of the signal of the planet do not change. Therefore, we have decided to consider these data in our study. Again because of the low surface temperature gradient, meridional winds are very slow, and the planet does not show superrotation.

5.3 Time series

In this section, we present the analysis of the orbital light curves and the physical parameters that have an influence on the signal. Figure 5.15 represents the orbital thermal light curve of the planet for observers at conjunction and observers at opposition for several inclinations of the planetary view, labeled by the latitude of the sub-observer's point. To study the effect of clouds on the signal, we have calculated the Cloud Radiative Forcing (CRF) (Section 2.2) at any time of observation. Figure 5.16 gives the CRF correspondent to the time series. As the clouds absorb the emission from below, CRF (=$F_{all-sky}$ - F_{clear}) is a negative magnitude. Table 5.4 presents the time series variability. It is also useful to associate the time series with the rotation maps from Figure 5.5 to Figure 5.10.

5.3.1 The Earth (Ete–1)

Comparing the light curves obtained at conjunction and at opposition of Figure 5.15, we do not observe a substantial difference in flux with a change in the planetary phase angle. The signal shows a combination of several effects: the large modulation reprints the seasonal cycle with a predominance of the NH because of the uneven distribution of continents, and the smaller variability is due to the passage of warm regions (Sahara) and cold regions (Indonesia) (Chapter 4) with the rotation of the planet. The cloud production is higher during summer, specially in the NH, due to the temperature increase.

5.3.2 The slow Earth

As in the case of the Earth, the light curve of Ete–10 has also a seasonal and a rotational variation. However, the slow Earth is a colder planet, the rotational modulation due to warm spots is rare. In this case, we can see the rotation of the planet because there is a difference in the emission with the illumination phase of the planet, due to the diurnal cycle of high clouds. The massive condensation of clouds over the continents produce a strong modulation with the rotation of the planet. High clouds condense massively during daylight, absorbing the planetary emission and producing a decrease in brightness temperature. The cloudy regions appear as large cold spots over the continents and the contrast between the clear and the cloudy regions produce the oscillation seen in Figure 5.15. The production of clouds is more important for low latitudes and particularly during northern summer (Fig. 5.16). Being a colder planet, the orbital variability of the Northern Hemisphere is lower than on Earth (Table 5.4) However, the orbital variability of the Southern Hemisphere is similar in both planets because of the predominancy of the oceans, which have a low thermal inertia.

Table 5.4. Time series variability

	Variability	Orbital phase	Latitude								
			90	60	45	30	0	-30	-45	-60	-90
Ete–1	Rotation	[0,1/12]	3	5(4)	6(5)	6(5)	6(4)	5(4)	4(3)	3(3)	2
		[4/12,5/12]	3	4(5)	5(6)	5(7)	4(6)	4(5)	4(5)	3(4)	2
		[7/12,8/12]	3	5(6)	6(8)	7(9)	7(9)	6(7)	5(5)	3(4)	2
		[10/12,11/12]	3	6(5)	6(6)	7(6)	6(5)	5(4)	4(4)	3(3)	2
	Orbit	[0-1]	19	17(15)	14(12)	11(9)	5(3)	4(6)	6(8)	8(9)	10
Ete–10	Rotation	[0,1/12]	2	4(3)	4(4)	5(5)	4(6)	4(6)	4(6)	3(5)	3
		[4/12,5/12]	3	6(5)	6(6)	6(7)	7(8)	5(7)	4(6)	3(4)	3
		[7/12,8/12]	4	7(8)	8(9)	9(10)	10(11)	8(9)	6(7)	4(4)	3
		[10/12,11/12]	3	6(4)	6(5)	7(6)	6(7)	5(7)	4(6)	3(5)	3
	Orbit	[0-1]	10	11(8)	11(7)	10(5)	6(3)	5(5)	6(6)	8(7)	9
Ote–1	Rotation	[0,1/12]	2	4(3)	4(4)	5(4)	5(4)	5(4)	4(4)	4(3)	2
		[4/12,5/12]	2	4(4)	5(5)	6(6)	6(7)	6(7)	5(6)	4(5)	2
		[7/12,8/12]	1	3(4)	4(5)	5(6)	6(7)	6(7)	5(6)	4(5)	2
		[10/12,11/12]	1	3(4)	4(5)	5(6)	6(7)	5(7)	5(6)	4(5)	2
	Orbit	[0-1]	8	8(6)	8(5)	7(3)	5(4)	5(7)	6(8)	8(9)	9
SOte–1	Rotation	[0,1/12]	2	2(2)	2(2)	1(1)	1(1)	1(1)	1(1)	1(1)	1
		[4/12,5/12]	2	2(2)	2(2)	1(1)	1(1)	2(2)	2(2)	3(3)	3
		[7/12,8/12]	1	1(1)	1(1)	1(1)	1(1)	2(1)	2(2)	2(2)	2
		[10/12,11/12]	3	3(2)	2(2)	2(2)	1(1)	2(2)	2(2)	2(2)	2
	Orbit	[0-1]	33	27(27)	22(21)	14(14)	4(5)	18(19)	25(26)	31(31)	36

Note. — Mean amplitude values of rotational and orbital variability of the time series of the following planets: Earth (Ete–1), slow Earth (Ete–10), aquaplanet analogue (Ote–1), and snowball (SOte–1) at opposition and conjunction (in parentheses) for several sub-observer's point latitudes. Values are calculated as the percentage over the mean value. Rectangles contain latitudes at summer.

5.3.3 The Earth-like aquaplanet

As shown in the previous section, Ote–1 is globally warmer than the Earth. There is a seasonal variation due to insolation change produced by the tilt of the rotation axis. The high thermal inertia of water prevents from having any contrast between day and night (opposition-conjuntion views) and the presence of clouds is the only factor that produces the rotation variability of the signal. The CRF is slightly larger during the summer noon.

5.3.4 The Snowball aquaplanet

During winter, as the atmosphere is very cold, dry, with little circulation and low clouds cover the surface, the surface emission is not significantly disturbed and the thermal light curve strongly depends on the inclination of observation. However in summer, as the atmosphere becomes warmer, the circulation of the atmosphere is enhanced, convective clouds are produced and then the whole hemisphere has similar brightness temperatures Figure 5.12. The CRF is larger during the southern summer day, as the summer of the southern hemisphere is more extreme because of the eccentricity of the orbit.

5.3.5 Observed parameters

Table 5.5 shows the results for the mean effective temperature and the albedo for an observer at opposition and at conjunction (in parentheses) at several sub-observer latitudes. Perspective favors the brightness temperatures near of the sub-observer point. for that reason low latitudes show warmer temperatures than the global mean, high latitudes have colder values, and mid-latitudes ($\sim 30^\circ$) being more temperate, have similar values to the global mean.

On the slow Earth, despite the large modulation due to convection clouds, the mean effective temperature is higher than the global value for an observer at opposition (who sees the winter–night and summer–day), whereas at conjunction

Table 5.5. Observed parameters

		Global	Latitude								
		Value	90	60	45	30	0	-30	-45	-60	-90
Ete–1	T_{eff} (K)	255	252	253	254	256	257	256	254	253	252
	Albedo	0.29	0.33	0.32	0.30	0.28	0.27	0.29	0.30	0.32	0.33
	$\mathcal{T}$(days)	0.99	1.00	1.00	1.00	1.00	1.00	1.00	1.00	1.00	0.63
Ete–10	T_{eff} (K)	248	247	(246) 248	(246) 249	(247) 250	(247) 251	(247) 250	(246) 249	(246) 248	246
	Albedo	0.37	0.38	(0.38) 0.37	(0.39) 0.36	(0.38) 0.35	(0.37) 0.33	(0.38) 0.35	(0.39) 0.36	(0.39) 0.37	0.38
	$\mathcal{T}$(days)	9.997	10.00	10.00	10.00	10.00	10.00	10.00	9.88	10.00	9.88
Ote–1	T_{eff} (K)	258	255	256	257	258	260	258	257	256	255
	Albedo	0.26	0.30	0.29	0.27	0.26	0.24	0.26	0.27	0.29	0.33
	$\mathcal{T}$(days)	0.997	0.63	1.00	1.00	1.00	1.00	1.00	1.00	1.00	0.63
SOte–1	T_{eff} (K)	233	229	230	232	233	235	233	231	230	228
	Albedo	0.51	0.54	0.53	0.52	0.50	0.49	0.50	0.52	0.53	0.54
	$\mathcal{T}$(days)	0.997	0.63	1.00	1.00	1.00	1.00	1.00	0.88	0.63	0.63

Note. — Observed parameters from the time series: effective temperature T_{eff} (Eq.2.11), albedo (Eq.2.12) and rotational period $\mathcal{T}$ (Eq.2.20) for the planets Ete–1, Ete–10, Ote–1, and SOte–1 at opposition and at conjunction (in parentheses) for several sub-observer's point latitudes. Values are calculated as the percentage over the mean value.

(where the observer sees the winter-day and the summer-night) the values are lower than the global mean, because for a planet with a continental distribution similar to the Earth, the influence of continents prevails over the eccentricity effect (see Table 5.5 and Figure 5.15). Both hemispheres have the same mean effective temperature by latitude but the variability is higher for the NH, where the continental masses are larger. This implies that the northern hemisphere is both warmer and colder than the southern one. As albedo is derived from the effective temperature (Equation 2.9), a lower effective temperature imply higher albedos, which agrees with the fact that an observer at conjunction (who sees the summer-night) sees a higher concentration of low clouds that reflect the solar radiation and increase the albedo values (Table 5.5 , in parenthesis).

In Ote-1 and SOte-1, the rotational variability is similar in both hemispheres, the seasonal variability is higher for the Southern Hemisphere due to the eccentricity of the orbit, as the SSu occurs near the periastron, where the planet suffers a higher degree of solar radiation, producing higher global temperatures. At the opposite place of the orbit, the situation is different. In Ote-1, the SW is also warmer, because the planet develops a large polar ice cap during the NW, as we have previously explained. However in SOte-1, SW is slightly colder, as the planet is already cover with ice, heat transport is very low and the temperature is determined by the eccentricity of the orbit.

5.4 Rotational periodicities

In Chapter 4, we have seen how the autocorrelation of the time series can be used to find the periodicities of planet light curves (Pallé et al., 2008; Gómez-Leal et al., 2012). This method is limited by three factors:

i) The number of periods contained in the series.– The average over a large number of periods reduce the uncertainty of the results.

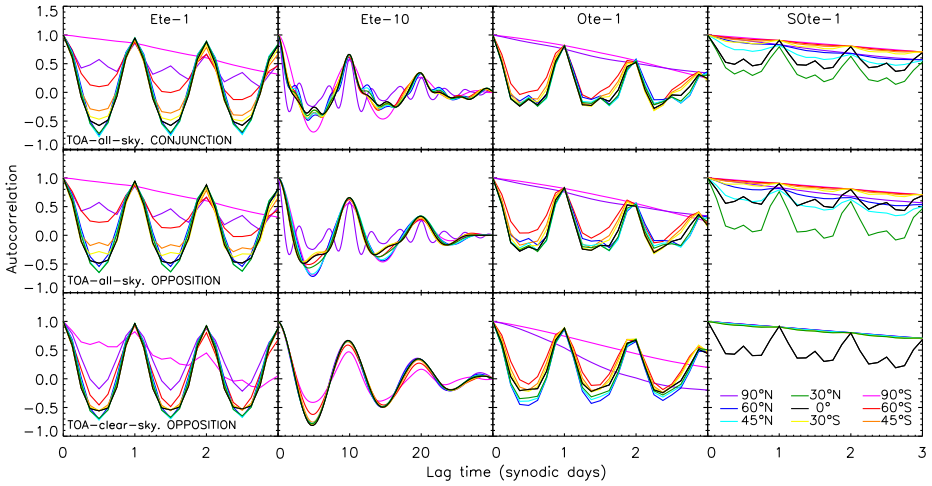

FIGURE 5.17 Autocorrelation series for the terrestrial planets Ete–1, Ete–10, Ote–1, and SOte–1, during northern summer: TOA-all-sky autocorrelation for an observer at conjunction (top), at opposition (middle), and TOA-clear-sky autocorrelation for an observer at opposition (bottom).

ii) The time resolution.– It is important to have a high time resolution to do a good sampling of the periodicity. If the latter is not a multiple of the time resolution, there is a longitudinal angle phase $\Delta\phi$ between the real and the measured period that is cumulative over time, then the longer the time considered, the worser the autocorrelation.

iii) The climatic effects over the signal.– Climate effects have an influence on the autocorrelation function and are also cumulative: as the seasonal flux variation or the random effect of clouds.

In our case we have made the best compromise between these factors. Table 5.5 presents the values of the autocorrelation series of our set of planets for an observer at opposition and an observer at conjunction (in parentheses), for several sub-observer's latitudes at northern summer and Figure 5.17 shows the corresponding

autocorrelation series of the TOA-all-sky emission at conjunction (top row), at opposition (middle row), and of the TOA-clear-sky emission at opposition (bottom row) for several sub-observer's latitudes during three rotational periods of each planet at northern summer. For most observers the period of the planet is well determined within the uncertainty given by the time resolution, with the exception of the polar views.

The common source of rotation in terrestrial planets is the presence of steady high clouds, whereas transient clouds have the opposite effect, usually distorting the periodicity of the planetary signal. In the case of the Earth, the modulation is created by the succession of warm and cold (cloudy) regions of the planet (Chapter 4, Gómez-Leal et al. (2012)). The signal of the slow-Earth is specially marked by the temperature meridional gradient and the temperature contrast between oceans and lands, although most of the time the planet is entirely covered by clouds (Figure 5.7 and Figure 5.8). The oceanic regions are covered with low clouds that are thin to thermal radiation, and high clouds, thick to infrared emission, are placed over the continents. As a result, although the surface temperature is similar, the TOA emission is distinctly different for each type of surface because it comes from different altitudes in the atmosphere, and then the modulation of the signal is very high. The convection clouds disappear during the night, but as they are related to the topography of the planet, the period is still retrieved by slight difference in thermal emission of oceanic and continental regions (in this case continent regions are warmer (see next section, Fig. 5.7) top chart).

On the aquaplanet, high clouds are primarily distributed along the ITCZ, and clouds are rare but quite stable on the snowball planet, because of the cold temperatures. As cloud lifetimes are longer than the rotation period in both planets, the period can be determined despite of having a homogeneous surface.

However, when in the case that the planetary view is uniform and the temperature contrast between clear and cloudy regions is not significant, the period cannot be

estimated. In the case of the Earth, an observer over the Antarctica is not able to determine the period, as the southern hemisphere is mostly covered by oceans and the cold and cloudy antarctic winter does not show temperature variances along the day. This happens also to observers over the poles of the aquaplanet and the snowball planet, particularly in winter over high latitudes, because of the absence of high clouds (Fig. 5.9).

Figure 5.17 shows the autocorrelation series of the four planets during northern summer. Comparing the two bottom charts ("all" and "clear-sky"), we can retrieve the effect of the clouds. The Earth and the aquaplanet does not present relevant differences and the most relevant distortions occur in Ete–10 and SOte–1. In the slow-Earth, convection clouds, attached to humid regions, have also a certain modulation and the signal is less affected, however for polar views (90°N, violet), they mask the diurnal temperature cycle of the surface. In SOte–1, the periodic signal is unmistakably produced by the clouds, the origin of the rotation period comes from the humidity of the ITCZ (clear-sky TOA emission, black line), we also see that the clouds that produce the autocorrelation are more intense during the day at low latitudes.

In summary, if the clouds have longer life-times than the rotation period, they create the periodic signal and the period is easily retrieved from the autocorrelation. On the contrary if the cloud lifetimes are shorter than the rotation period, the periodic signal cannot be calculated from the autocorrelation. In order to retrieved the period, we need a long observation time to have a large number of rotations contained in the signal.

5.5 Longitudinal light curves

After the determination of the rotation period, the observer can built an average rotation light curve in order to identify warm and cold regions on the planet. The average rotation is built by time-folding the signal. In order to avoid the variation

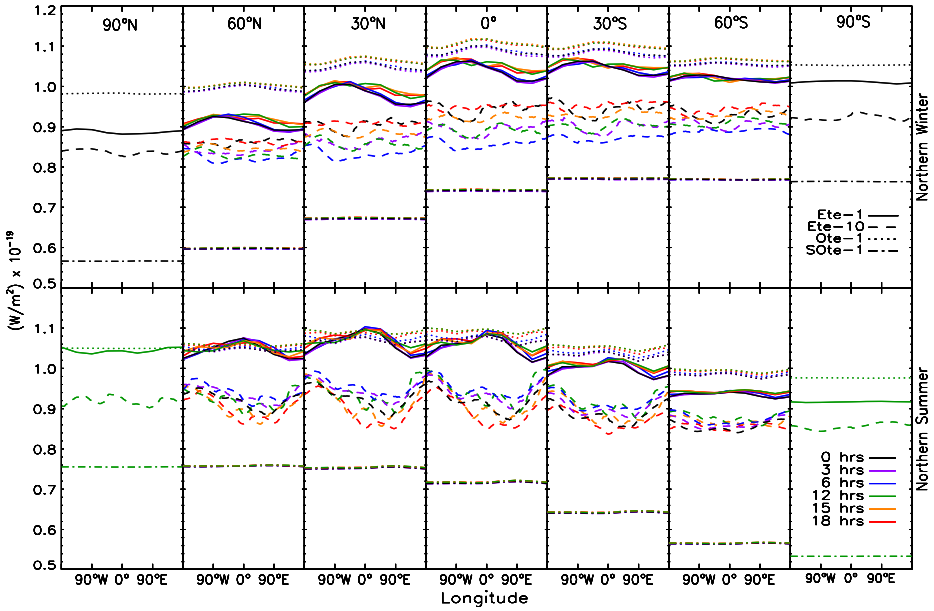

Figure 5.18 Longitudinal light curves: Mean TOA-all sky flux vs longitude, during northern winter (top) and northern summer (bottom) for the latitudes 90°N, 60°N, 30°N, 0°, 30°S, 60°S, and 90°S, colours correspond to local hour at the planetary disk center-meridian towards the observer.

in flux produced by the seasons, and to find a compromise between a good statistics and sampling of the signal, the optimal series length is estimated to be ∼10 days.

Figure 5.18 represents the averaged rotation curve viewed by different observers (sub-observer's latitudes in columns and local hours in colours) for our set of planets during northern winter (top row) and northern summer (bottom row). It is presented as thermal flux in function of the planetary longitude, as it is explained in Section 2.3.2, by this method, we can infer warm and cold regions on the planet. For comparison, the rotational curves of the NASA-SRB Earth are described in Section 4.4. LMDZ results are similar, except for the fact that, although the shape of the graph is the same, the temperature evolution along the day for the maximum (Sahara-Arabian region) and the minima (Indonesia) are not the same, due to the differences in the cloud modeling. However, this fact does not affect the global results

of this study.

There is a diurnal cycle in Ete-10, due to the continental convective clouds that make the planet colder during the evening. These clouds disappear from the view when the Pacific ocean passes through the center meridian, then, as the region is covered with low clouds (Figure 5.7 and Figure 5.8), the global emission is warmer, specially in summer (Table 5.4).

The modulation in Ote–1 is only produced by the regions with a high condensation of clouds. In the snowball planet, the temperature difference between clear and cloudy regions is very low and the effect of clouds is not important. However, the effect of the eccentricity of the orbit is clearly seen, with a warmer summer and a colder winter in the Southern Hemisphere.

5.6 Summary

In this chapter, we have studied the thermal light curves of four Earth-like planets: The Earth; a slow Earth, with a rotation period of 10 days; an aquaplanet with Earth orbital parameters and a snowball version of this aquaplanet. Climate is highly dependent on surface temperature, Bond albedo, rotation rate, cloud covering and continental distribution. Then, we have calculated the global parameters of the atmosphere, discuss the climatic conditions, and study the influence of the physical characteristics of the planet on the signal.

In comparison with Earth's climate, a slow Earth has a colder climate, zonal winds are very slow and the meridional circulation dominates, it also has a diurnal convection cloud formation cycle in the form of huge monsoons and a thick layer of low clouds over the oceans. As a result of a large part of the surface is frozen. Unlike the Earth, there are equatorial superrotating winds in the upper levels of the troposphere.

An aquaplanet analogue has a warmer climate, the greenhouse effect is severe because of the large fraction of high clouds. Surface temperatures of aquaplanets are influenced by the eccentricity of the orbit (the southern summer is warmer because at that moment the planet passes by the periastron).

The snowball climate is cold and dry with very slow winds, a layer of low cloud covers the surface except in summer, when convection clouds are formed.

The time series variability of Earth-like planets is produced by three main factors: the seasonality, by which the energy absorbed (and emitted) changes along the orbit because of the inclination of the rotation axis; the rotation of the planet, as the change in flux is created by the contrast between warm and cold areas of successive planetary views; and the diurnal variability, when the temperature cycle of a particular region produces a change in the emission.

The rotation period of the signal can be retrieved, with a compromise of the length of the time series considered, if cloud lifetimes are longer than the rotation period or if the planet has cloud-convection regions, where clouds are formed constantly. In this case, the regions are characterized for the low brightness temperature from the top of the clouds. The large humidity ratio associated with convection regions is the origin of the periodical signal.

Finally, we have obtain the longitudinal curves of the planets, which allow us to identify warm and cold regions and the influence of the axial tilt (seasons) and eccentricity of the orbit.

Chapter 6

Water Worlds

We present the study of the thermal emission of five aquaplanets. As in the previous chapters, we study the physical characteristics of the planet, their influence on the climate, the global infrared emission, and the shape of the thermal light curve observed at different geometries. Because of the homogeneity of the surface, the variability of the signal is produced by the presence of clouds. We are interested in the influence of clouds on the retrieval of the rotation rate. We have used LMD Global Climate Model data of five aquaplanets with the same atmospheric composition as the Earth and we have modified the rotation rate and the tilt of the rotation axis. Section 6.1 is an introduction to this type of planets; Section 6.2 describes the general characteristics of the climate of aquaplanets and the results of our set of study; in Section 6.3, we compare the infrared light curves of non-synchronous and synchronous aquaplanets; in Section 6.4, we discus the retrieval of the rotational period in planets without continents; Section 6.5 presents the longitudinal curves; and in Section 6.6, we give the conclusions of our study.

6.1 Introduction

Present oceans cover $\sim$ 71% of the Earth surface, but some geological models show that continents could have been mostly immersed at the end of the Archaean eon ($\sim$2.5 Gyrs ago) with only a fractional area of $2-3\%$ of the Earth was emerged land (Flament et al., 2008). It is possible then that at a certain epoch the early Earth had been covered with water except for a little fraction of its surface emerged in the form of small islands (Belousova et al., 2010; Guitreau et al., 2012). Water worlds could be common within the circunstellar Habitable Zone (HZ). For this reason, it is interesting to study this type of planets. The amount of water on a terrestrial planet could vary considerably as it depends on the delivery of water from sources

outside the HZ. Using N-body simulations to reproduce the formation of the inner Solar system, and assuming that the fraction of water is $\sim 10\%$ in the outer main belt, Raymond et al. (2007) found that they typically form an Earth like planet within the HZ with 1-10 times the amount of water on Earth. According to the so-called "Grand Tack" model, the distribution of water in the main belt is tightly associated with the specific formation and orbital evolution of the giant planets of the Solar System (Walsh et al., 2012) and could vary from one planetary system to another. On the Earth, approximately half of the total amount of water constitutes the oceans, and the other half is held within the mantle. This distribution is not fully understood although some hypotheses have been proposed (Kasting & Holm, 1992) and could also be different on another planet. If we assume that this ratio and the bulk composition of the planet (0.1% of H_2O in mass) are constant, the fraction of emerged land would decrease for a more massive planet. Indeed, the mass-radius relationship is given by $R_P/R_\oplus = (M_P/M_\oplus)^{0.274}$ (Sotin et al., 2007), and thus the depth of the ocean would increase as 2.7 km$\times(M_P/M_\oplus)^{-0.274}$. On an Earth replica twice as massive as our planet, the ocean would therefore be 20% deeper while the highest mountain (that scale as gravity^{-1}) would be 20% lower.

However, planets of terrestrial mass may have a very different origin than the Earth and it is expected that some of them may consist in a much larger fraction of water. An ocean planet, as proposed by Kuchner (2003) and Léger et al. (2004), is an Earth-like planet ($\leq 10M_\oplus$) formed of cometary material in the outer cold regions. Afterwards, the body migrates into the Habitable Zone (HZ) where the ices melt into liquid water oceans that cover the surface. The formation of a water-rich planet ending in the HZ can also be triggered by the migration of giant planets (Raymond et al., 2006). Having lower density, the radius of an ocean-planet is larger and its gravity lower than in terrestrial analogues (Sotin et al., 2007; Adams et al., 2008). This property make this type of planets easier to detect by transit missions like CoRoT or Kepler (Selsis et al., 2007) and easier to study by spectrophotometry (JWST).

Planets covered by oceans with any or little emerged lands are thus an expected

Table 6.1. Planetary specifics

	Rotation period (sidereal days)	Obliquity (degrees)	Excentricity	Type of planet
Ete–1[a]	1	23.44	0.0167	Earth-like
Ote–1[a]	1	23.44	0.0167	Aquaplanet
O–1	1	0.00	0.000	Aquaplanet
O–10	10	0.00	0.000	Aquaplanet
Os–1	1	0.00	0.0000	Synchronous aquaplanet
Os–10	10	0.00	0.0000	Synchronous aquaplanet
Os–360	360	0.00	0.0000	Synchronous aquaplanet

[a]Values of Earth (Ete–1) and Ote–1 (Chapter 5) are given for comparison.

result of planet formation and evolution. The Earth itself may have been mostly covered by water during half of its history (although neither the atmosphere nor the oceans had the same characteristics as present Earth). The discovery of extrasolar water worlds would open a new field of comparative planetology. Because of their homogeneity, this type of planets is interesting to study the interaction between the ocean and the atmospheric circulation. In addition, their environmental conditions will be valuable to examine the hydrothermal origin of life (Wächtershäuser, 1988, 1990).

6.2 Planetary characteristics

In addition to the stellar insolation, the energy budget of a planet and its climate depend on many factors, such as the atmospheric composition, surface characteristics, and the circulation of the atmosphere and ocean. On an Earth-like planet, the circulation modulates the temperature by directly transporting energy and setting the distribution of water vapor and clouds.

Table 6.2. Global parameters of radiation

	T_{eff}[a] (K)	A	CRF (W/m^2)	g_N	T_S (K)	∇T_S^{φ} (K)	∇T_S^{ϕ} (K)	$\Delta\varphi_S^{max}$ (°E)	$\Delta\phi_S^{ice}$ (°lat)
Ete–1[b]	255	0.30	-27.2	0.39	288	-	50-80	-	-
Ote–1[b]	258	0.26	-28.7	0.41	294	-	54	-	75
O–1	257	0.27	-27.4	0.39	291	-	74	-	60
O–10	245	0.40	-31.3	0.33	270	-	75	-	45
Os–1	238	0.46	-20.6	0.23	254	22	96	15	50
Os–10	231	0.52	-15.5	0.09	237	65	84	15	60
Os–360	231	0.53	-15.5	0.09	236	66	66	0	60

Note. — Effective temperature T_{eff}, albedo A, cloud radiative forcing CRF, normalized greenhouse parameter g_N and surface temperature T_S (Section 2.2). ∇T_S^{φ} and ∇T_S^{ϕ} are the zonal and meridional temperature gradients. $\Delta\varphi_S^{max}$ is the eastward shift of the surface temperature maximum in degrees. $\Delta\phi_S^{ice}$ is the maximum extension of the ice caps in latitude at the longitude of the substellar point.

[a]The temperature uncertainty is $\pm 5{\cdot}10^{-4}K$, the precisions shown in the table are chosen for simplicity.

[b]Values given for comparison (Chapter 5).

Table 6.3. Characteristics of the Troposphere[a]

	H (km)	N (σ_N) ($10^{-5}s^{-1}$)	L (σ_L) (10^{-3})	l (σ_l) (km)	a (σ_a) (K/km)	Δ_T	Ro_T
O–1	8.513	1329 (7)	247 (7)	1572 (4)	5.2 (0.4)	0.195	0.02
O–10	7.899	1260 (20)	732 (7)	4660 (40)	6.1 (0.6)	0.195	1.91
Os–1	8.001	$10{\cdot}10^2$ ($4{\cdot}10^2$)	$2{\cdot}10^2$ ($1{\cdot}10^2$)	1560 (70)	5 (4)	0.200	0.02
Os–10	7.978	$10{\cdot}10^2$ ($4{\cdot}10^2$)	$8{\cdot}10^2$ ($1{\cdot}10^2$)	5000 (80)	5 (3)	0.122	1.04
Os–360	7.884	$11{\cdot}10^2$ ($5{\cdot}10^2$)	$467{\cdot}10^1$ ($8{\cdot}10^1$)	$297{\cdot}10^2$ ($5{\cdot}10^2$)	5 (4)	0.061	683

Note. — Stratification vs Rotation: H is the scale height, N is the Brunt-Väisälä frequency, L is the normal Rossby deformation radius, l is the Rossby deformation radius, a is the tropospheric lapse rate, Δ_T is the non-dimensional meridional temperature gradient, and Ro_T is the thermal Rossby radius (Section 2.2.3).

[a]The values are restricted to the tropospheric pressure levels of each planet (Figs. 6.5) and 6.6).

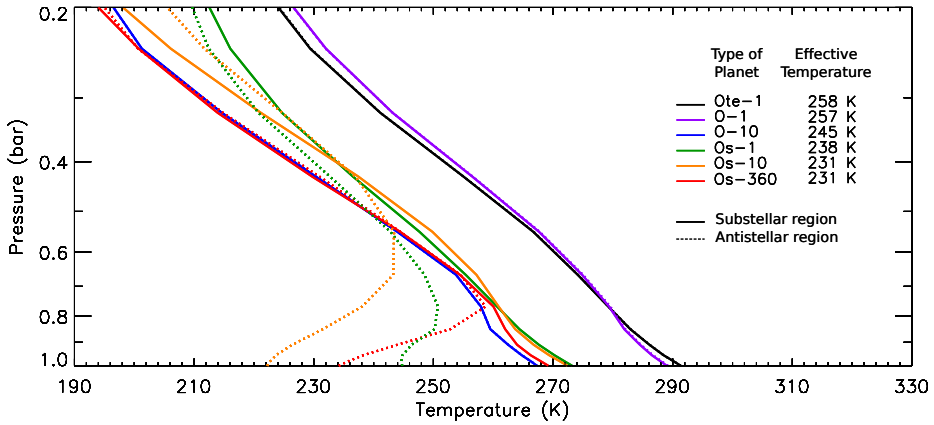

Figure 6.1 Atmospheric profiles for the aquaplanets O–1, O–10, Os–1, Os–10, Os–360 (Table 6.1), at the substellar (solid) and antistellar (dotted) regions.

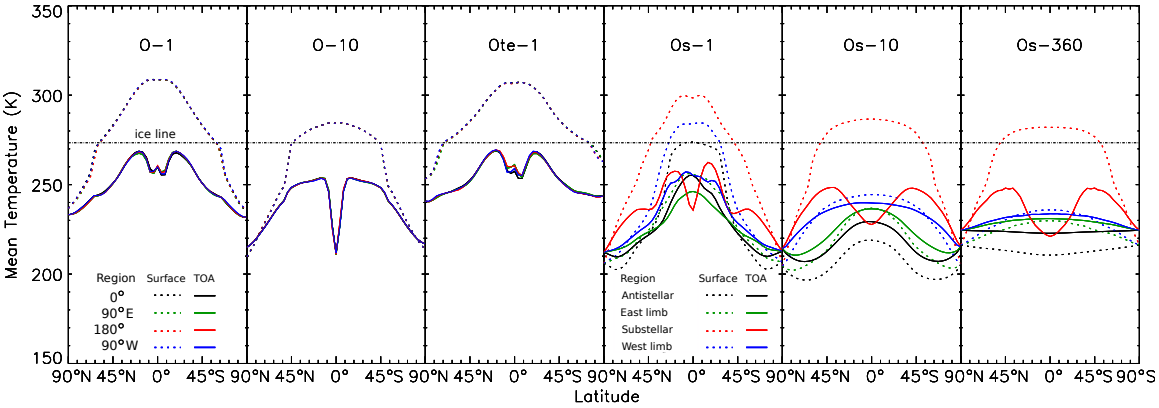

Figure 6.2 Mean surface temperature (dashed) and mean brightness temperature (solid) vs latitude for the planets O–1, O–10, Ote-1, Os–1, Os–10, and Os–360 (Table 6.1). Colours indicate the sectors where the mean temperature is calculated, each sector has 90° in longitude and is centered on 0° (black), 90°E (green), 180° (red), 90°W (blue), respectively, that in the synchronous planets correspond to the antistellar point, the east (morning) limb, the substellar point, and the west (evening) limb.

As we have explained in Chapter 2, clouds are some of the major players in the energy balance of Earth-like planets through two main effects: First, they increase the planetary albedo as they reflect the incoming radiation at short wavelengths, cooling the planet. This effect depends on the cloud optical thickness, as well as the surface albedo[1]. Second, clouds are absorbent in the infrared and for this reason have a direct influence on the greenhouse effect. The most important factor is the difference between the cloud-top temperature – which determines the radiation that will be emitted to space – and the surface temperature, with a large negative difference leading to a warming effect. As the atmospheric temperature generally decreases with height, high clouds have low emission temperatures and a large greenhouse effect – but they can be optically thin in the visible band – while low clouds have a large albedo but a weak greenhouse effect.

The characteristics of the atmospheric circulation of an aquaplanet depend on the rotation speed of the planet. In the tropical zone around the equator, the Coriolis force is weak, and horizontal temperature gradients will be relatively small. The circulation is dominated by thermally direct cells, whose zonally-averaged, meridional components are known on Earth as the Hadley cells. The meridional extent of the Tropics and the Hadley cell are determined by the rotation rate, and to a lesser extent by other parameters such as vertical stability or tropopause height (Hunt, 1979; del Genio & Suozzo, 1987; Frierson et al., 2007). At higher latitudes, the Coriolis force becomes stronger, and the circulation is dominated in both hemispheres by jets in thermal wind balance with larger temperature gradients. Multiple jets can exist in planets with a larger radius.

6.2.1 Non-synchronous aquaplanets

First, in order to study the influence of rotation on aquaplanets, we have built two planets, a case with a rotation rate of one day (O–1), an analogous planet with a

[1]In some specific cases, such as above a fresh snow surface, clouds can in fact lightly decrease the planetary albedo

rotation rate of 10 days (O–10), and each one within a circular orbit of a radius of 1 UA and without any obliquity (Table 6.1). O–1 has an atmospheric profile (Fig. 6.1), a surface temperature and an effective temperature (Table 6.2) comparable to the ones of Earth (Ete–1) and of the analogous aquaplanet Ote–1 from the previous chapter. High-latitudes are however colder in O–1, as the lack of obliquity means that the annual-mean insolation is weaker near the poles. The albedo effect of increased sea ice leads to a lower global-mean temperature, and equatorial temperatures that are very close: surface temperatures are comprised between 235 and 309 K in O–1, compared to 253 and 307 K in Ote–1.

The lower rotation rate of O–10 produces an increase in the width of the Hadley cell, that it is represented by the plateau of highest mean surface temperature and the correspondent brightness temperature in Figure 6.2. The meridional temperature gradients are similar in both types of planets (Table 6.2), but the temperature of the slowly rotating planet is lower almost everywhere; these results contradict former studies using simpler models without complete atmospheric physics (Hunt, 1979; del Genio & Suozzo, 1987). The reason seems to be that the dry subsidence region of the Hadley cells is more extended in O–10, leading to a lower greenhouse effect. This initial impact is then increased by feedbacks, including also a larger sea-ice cover than O–1.

Both planets have a narrow region of reduced brightness temperature near the equator, produced by the ITCZ. This brightness minimum is due to a high concentration of high-top convective clouds, clearly apparent in the maps of Figure 6.8. In the case of O–1, the mean surface temperature has a double-peak structure at both sides of the ITCZ, because of a relative temperature minimum in the ocean surface caused by equatorial upwelling (Schopf, 1980; Bakun, 1990; Codron, 2012), where the interaction of easterly trade winds and the ocean by Ekman transport brings cooler deeper water to the surface at the equator and produces a net transport of water to the poles. Equatorial upwelling is absent in O–10, thus the ITCZ has a single peak at the equator. Low clouds are prevalent over the iced surface (Fig. 6.8).

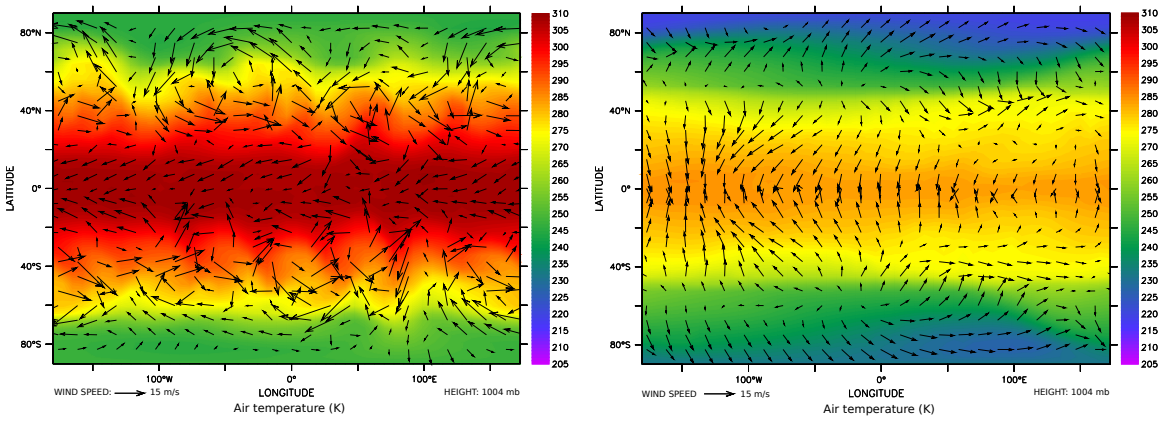

FIGURE 6.3 Mean surface temperature and mean surface wind velocity field in O–1 (left) and O–10 (right).

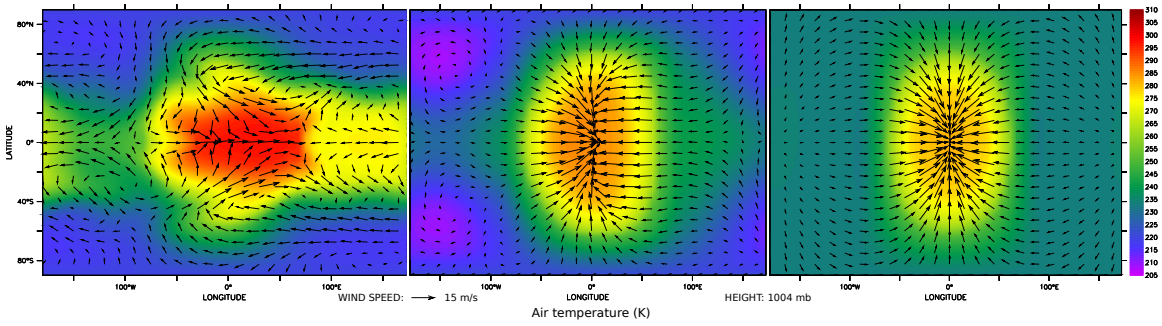

FIGURE 6.4 Mean surface temperature and mean surface wind velocity field for Os–1 (left), Os–10 (center), and Os–360 (right).

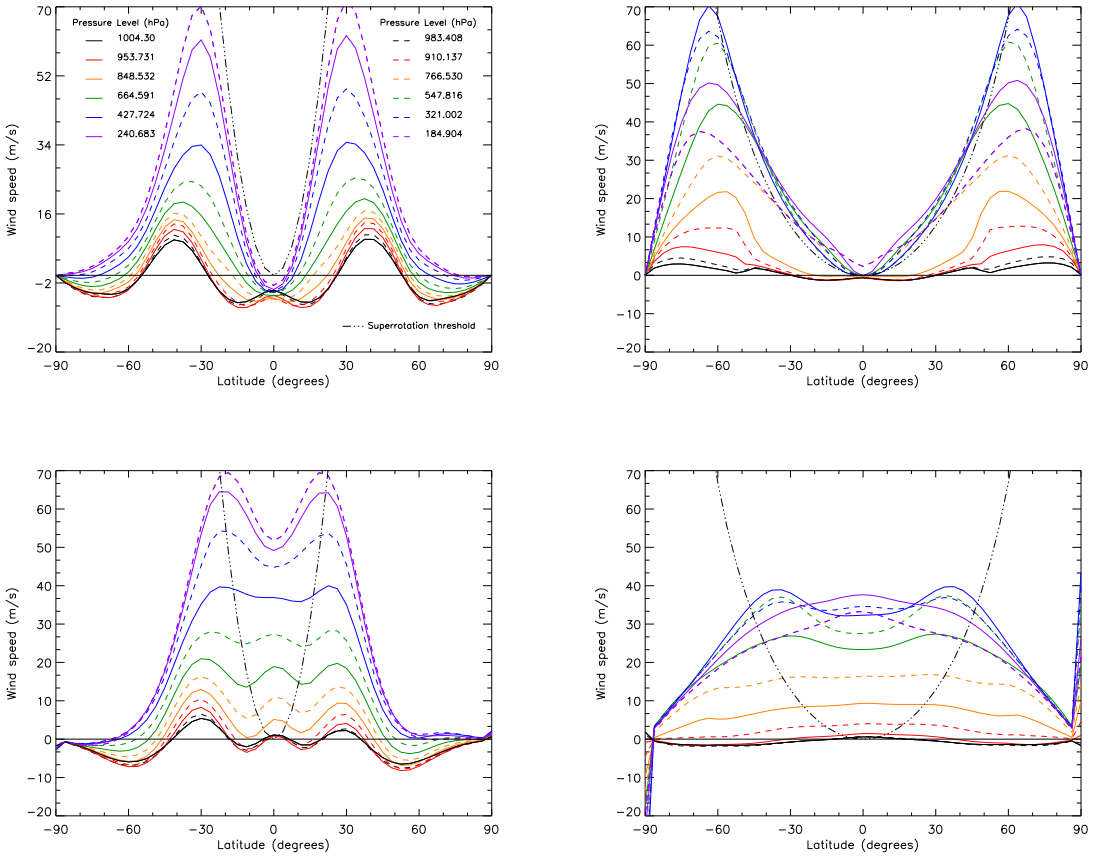

Figure 6.5 Mean zonal wind for O–1 (top-left), O–10 (top-right), Os–1 (bottom-left), Os–10 (bottom-right).

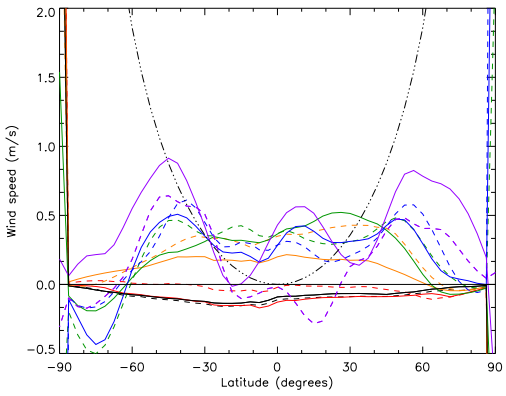

Figure 6.6 Mean zonal wind for Os–360.

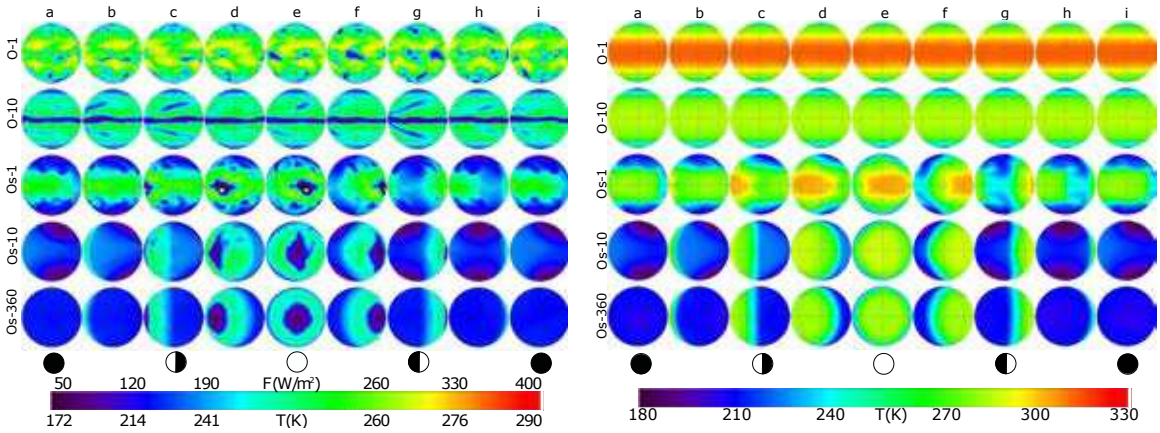

FIGURE 6.7 TOA-all-sky flux (left, scaled in flux and brightness temperature) and surface temperature (right) towards an observer at opposition during one rotation (a-i) for the planets O–1, O–10, Os–1, Os–10, and Os–360. The circles represent the planetary phases of the tidally-locked planets for an observer at the equator.

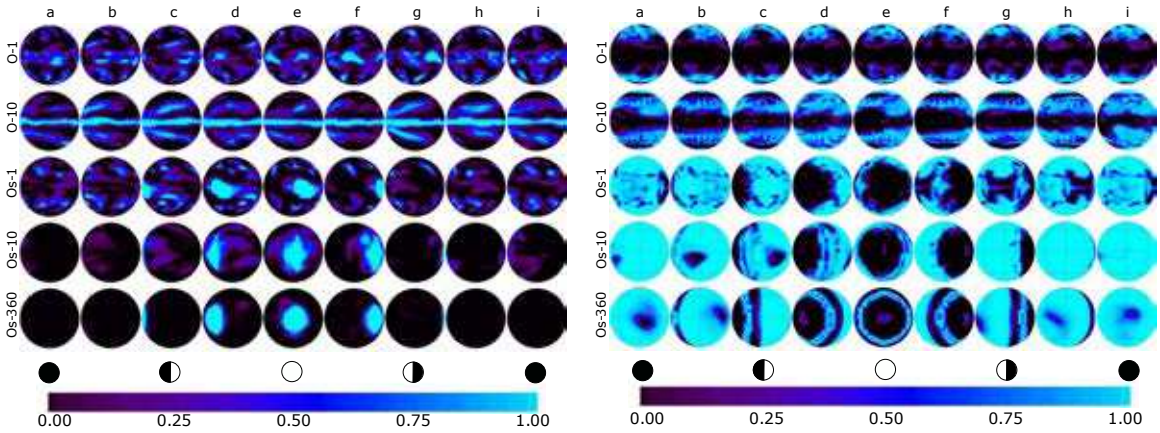

FIGURE 6.8 High cloud fraction (left) and low cloud fraction (right) towards an observer at opposition during one rotation (a-i) for the planets O–1, O–10, Os–1, Os–10, and Os–360. The circles represent the planetary phases of the tidally-locked planets for an observer at the equator.

The day/night temperature contrast is negligible, as can be seen in Figure 6.7 and in Figure 6.2, where the curves are almost coincidental for every point of view. This is due to the high thermal inertia of the surface, whether the 50-m ocean mixed layer or the sea ice layer (as both the thermal inertia of sea-ice and the diurnal cycle of absorbed shortwave radiation are weak).

Figure 6.3 shows the annual mean surface temperature and wind field for O–1 (left) and O–10 (right). The equatorial zonal wind and the instability regions ($\sim$40° latitude) in O–1 are clearly seen, in O–10 the zonal wind is weak and there is a region of convergence in the form of a "chevron"[2]. The winds are predominantly meridional near the equator, where the Coriolis force is minimum, and zonal near the poles, the chevron is orientated south-west to north-east in the Northern Hemisphere and south-east to north-west in the Southern Hemisphere. As in any region of convergence, convection clouds are formed, giving the characteristic pattern of Figure 6.7. Figure 6.5 show that the mean zonal wind speed per latitude and the superrotation limit (dot-dash line). O–10 shows equatorial superrotation in the upper troposphere, it extends to a latitude range of 40° at $\sim$767 hPa, to a 60° at $\sim$185 hPa. The "chevron" cloud opens at high latitudes because the superrotation wind speed increases with latitude. As in the case of Ete–10 (Figure 5.14), the superrotation is faint, however wind speeds are higher in aquaplanet analogues than in planets with continents because the friction of the wind with water is lower than the friction with land.

6.2.2 Synchronous aquaplanets

The atmospheric circulation of tidally-locked planets is rather symmetric respect to the substellar point, because its permanent position. In order to separate insolation regimes, in Figure 6.2, we have pictured the mean surface temperature along with

[2]A similar pattern has been observed in slow planets with superrotation winds as Titan and Venus, but curiously, the orientation of the chevron is the opposite, with the tip pointing eastwards. The origin of this arrow is the combination of Rossby and Kelvin waves, (Tokano, 2011; Showman & Polvani, 2011)

the brightness temperature within different sectors of the planet, each covering 90° in latitude: q1 is centered at 0° longitude in the center of the nightside, q3 at the substellar point, q2 at 90°W and q4 at 90°E at terminators.

In tidally-locked planets, the ITCZ is replaced by a region of ascending air around the substellar point, largely covered by high clouds that result in a pronounced minimum in brightness temperature as it is also visible on the maps of Figure 6.7 and Figure 6.8. Then the circulation transports heat away from the permanent dayside, preventing an atmospheric collapse on the nightside. This transport is more efficient above the surface boundary layer, leading to temperature inversion on the nightside (Figure 6.1), which helps the formation of low cloud decks (Figure 6.8).

At the same time, the high albedos of the low clouds and the ice, which cover a large part of the surface away from the substellar point, strengthen this effect (Figure 6.2), and mean surface temperatures on the planet are between 300 and 210 K. Merlis & Schneider (2010), with a model with simplified physics, obtains warmer temperatures (300 K- 250 K), possibly because of the weak greenhouse effect or the albedo of the high clouds in the substellar region. The ice-albedo feedback is likely to be weak however, as the ice-covered regions are the ones receiving little insolation (Joshi et al., 1997). The heat transport by the ocean is limited to the ice-free region.

The actual dynamics of the atmosphere depends on the rotation rate. In the slowly rotating planet (Os–360), the circulation is symmetric with respect to the substellar point (del Genio & Zhou, 1996). In the rapidly rotating planet (Os–1), the zonal asymmetry in insolation creates stationary Rossby and Kelvin waves that carry momentum towards the equator and generate the equatorial superrotation (Merlis & Schneider, 2010; Showman & Polvani, 2011). The tropical jet is strong enough to shift eastward the position of the minimum and maximum of temperature by ∼90 degrees and ∼20 degrees respectively. The rapid rotation also limits poleward heat transport by a thermally direct cell, leading to a larger meridional temperature gradient (see

Table 6.2). The intermediate rotation rate (Os–10) resembles the slow

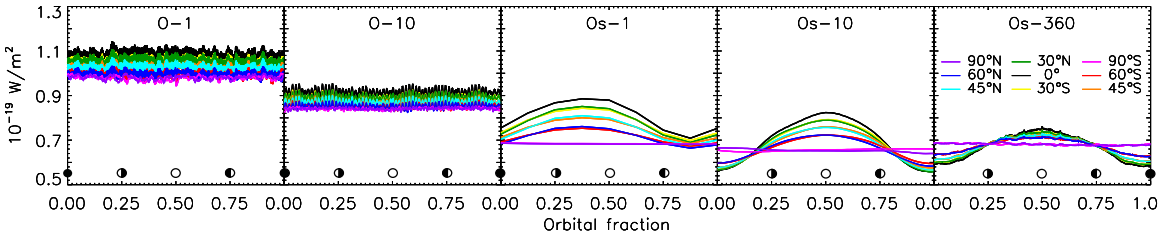

Figure 6.9 TOA-all-sky flux orbital series for the terrestrial planets O–1, O–10, Os–1, Os–10, and Os–360. The circles represent the planetary phases of for an observer at the equator.

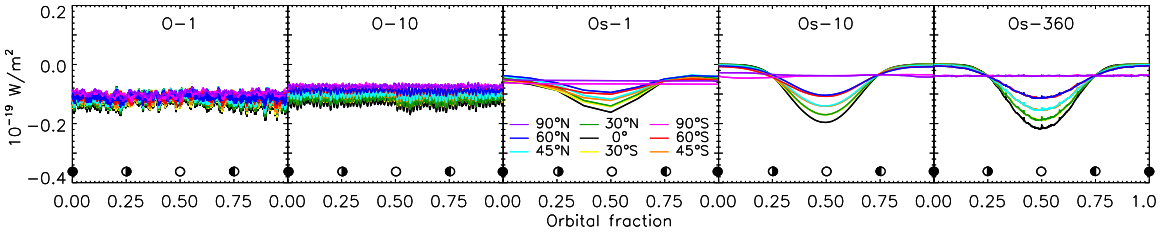

Figure 6.10 Cloud Radiative Forcing corresponding the orbital series for the terrestrial planets O–1, O–10, Os–1, Os–10, and Os–360. The circles represent the planetary phases of for an observer at the equator.

case, with similar circulation patterns, albedos, greenhouse parameters, and surface and effective temperatures. But the rotation of Os–10 still leads to anisotropy, shown as the temperature minimum at $\sim 60°$ latitude in both hemispheres (Figure 6.2, Figure 6.4 and Figure 6.7). It is remarkable that especially for Os–1 and also for Os–10, the minimum temperatures are not found near the antistellar point but near the poles. Figure 6.4, which represents the mean temperatures and the wind velocity fields at the surface of the set of synchronous planets, shows that the winds always converge in the warmest region of the planet.

In Figure 6.5 and Figure 6.6 we see that there are superrotating winds in the three

Table 6.4. Time series variability

	Variability	Orbital phase	Latitude								
			90	60	45	30	0	-30	-45	-60	-90
Ete–1[a]	Rotational	[4/12,5/12]	3	4(5)	5(6)	5(7)	4(6)	4(5)	4(5)	3(4)	2
	Orbital	[0-1]	19	17(15)	14(12)	11(9)	5(3)	4(6)	6(8)	8(9)	10
Ote–1[a]	Rotational	[4/12,5/12]	2	4(4)	5(5)	6(6)	6(7)	6(7)	5(6)	4(5)	2
	Orbital	[0-1]	8	8(6)	8(5)	7(3)	5(4)	5(7)	6(8)	8(9)	9
O–1	Rotational	[0,1/12]	2	4	5	6	6	6	5	4	2
	Orbital	[0-1]	2	3	3	3	3	3	3	3	2
O–10	Rotational	[0,1/12]	2	3	4	5	5	5	4	3	2
	Orbital	[0-1]	1	2	2	2	2	2	2	2	1
Os–1	Orbital	[0-1]	2	12	16	18	19	17	14	11	2
Os–10	Orbital	[0-1]	3	15	21	25	28	25	21	16	3
Os–360	Orbital	[0-1]	2	13	17	20	24	20	17	12	2

Note. — Time series variabiity for aquaplanets O–1, O–10, Os–1, Os–10, Os–360. Values as percentage over the mean.

[a]Values given for comparison (Chapter 5).

planets. The superrotation band extends to ∼30° in latitude in Os–1, that shows winds speeds values similar to the Earth, with a maximum speed of ∼70 m/s. Os–10 has a superrotation winds within a band that extends to ∼45°, the with maximum speed (∼40 m/s) is lower to to the colder temperatures and the slower rotation of the planet. On the contrary, the state of Os–360 is stable and the net circulation is negligible with speeds < 1 m/s. Figure 6.7 and Figure 6.8 shows the symmetry respect to the substellar point as well as the surface of ice and water, the cloud covering, and the heat transport along of the planet for an observer at opposition at the equatorial plane.

6.3 Time series analysis

Figure 6.9 illustrates the orbital thermal light curves of the planets at a distance of 10 pc, for nine different observer's inclinations. As it was previously explained, the

TOA emission is perturbed by the presence of high clouds. We have also calculated the correspondent CRF, at each point of the series in order to quantify the relevance of this absorption on the integrated signal (Figure 6.10).

6.3.1 Non-synchronous aquaplanets

The planetary thermal emission is essentially dependent on insolation, for this reason the light curves of O–1 and O–10 depend on the observers position. Rotation rate and the high thermal inertia of water prevent from having significant differences between day and night, and in the absence of seasons, the variability is strictly produced by the presence of high clouds. In non-synchronous aquaplanets, the production of this type of clouds is determined by the atmospheric circulation and not by illumination, as it is the case of terrestrial planets (Chapter 5). Low clouds are more abundant near the poles over the permanent ice caps (Figure 6.8), whereas at low latitudes, warm convective currents rise the clouds to higher levels of the troposphere. For this reason high clouds are mainly placed along the ITCZ.

As expected, in O–1, the rotational variability of the planet (Table 6.4) is comparable to an aquaplanet with the axial tilt of the Earth (Ete–1), whereas it has a little orbital variability, as it is just produced by the fluctuation of clouds.

In O–10, the atmosphere is colder and less turbulent than in O–1 and the clouds are evenly distributed along the ITCZ. High clouds also appear along the mid-latitude convergent region producing a “chevron” cloud pattern (Merlis & Schneider, 2010; Showman & Polvani, 2011). The cyclical appearance of this pattern causes an additional frequency modulation on the signal of the planet.

6.3.2 Synchronous aquaplanets

In planets with circular orbits, the thermal light curve of tidally locked planets gives an important information about the distribution of the brightness temperature on the planet. The maximum and the minimum of the curve correspond respectively

to the permanent day and night sides of the planet. However, because of the atmospheric circulation, these features can be shifted from the substellar and the antistellar points by several degrees (e.g., Fortney et al., 2006; Knutson et al., 2007), a fact that is useful to distinguish between atmospheric and airless planets (Seager & Deming, 2009).

The atmosphere has a large CRF near the substellar point, where the tropospheric wind converges forming a huge condensation cloud (Figure 6.4 and Figure 6.8). The nightside can be colder and drier than the poles. However, in Os–1, the superrotation jet warms the nightside, displacing the minimum of temperature to lower latitudes ($\sim$60°). Then, although and the polar views have the lowest brightness temperature, the minimum value of the orbital series belongs to views at $\sim$60° in latitude (Figure 6.9), because of the circulation and the thermal inertia of the atmosphere. The maximum is shifted 15°E (Table 6.2 and Figure 6.9). In the case of Os–10, this shift is barely appreciated in the light curve because, although slower planets have lower temperatures, the atmosphere is less turbulent and as a consequence the CRF is larger at the substellar point (Fig. 6.7 and Fig. 6.10), absorbing the thermal emission from below. This extreme difference between the dayside and the nightside is represented by the orbital variability (Table 6.4).

It is interesting to note that in Os–1, the variability at the equator is comparable to the seasonal change at Earth's north polar view. For tidally-locked planets with slower rotation rates the variability increases, but it is not directly proportional as it also depends on the climate, specially on the extension of the iced surface and the magnitude of the convective clouds over the warmest point of the planet.

6.3.3 Parameters retrieved from the series

As we have shown in Section 2.2, the planetary effective temperature and albedo can be retrieved from the orbital light curves. Table 6.5 shows the results for nine different positions of the observer. High latitudes, being colder and more abundant

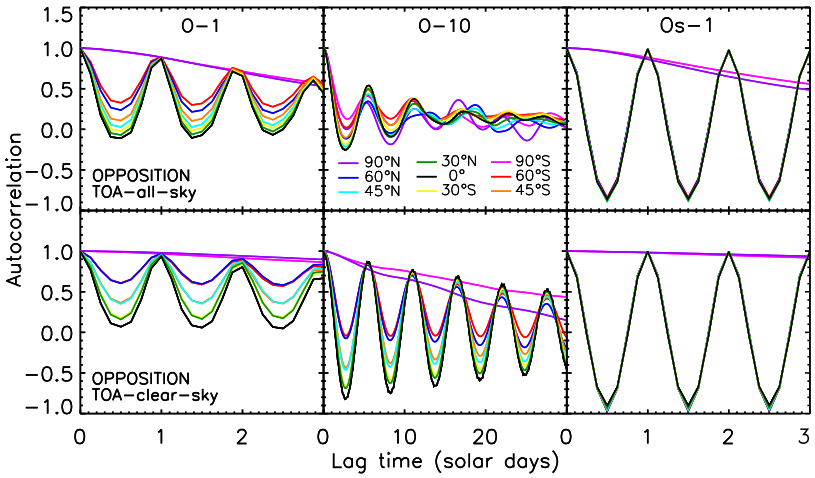

Figure 6.11 TOA-all-sky autocorrelation series for an observer at opposition for the planets O–1, O–10, and Os–1.

in low clouds, present higher albedos and lower effective temperatures, whereas observers over low latitudes, where the insolation is higher, retrieve higher effective temperatures and lower albedos. For every planet, latitudes $\sim 30^{\circ}$ give results near to the global value.

6.4 Periodicities

We have used the autocorrelation analysis of the time series to obtain the rotation period of the five planets (Section 2.3). As the rotation period of tidally-locked planets can be directly retrieved from their thermal orbital light curve, in this section, we only present the results for O–1 and O–10 (Figure 6.10 and Table 6.5).

Figure 6.11 give the autocorrelation for the TOA-all-sky emission (top) and the TOA-clear-sky emission (bottom). The latter also contains the information of humidity, without the cloud absorption, for this matter, the period obtained is given by the distribution of the humidity related to convective regions (1 day for O–1 and ∼6 days for O–10). The TOA-all-sky emission shows the effect of the cloud absorption.

Table 6.5. Observed parameters[a]

		Global	Latitude								
		Value	90	60	45	30	0	-30	-45	-60	-90
O–1	T_{eff} (K)	257	253	254	256	257	259	257	256	254	253
	Albedo	0.27	0.32	0.31	0.29	0.27	0.25	0.27	0.29	0.31	0.32
	τ(days)	0.99	-	1.00	1.00	1.00	1.00	1.00	1.00	1.00	-
O–10	T_{eff} (K)	245	243	243	244	245	246	245	244	243	243
	Albedo	0.40	0.41	0.42	0.41	0.40	0.39	0.40	0.41	0.42	0.41
	τ(days)	9.97	-	10.75	6.25	6.25	6.25	6.25	6.25	10.75	-
Os–1	T_{eff} (K)	238	231	234	237	239	241	239	237	234	232
	Albedo	0.46	0.52	0.50	0.48	0.46	0.44	0.45	0.48	0.50	0.52
	τ(days)	1.00	-	1.00	1.00	1.00	1.00	1.00	1.00	1.00	-
Os–10	T_{eff} (K)	231	229	229	230	231	232	231	230	230	229
	Albedo	0.52	0.54	0.54	0.53	0.52	0.51	0.52	0.53	0.54	0.54
	τ(days)	10.00	-	10.00	10.00	10.00	10.00	10.00	10.00	10.00	-
Os–360	T_{eff} (K)	231	231	231	231	230	230	230	231	231	231
	Albedo	0.53	0.52	0.53	0.53	0.53	0.53	0.53	0.53	0.53	0.53
	τ(days)	360.0	-	360.0	360.0	360.0	360.0	360.0	360.0	360.0	-

[a]Observed parameters from the time series: effective temperature T_{eff}, albedo A and rotational period τ (Chapter 2) for the planets Ete–1, Ete–10, Ote–1, and SOte–1 at opposition and at conjunction (in parentheses) for several sub-observer's point latitudes. Values are calculated as the percentage over the mean value.

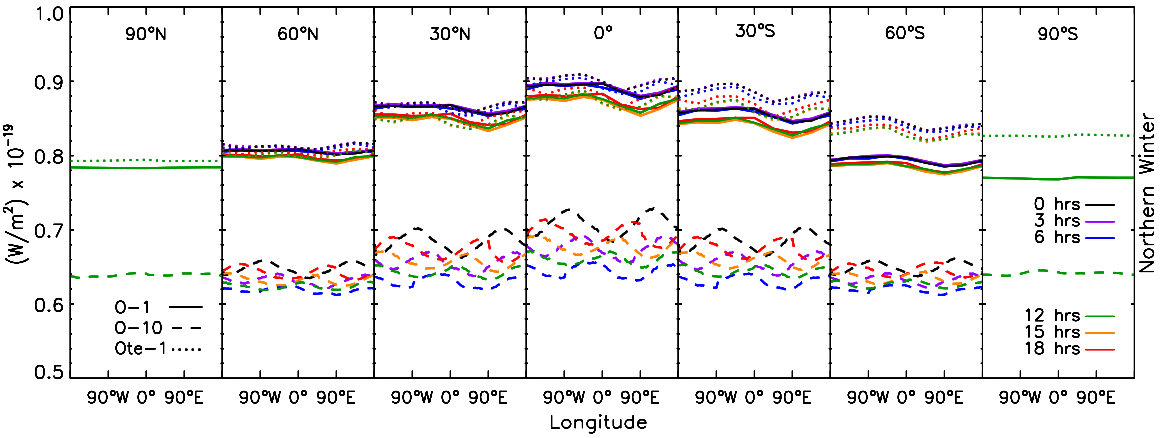

Figure 6.12 Rotational series for the planets O–1 and O–10. Ote–1 rotational series during northern winter is given for comparison. Colors represent the local hour at the planetary disk center meridian.

Table 6.5 shows a dispersion in the rotation rates of O–10 with latitude, due to the superrotation of the atmosphere.

To set an example, due to the day/night contrast and the steady state of the weather patterns, the autocorrelation of Os–1 clearly shows a rotational period of 1 day for every observer (except for polar ones where the planetary view does not change). However, in the case of non-synchronous aquaplanets with circular orbits, the variability of the signal comes only from the presence of clouds. When the rotation period is longer than the cloud lifetimes, as in O–1, the autocorrelation is reinforced. On the contrary when the cloud lifetimes are shorter than the planetary rotation, as in O–10 due to the superrotation of the atmosphere, the regions are periodical but the clouds change after one rotation of the planet, and then the autocorrelation obtained by a distant observer, becomes worser with time.

6.5 Average rotation light curves

As in Chapter 4, we can built an average daily signal by time-folding the series with the value of the rotation period obtained by autocorrelation. This method

minimizes the fluctuations of the signal and the steady features stand out. It is useful to compare Figure 6.12 with Figure 6.7 and Figure 6.8. Whereas Figure 6.7 and Figure 6.8 represent the planetary disk seen by an equatorial observer at opposition during one rotation, Figure 6.12 shows the rotational average series for O–1, O–10 and Ote–1 (Chapter 5). Each graph of Figure 6.12 is formed by the views of the planet at the same local hour (each view of Figure 6.7 correspond to the graphs at 0 hrs). Following this description, these type of curves are observed by a unique observer only in the case of planets with circular orbits and without axial tilt, as it are the cases of O–1 and O–10. In the absence of seasons, the planet receives the same energy at every point of the orbit and the short rotation period allow the observer to built the graphs of Figure 6.12.

As expected, O–1 does not present significant variabilities within one period and resembles the average rotation curve of Ote–1, with the exception that the latter, having an axil tilt, has a change in the mean temperature level produced by the seasons and the southern hemisphere is warmer due to the eccentricity of the orbit.

Taking in account the superrotation of the atmosphere, the clouds of O–10 exhibit a diurnal cycle. The planet gets warmer during the day, the absorption of the convective clouds becomes stronger, the "chevron" pattern appears at both the substellar and the antistellar point at afternoon (15 hr, local), moves towards the east (as it rotates faster than the solid body). It grows being maximal at midnight (0 hr, local). Then, it rains during the night then the cycle starts again at 15 hr.

6.6 Summary

In this chapter, we have studied the thermal emission of five aquaplanets with circular orbits and without axial tilt (without seasons): O–1 and O–10 have a rotation rate of 1 and 10 days, respectively; and three synchronous aquaplanets Os–1, Os–10, Os–360 with rotation rates of 1, 10 and 360 days, where the stellar constant is modified according to the orbital distance.

Aquaplanets analogues are warmer than terrestrial planets, with an ITCZ with a high concentration of convective clouds because the large specific humidity. An aquaplanet with the same orbital parameters than the Earth has an effective temperature of 258 K, an aquaplanet analogue with a circular orbit and without axial tilt, has an effective temperature of 257 K. Synchronous aquaplanets however have low surface temperatures and the main part of the surface is frozen except for the antistellar region, an Earth analogue with a rotation rate of 1 day, has an effective temperature of 238 K. The warmest point is usually shifted by the circulation of the planet and being a convergence region, steady convection clouds cover the area, which has a slight effect over the signal by decreasing the TOA-emission at this point.

Because of the low thermal inertia of water, the cloud absorption is the only source of flux variability in the signal. Thus, the period is retrieved by autocorrelation if the cloud lifetimes are longer than the period of the planet or if the clouds are linked to convergence regions. Thus, the period is retrieved in O–1 because the rotation rate is shorter than the clouds lifetimes. O–10 has a convergence region in the form of a "chevron" pattern, however the region is an atmospheric phenomenon and it is not linked to surface steady features. The period obtained is shorter that the period of rotation of the planetary surface, because the equatorial superrotating winds in the upper troposphere drive the clouds of the "chevron" pattern. The "chevron" cloud opens at high latitudes because the superrotation wind speed increases with latitude. The movement of the "chevron" pattern is shown in longitudinal light curves. The period of tidally looked planets is retrieved because the convergence regions are tied to the surface temperature maximum.

PART IV.

PERSPECTIVES

Chapter 7

Spectral variability of Earth-like planets

A further step is to use narrow band data to build the spectral signal of Earth-like planets. By the comparison with spectra of terrestrial planets, we can infer the physical conditions of the atmosphere, the state and abundances of the main atmospheric species, as well as the global parameters of the planetary climate. The study of narrow-band light curves will also give an important information about the dynamics and the evolution of the most relevant compounds. By the average of the signal, we can also build longitudinal light curves and study their distribution on the planet. We have used a new generic version of the LMD Global Climate Model to build the spectral light curves of the Earth-like planets studied in Chapter 5: the Earth, the Earth with a rotation rate of 10 days (Ete–10), the aquaplanet Ote–1 and the snowball aquaplanet SOte–1.

7.1 Detection of Earth-like planets

The Earth has a brightness temperature of $\sim$255 K, and the correspondent blackbody emission has a peak at $\sim$11 μm. Then, the thermal infrared (5-20 μm) is the most favorable spectral range to detect Earth-like planets. The orbital parameters can be detected by radial velocity using high-resolution spectrometers. For an Earth analogue at a distance of 1 UA from a solar-type star, the flux contrast factor between the star and the planet F_*/F_{pl} is $\simeq 10^6$, 1000 times larger than in the visible range, however in order to obtain an angular distance above the difraction limit $\lambda/D \sim$ 100 mas, a diameter D of 40 m for ground-telescopesis required (**?**). The spectral features of H_2O,CO_2, and O_3 are detectable, however CH_4 is just detectable in Early-Earth atmospheres where CH_4 is predominant (Table 7.1). In the case of rocky

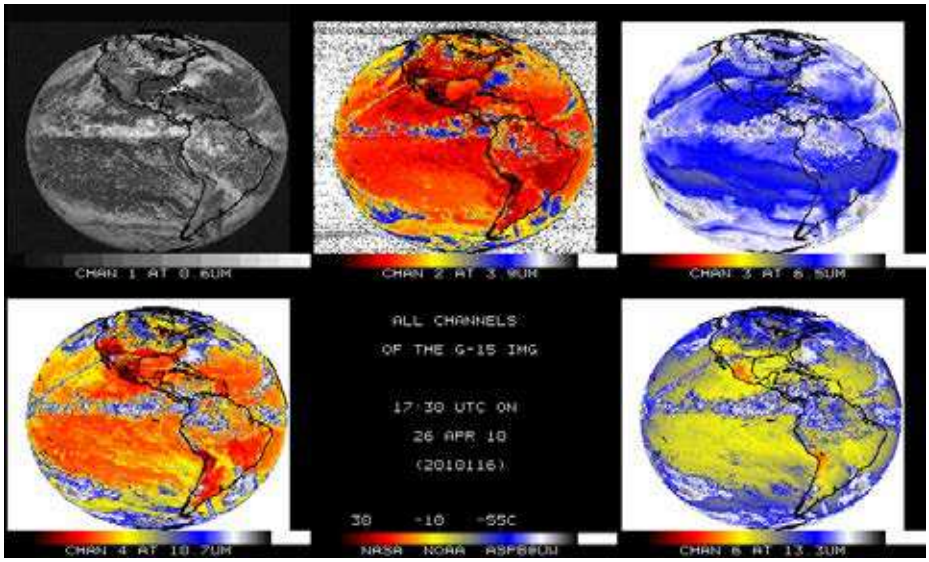

Figure 7.1 NOAA newest Geostationary Operational Environmental Satellite (GOES-15) took its first imager full-disk infrared image of the Earth on April 26 starting at 17.30 UT. Each of the five imager spectral bands are shown. There is one visible band and four infrared bands (shortwave window, water vapor, longwave window and a CO_2 sensitive band). Credit: NASA-NOAA-SSEC.

planets around cold dwarf stars of masses between 0.1-0.2 M $_\odot$ the detection from the ground is possible by 4-8 m class telescopes for planets at a maximum distance of $\simeq$50 pc, with the use of a telescope of 40 m as E-ELT (Martín & Guenther, 2006) allows to acheive distances up to $\simeq$200 pc (e.g., Oliva & Origlia, 2008; Pallé et al., 2011). Furthermore, we can increase the S/N ratio, using instruments like HIRES and METIS on grounds-based telescopes like E-ELT, which will open the door to a new range of measurements:

i) High-resolution spectra.– Planetary spectra can be used to probe into the atmosphere of the planet by identifying the optical depths as they depend directly on wavelength. Features on the atmosphere can be then separated with a resolving power of R$\sim$300, and used to recover the abundances, state, distribution and dynamics of atmospheric species.

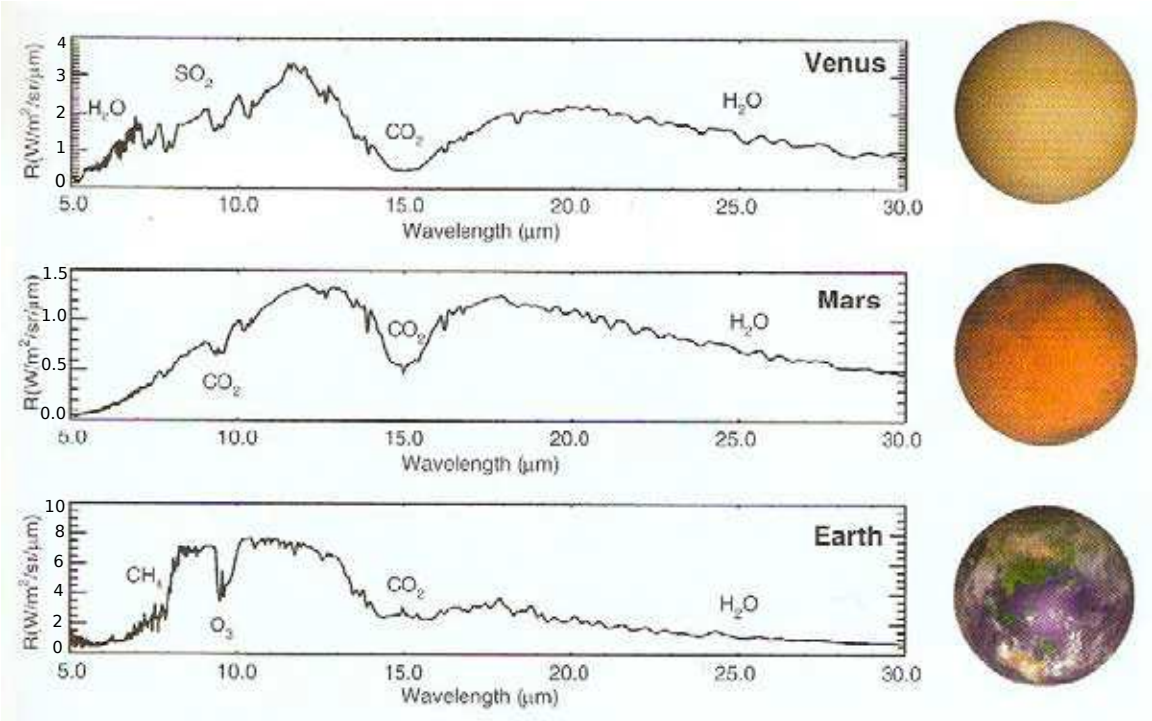

Figure 7.2 Spectral radiance of Venus, Mars and the Earth. (From Vázquez et al. 2010).

ii) Rotation rate and winds.– Orbital velocity maps (time vs. orbital velocity) can be used to measure the zonal winds and the rotation rate of the planet. The velocity deviation is clearly shown as a line broadening (Snellen et al., 2010).

iii) Longitudinal spectral variations.– We can build averaged rotational light curves as a function of the planetary longitude (Section 2.3.2, Figure 5.18 and Figure 6.12) to illustrate the distribution and the dynamics of atmospheric compounds.

Future space telescope missions will use the transit method on bright stars to detect Earth-like planets: PLATO (Catala & PLATO Consortium, 2008; Rauer & Catala, 2011), an ESA mission that is previewed to be launched in 2017-2018, will

Table 7.1. Detection of atmospheric spectral features

Gas	Terrestrial abundance	Spectral feature (μm)	Resolution	Detection threshold
H_2O	8000 ppm	19.6	3.3	1 ppm
CO_2	355 ppm	15	4	1 ppm
O_3	6 ppm	9.6	17	1 ppm
CH_4	2 ppm	8	6	10 ppm
NO_2	0.1-1 ppb	6.3	30	100 ppb
NH_3	0.01 ppb	11	10	10 ppm

Note. — Thermal IR spectral features of the main atmospheric gases on Earth-like planets. The detection threshold is calculated assuming a spectral resolution of 20 and a S/N of 10. From Ollivier et al. (2008); Des Marais et al. (2002) and Selsis et al. (2007).

search transits around stars of 8-11 magnitudes; TESS (e.g., Ricker et al., 2009) is a NASA mission for stars fainter than 12 magnitudes and it will be operative in 2017. EChO (e.g., Tinetti et al., 2012) is the first space mission designed to study exoplanet atmospheres and it will provide high-resolution multiwavelength spectroscopic observations in the infrared range (0.4-11) μm with a contrast ratio $F_*/F_{pl} \sim 10^5$.

A solution to improve the observations without building large telescopes is to use the nulling interferometry technique (Bracewell, 1978), either by a structurally connected interferometer or by a flagship mission, with a 2 m diameter collectors will be capable of detecting more than 100 Earth size planets around nearby stars. However space projects as SIM (e.g., Tanner et al., 2006; Catanzarite et al., 2006; Tanner et al., 2010), DARWIN (e.g., Ollivier et al., 1999, 2001; Cockell et al., 2009) and TPF-I (e.g., Kaltenegger & Fridlund, 2006; Gappinger et al., 2007) have been cancelled.

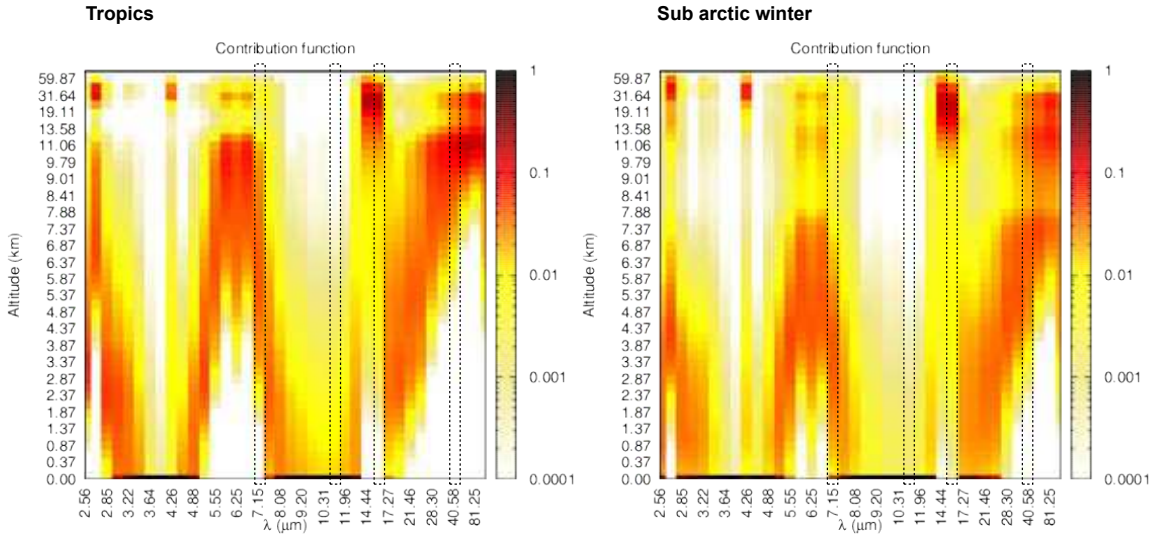

Figure 7.3 Contribution functions for the tropics (left) and the subartic winter (right). The rectangles show the layers that contribute to the formation of the bands used in Figs. 7.4–7.7.

7.2 Climate Model

The generic model was developed at the Laboratoire de Météorlogie Dynamique (LMD) to explore a broad range of conditions in terms of temperature, pressure, atmospheric composition. Its aim is the study early climates (Forget et al., 2013; Wordsworth et al., 2013) and exoplanet atmospheres (Wordsworth et al., 2011; Selsis et al., 2011; Leconte et al., 2013) and to produce time-dependent maps of narrow band fluxes to generate synthetic observables. To do that, most of the empirical parameterizations (for instance to model the condensation and precipitation) or the detailed properties (like the precise albedos and emissivities associated with the different types of soils, vegetations, ice/snow layers) are no longer used. They are replaced by simplified, but more generic physical laws controlled by a few global parameters (like the radius of the ice/water particles, the soil thermal inertia,

emissivity).

This model was applied to the case of present Earth to test its ability to catch the main characteristics of its climate and the associated observables. Although the general properties of Earth climate are reproduced, the simulations produced with this model slightly depart from those obtained with the Earth LMDZ code. In particular the equilibrium and mean surface temperature are lower than that of Earth (or simulated with the Earth LMDZ GCM). This is mainly due to the fact that the radiative effect of ozone is not included (it would require to compute grids of high-resolution absorption coefficients with an additional dimension), which results in a lower forcing. The simplified properties of clouds also yield a lower forcing due to a slightly higher albedo.

We are currently working with recent generic model simulations for the Earth, the aquaplanet Ote–1, and an Earth with a 10 days rotation period (Chapter 5). In this section we present our preliminary results for the mid-infrared spectra and time series obtained for these cases. The analysis of these synthetic observables (from Figure 7.4 to Figure 7.7) will be done after this thesis. However, we can study some main features from the spectral light curves of Figure 7.4 and Figure 7.5. Relating the global brightness temperature of each band to the atmospheric profile, we can identify some atmospheric compounds correspondent to certain bands (named by their center wavelength): water vapor absorption in the low-medium-level of the troposphere (7.14 μm); "atmospheric window", temperature of the low-cloud tops and the surface (11.02 μm), water vapor at the upper levels of the troposphere (40.00 μm), and carbon dioxide at the stratosphere (15.58 μm), the height levels vary in the snowball planet because of the lower lapse rate (Figure 5.11). The curves start at the spring equinox, then for an observer at the northern hemisphere (blue, green) the temperature rises at the surface (11.02 μm) during spring and decreases during autumn. Water vapor bands (7.14 μm, 40.00 μm) have a small seasonal variation because of the accumulation of latent heat associated with evaporation of water at the surface and condensation of water vapor in the troposphere.

7.3 Summary

The use of LMDZ generic GCM spectral data gives the opportunity to reproduce Earth-like planet conditions and simulate the planetary signal detected by a distant observer. By the comparison of the signal received with the Earth spectrum, the type of atmosphere (Figure 7.2) and the abundances of the main atmospheric species, that have spectral features, (Table 7.1) can be identified.

By the calculation of the brightness temperature of each band, a hypothetical atmospheric profile can be traced identifying temperature and height, this calculations allow to determine the surface temperature. By a model of the contribution function of the relative intensity depth between the spectral line and the continuous level, we can determine the depth of the layers of formation of a spectral line, and the results can be compared with the atmospheric profile (Figure 7.3).

The global parameters of the climate can be calculated by the integration to all the thermal range. The effective temperature of the planet correspond to the "bolometric" brightness temperature, the Bond albedo of the planet is retrieved by the application of the energy balance relation (Equation 2.9), assuming the radius of the planet can be measured independently, and the greenhouse parameter is finally given by Equation 2.10 (or Equation 2.12 for g_N).

Unlike spectra, light curves allow to study the time variability of each band and of its atmospheric constituents. The comparative analysis of the autocorrelation series of each band will give the rotation rate of the planet and/or the rotation rate of large weather systems (Section 6.3.3) as in the case of water worlds. Longitudinal curves illustrate the distribution, state and evolution of the various components of the atmosphere, notably biosignatures as H_2O, CO_2, and O_3. Finally, by the typification of a possible next generation telescope (spectral resolution, diameter, technique, S/N, etc...) we can simulate a complete observation. However, because the thermal emission spectrum depends both on the temperature profile and abundances of the infrared absorbents, the results might have degeneracies. Light curves are a promising way to identify them (von Paris et al., 2013).

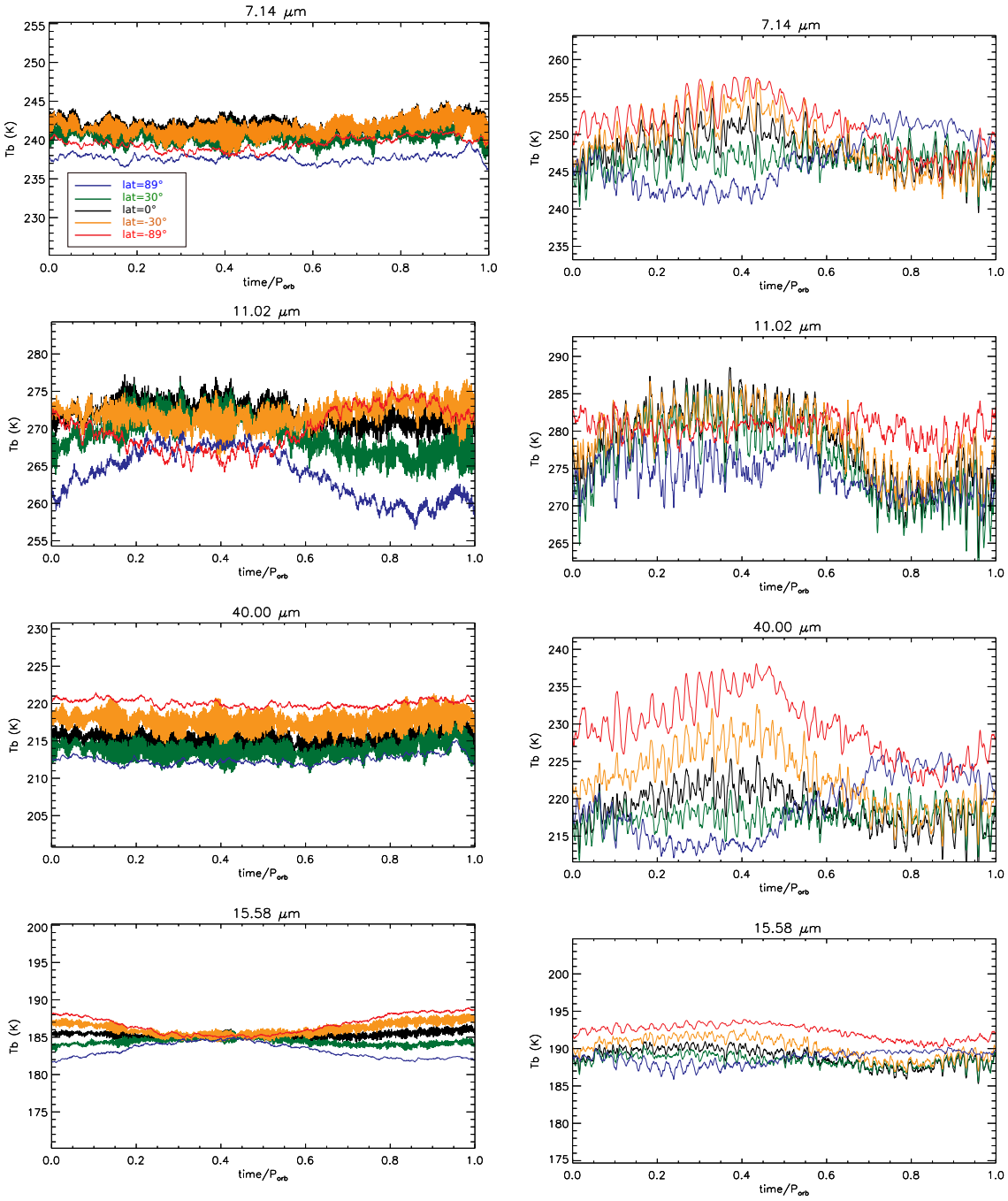

Figure 7.4 TOA-all-sky spectral brightness temperature annual series towards observers at 89N° (blue), 30N° (green), 0° (black), 30S° (orange), 89S° (red), for the planets Ete–1 (left) and Ete–10 (right), the rows correspond to the spectral bands of 7.14μm, 11.02μm, 40.00μm, and 15.58μm, described in Chapter 2.

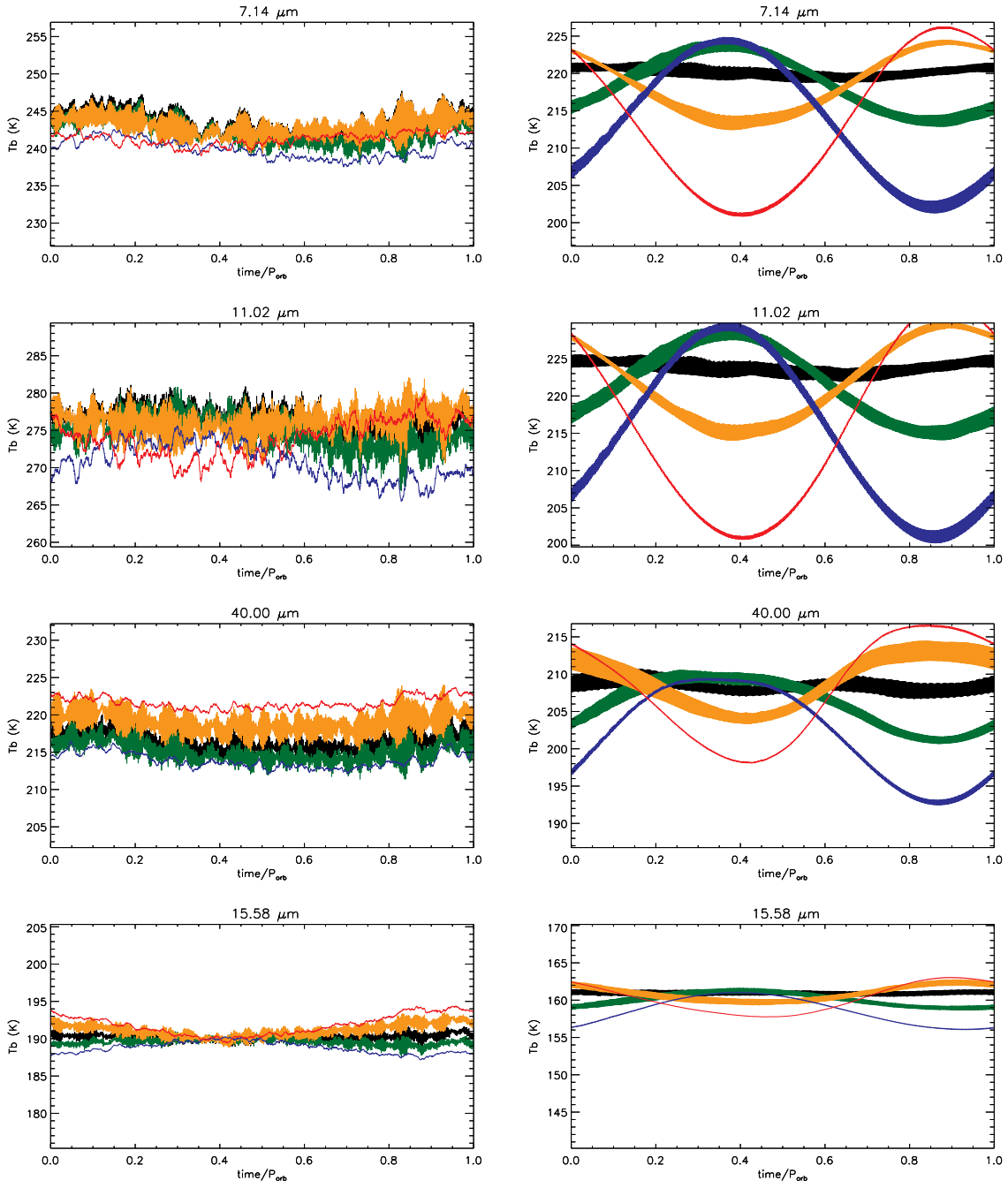

FIGURE 7.5 TOA-all-sky spectral brightness temperature annual series towards observers at 89N° (blue), 30N° (green), 0° (black), 30S° (orange), 89S° (red), for the planets Ote–1 (left) and SOte–1 (right), the rows correspond to the spectral bands of 7.14μm, 11.02μm, 40.00μm, and 15.58μm, described in Chapter 2.

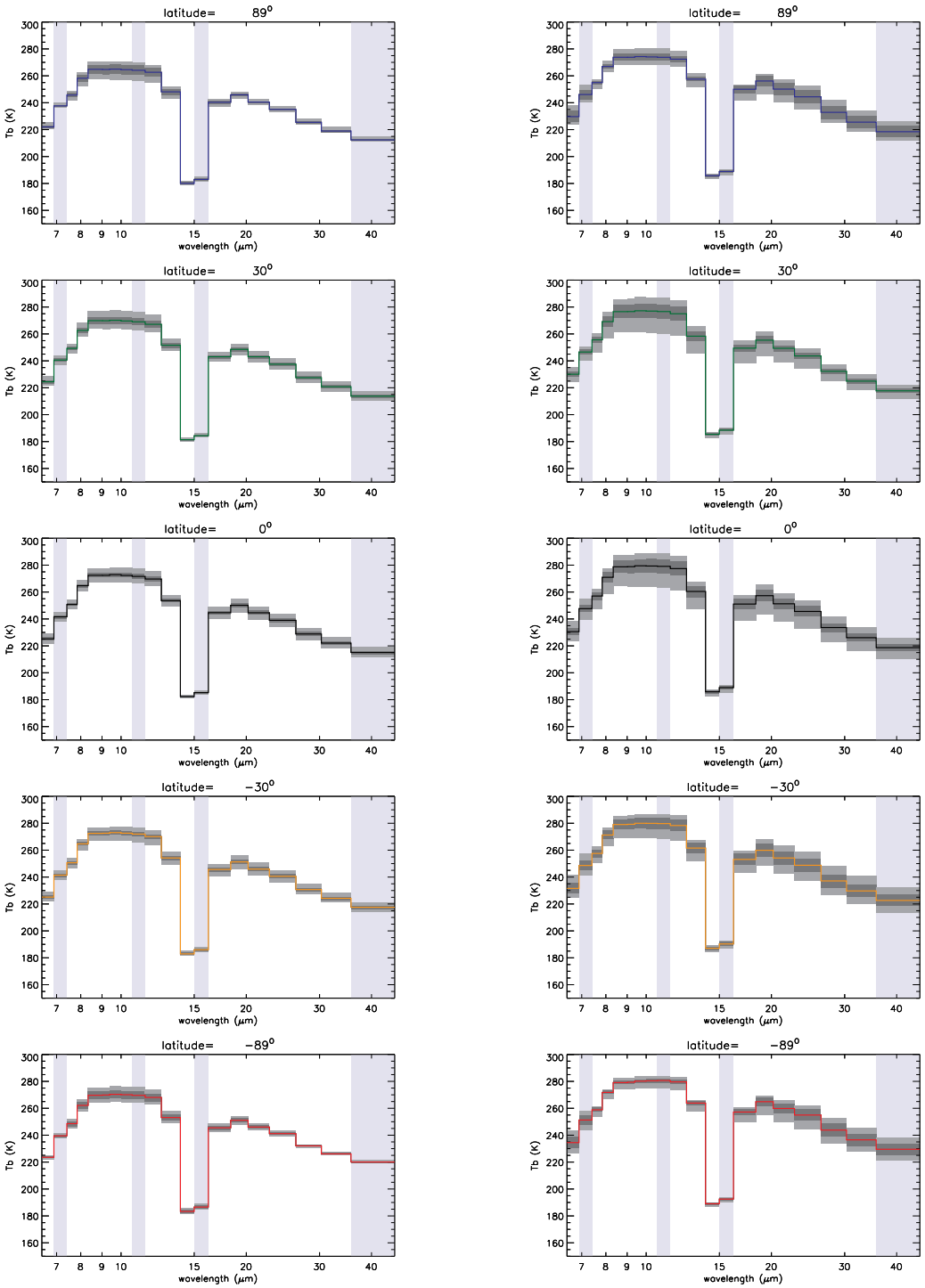

Figure 7.6 TOA-all-sky spectra towards observers at (from top to bottom) 89°N, 30°N, 0°, 30°S, and 89°S, for the planets Ete–1 (left) and Ete–10 (right).

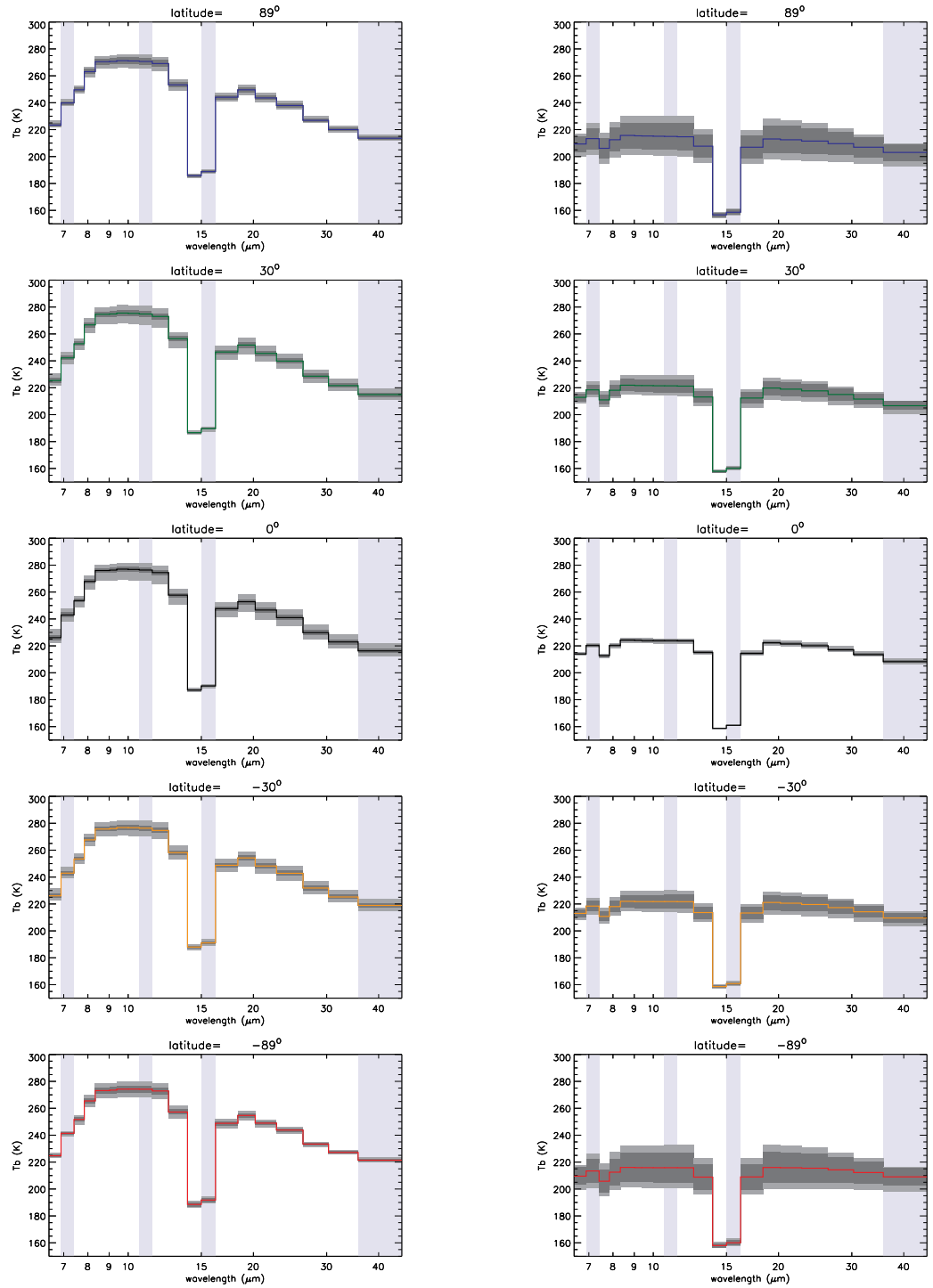

FIGURE 7.7 TOA-all-sky spectra towards observers at (from top to bottom) 89°N, 30°N, 0°, 30°S, and 89°S, for the planets O–1 (left) and SOte–1 (right).

Chapter 8

Conclusions

The study of the Earth-like planets is important to prepare the incoming detection and characterization of extrasolar habitable worlds. The use of climate models gives us the opportunity to built a variety of planets, by changing the planetary properties and simulating any geometry of observation, which it is important to understand their influence on the observables. In this thesis, we have used satellite and model results to simulate thermal light-curves of the Earth and several Earth-like planets, studying the climate and the circulation of the atmosphere and deriving some planetary properties from the spectro-photometric signal, such as the planetary rotation rate, the global temperature of the planet, the existence of seasons, the eccentricity of the orbit, weather patterns or the presence of moons.

8.1 Methods

– I have built a geometrical model that can simulate the point-like emission signal of an Earth-like planet received by an observer at any geometry and distance.

– By the comparison of mean limb darkening models and for the sake of simplicity we conclude that the Lambertian approximation is applicable on the simulation of the thermal emission of the Earth-like planets of our set.

– Our model can also calculate the global characteristics of the planet as the effective temperature, the Bond albedo, the greenhouse parameter, or the cloud radiative forcing to study the climate and to analyze the influence of the variation of these parameters on the signal.

– In addition, by the further analysis of the light curves, we can retrieve certain parameters such as the rotation rate, the albedo and the effective temperature. We can also built longitudinal maps to reveal warm and cold regions of the planet and include the effect of natural satellites.

8.2 Types of data

– Three types of data have been implemented by our model in order to obtain the planetary integrated mid-infrared emission in the direction of a remote observer randomly located.

– First I have used satellite validated data from NASA-SRB project in order to obtain an accurate reproduction of the thermal light curve of the Earth (Chapter 4).

– Secondly, I have used the Earth LMDZ GCM to reproduce the Earth and the results obtained are validated by the comparison with SRB data.

– Then, I have modeled nine Earth-like planets including: a slow Earth, an aquaplanet and a snowball planet with the orbital parameters of the Earth (Chapter 5), two aquaplanets with circular orbits and three synchronous aquaplanets (Chapter 6).

– The use of LMDZ generic model allows the application of data from narrow spectral bands which allows to study of the temporal evolution of the planetary spectrum, and also the distribution, abundances and evolution of its atmospheric components (Chapter 7).

8.3 Photometric variability of the Earth

– I have constructed a 3 hr resolution model of the integrated mid-infrared emission of the Earth over 20 years in the direction of a remote observer randomly located.

– The seasonal modulation dominates the variation of the signal. As expected, it is larger for the polar views because the planetary obliquity causes a bigger annual insolation change for these latitudes. For equatorial views, the seasonal maximum

occurs during the summer of the Northern Hemisphere, as the latter contains large continental masses whereas the Southern Hemisphere is dominated by the oceans.

– The rotational variability is detectable because of the uneven distribution of oceans and continents with geographical longitude. The daily maximum of the mid-infrared flux is shown when dry large masses of land, such as the Sahara desert, are in the observer's field of view. The daily minimum appears when cloudy humid regions such as the Indonesian area is visible, as iced big zone are confined to the poles.

– In the polar views, the distribution of land does not change with time but the diurnal temperature variation of large continental areas affects the signal, allowing the detection of the rotational period in the North Polar case.

– I find that the rotational variations have an amplitude of several percents, which is comparable to that of the seasonal variations for some latitudes.

– It is important to remark the strong influence of the weather patterns, humidity and clouds are sometimes able to mask the 24 hr rotation period of the signal for several days at a time. However, this effect can be solved by time folding.

– It is important to point out that the Earth does not exhibit a significant modulation associated with phase variation (phase curve). This is because the integrated thermal emission does not generally probe the boundary layer (first km of the atmosphere) where the diurnal cycle takes place.

– If unresolved, the Earth–Moon system would however present a phase variation of Lunar origin. A satellite of the size of the Moon would introduce a strong phase variability that would completely dominate over the planet's signal. This effect adds high complexity to its interpretation by photometry.

– At the light of these results it seems that future infrared photometric observations of terrestrial planets can be useful in order to characterize their atmospheric and surface features. If the planet is not completely covered by clouds, as Venus is, the presence of strong surface inhomogeneities (continents) can be extracted from the daily variations. The orbital variability can also give estimates of the planet effective temperature, the seasonal cycle, the eccentricity its orbit, and the distribution of land at larger scale.

8.4 Photometric variability of Earth-like planets

8.4.1 Planets in a terrestrial orbit

– I have studied the thermal light curves of four Earth-like planets: The Earth; a slow Earth, with a rotation period of 10 days; an aquaplanet with Earth orbital parameters and a snowball version of this aquaplanet. Climate is highly dependent on surface temperature, Bond albedo, rotation rate, cloud covering and continental distribution. Then, I have calculated the global parameters of the atmosphere, discuss the climatic conditions, and study the influence of the physical characteristics of the planet on the signal.

– In comparison with Earth's climate, a slow Earth has a colder climate, zonal winds are very slow and the meridional circulation dominates, it also has a diurnal convection cloud formation cycle in the form of huge monsoons and a thick layer of low clouds over the oceans. As a result of a large part of the surface is frozen. Unlike the Earth, there are equatorial superrotating winds in the upper levels of the troposphere.

– An aquaplanet analogue has a warmer climate, the greenhouse effect is severe because of the large fraction of high clouds. Surface temperatures of aquaplanets are influenced by the eccentricity of the orbit (the southern summer is warmer because at that moment the planet passes by the periastron).

– The snowball climate is cold and dry with very slow winds, a layer of low cloud covers the surface except in summer, when convection clouds are formed.

– The time series variability of Earth-like planets is produced by three main factors: the seasonality, by which the energy absorbed (and emitted) changes along the orbit because of the inclination of the rotation axis; the rotation of the planet, as the change in flux is created by the contrast between warm and cold areas of successive planetary views; and the diurnal variability, when the temperature cycle of a particular region produces a change in the emission.

– The rotation period of the signal can be retrieved, with a compromise of the length of the time series considered, if cloud lifetimes are longer than the rotation period or if the planet has cloud-convection regions, where clouds are

formed constantly. In this case, the regions are characterized for the low brightness temperature from the top of the clouds. The large humidity ratio associated with convection regions is the origin of the periodical signal.

– Finally, I have obtain the longitudinal curves of the planets, which allow us to identify warm and cold regions and the influence of the axial tilt (seasons) and eccentricity of the orbit.

8.4.2 Water Worlds

– I have studied the thermal emission of five aquaplanets with circular orbits and without axial tilt (without seasons): O–1 and O–10 have a rotation rate of 1 and 10 days, respectively; and three synchronous aquaplanets Os–1, Os–10, Os–360 with rotation rates of 1, 10 and 360 days, where the stellar constant is modified according to the orbital distance.

– Aquaplanets analogues are warmer than terrestrial planets, with an ITCZ with a high concentration of convective clouds because the large specific humidity. An aquaplanet with the same orbital parameters than the Earth has an effective temperature of 258 K, an aquaplanet analogue with a circular orbit and without axial tilt, has an effective temperature of 257 K. Synchronous aquaplanets however have low surface temperatures and the main part of the surface is frozen except for the antistellar region, an Earth analogue with a rotation rate of 1 day, has an effective temperature of 238 K.

– The warmest point is usually shifted by the circulation of the planet and being a convergence region, steady convection clouds cover the area, which has a slight effect over the signal by decreasing the TOA-emission at this point.

– Because of the low thermal inertia of water, the cloud absorption is the only source of flux variability in the signal. Thus, the period is retrieved by autocorrelation if the cloud lifetimes are longer than the period of the planet or if the clouds are linked to convergence regions.

– The period is retrieved in the case of the aquaplanet O–1 because the rotation rate is shorter than the clouds lifetimes. O–10 has a convergence region in the form

of a "chevron" pattern, however the region is an atmospheric phenomenon and it is not linked to surface steady features. The period obtained is shorter that the period of rotation of the planetary surface, because the equatorial superrotating winds in the upper troposphere drive the clouds of the "chevron" pattern. The movement of the chevron pattern is shown in longitudinal light curves.

– The period of tidally looked planets is retrieved because the convergence regions are tied to the surface temperature maximum.

8.5 Perspectives

– The use of LMDZ generic GCM spectral data gives the opportunity to reproduce Earth-like planet conditions and simulate the planetary signal detected by a distant observer. By the comparison of the signal received with the Earth spectrum, the type of atmosphere (Figure 7.2) and the abundances of the main atmospheric species, that have spectral features, (Table 7.1) can be identified.

– By the calculation of the brightness temperature of each band, a hypothetical atmospheric profile can be traced identifying temperature and height, this calculations allow to determine the surface temperature. By a model of the contribution function of the relative intensity depth between the spectral line and the continuous level, we can determine the depth of the layers of formation of a spectral line, and the results can be compared with the atmospheric profile (Figure 7.3).

– The global parameters of the climate can be calculated by the integration to all the thermal range. The effective temperature of the planet correspond to the "bolometric" brightness temperature, the Bond albedo of the planet is retrieved by the application of the energy balance relation (Equation 2.9), assuming the radius of the planet can be measured independently, and the greenhouse parameter is finally given by Equation 2.10 (or Equation 2.12 for g_N).

– Unlike spectra, light curves allow to study the time variability of each band and of its atmospheric constituents. The comparative analysis of the autocorrelation series of each band will give the rotation rate of the planet and/or the rotation rate

of large weather systems (Section 6.3.3) as in the case of water worlds. Longitudinal curves illustrate the distribution, state and evolution of the various components of the atmosphere, notably biosignatures as H_2O, CO_2, and O_3. Finally, by the typification of a possible next generation telescope (spectral resolution, diameter, technique, S/N, etc...) we can simulate a complete observation. However, because the thermal emission spectrum depends both on the temperature profile and abundances of the infrared absorbents, the results might have degeneracies. Light curves are a promising way to identify them (von Paris et al., 2013).

– The topic of this thesis was the study of the thermal emission of Earth-like planets. Although the observation of these type of planets will be possible in a decade, this model is also applicable to the study of other types of planets. The next step is to implement the model with the purpose of Super-Earths, as this type of planets are detectable nowadays.

Chapter 9

Conclusions (français)

Les conclusions finales de cette thèse sont présentées comme un résumé des conclusions indiquées dans chaque chapitre. L'étude des planètes telluriques est important pour préparer la détection et la caractérisation futures des planètes extrasolaires habitables. L'utilisation de modèles climatiques nous donne la possibilité de construire une grande variété de planètes, en modifiant les propriétés planétaires et de simuler n'importe quelle géométrie de l'observation, ce qui est important pour pouvoir comprendre leur influence sur les observables. Dans cette thèse, j'ai utilisé des donnés satellitaires et des donnés des modèles climatiques pour simuler l'emission thermique et les courbes de lumière de la Terre et de plusieurs planètes telluriques. L'analyse de nos résultats permet de étudier le climat, la circulation de l'atmosphère et de dériver des propriétés planétaires à partir du signal spectro-photométrique, comme le taux de rotation planétaire, la température globale de la planète, l'existence des saisons, l'excentricité de l'orbite, les conditions météorologiques ou la présence des satellites naturels.

9.1 Méthodes

– J'ai construit un modèle géométrique qui permet de simuler le signal de l'émission ponctuelle d'une exoplanète tellurique reçu par un observateur à toute géométrie et distance.

– Par la comparaison des modèles de la moyenne du "limb-darkening" terrestre

et dans l'intérêt de la simplicité, nous pouvons concluir que la loi de Lambert est applicable à la simulation de l'émission thermique de l'ensemble des planètes telluriques de cet étude.

– Le modèle peut également calculer les caractéristiques globales de la planète, comme par exemple la température effective, l'albédo de Bond, le paramètre à effet de serre, ou le forçage radiatif des nuages, qui sert à étudier le climat et à analyser l'influence de la variation de ces paramètres sur le signal thermique.

– D'ailleurs, par l'analyse des courbes de lumière, nous pouvons récupérer certains paramètres tels que la vitesse de rotation, l'albédo et la température effective de la planète. Nous pouvons également construire des cartes longitudinales, qui permettent de révéler les régions chaudes et froides de la planète et comprendre l'effet de satellites naturels dans le signal combiné des deux corps.

9.2 Types de données

– Trois types de données ont été utilisés par notre modèle afin d'obtenir l'émission infrarouge de la planète intégrée dans la direction d'un observateur distant situé au hasard.

– D'abord, j'ai travaillé avec des données satellitaires issus du projet SRB de la NASA, afin d'obtenir une reproduction exacte de la courbe de lumière thermique de la Terre (Chapitre 4).

– Deuxièmement, j'ai utilisé des donnés issus du modèle de circulation générale LMDZ pour simuler le signal thermique de la Terre et les résultats obtenus sont validés par la comparaison avec les données issus du SRB.

– Ensuite, j'ai modélisé neuf planètes telluriques, y compris : une Terre lente (avec un taux de rotation de 10 jours), une aquaplanète et une aquaplanète "boule de neige" avec les mêmes paramètres orbitaux de la Terre (Chapitre 5), deux aquaplanètes avec des orbites circulaires avec des taux de rotation de 1 et 10 jours respectivement et trois aquaplanètes synchrones à différents taux de rotation: 1 jour, 10 jours et 360 jour (Chapitre 6).

– L'utilisation du modèle LMDZ générique permet l'application des donnés en

bandes spectrales étroites et l'étude de la evolution temporel du spectre de la planète, et aussi de la distribution, les abondances et l'évolution de ses composants atmosphériques (Chapitre 7).

9.3 Variabilité photométrique de la Terre

– J'ai construit un modèle de l'émission infrarouge de la Terre avec une résolution temporel de 3 heures et intégrée pour un période de 20 ans dans la direction d'un observateur distant situé au hasard.

– La modulation saisonnière domine la variation du signal. Comme prévu, cette variation est plus large pour les vues polaires à cause de l'obliquité planétaire, qui produit un changement d'ensoleillement annuel plus importante pour ces latitudes. Pour les vues équatoriales, le maximum saisonnier se produit pendant l'été de l'hémisphère Nord, parce que celui-ci contient de grandes masses continentales alors que l'hémisphère sud est dominé par les océans.

– La variabilité rotationnel est détectable en principe en raison de la répartition inégale des océans et des continents avec la longitude géographique. Le maximum journalier du flux infrarouge apparaît lorsque des grandes masses sèches de la Terre, tels que le désert du Sahara, sont dans le champ de vision de l'observateur. Le minimum journalier, par contre, apparaît quand des régions nuageuses et humides, tels que la zone des moussons entre l'Inde et l'Indonésie, sont visibles, tant que les grandes zones glacés sont réservés aux pôles de la planète.

– Dans les vues polaires, la distribution des terres ne change pas avec le temps, mais la variation journalière de température de grandes zones continentales qui sont dans le champ de vision, produit une variation du signal, ce qui permet la détection de la période de rotation dans le cas du Pôle Nord.

– Les variations dues au mouvement de rotation de la Terre ont une amplitude de plusieurs pour cent, ce qui est comparable à celle des variations saisonnières pour certaines latitudes.

– Il est important de remarquer la grande influence des conditions météorologiques. L'humidité et les nuages sont capables de masquer la période de rotation du signal

pendant plusieurs jours. Cependant, cet effet peut être résolu en faisant le "time-folding" du signal.

– L'émission infrarouge de la Terre ne présente pas une modulation significative associée à la variation de phase (courbe de phase). En effet, l'émission thermique intégrée ne proviens pas généralement de la couche limite (première km de l'atmosphère) où le cycle diurne a lieu.

– Le système non résolu Terre-Lune présente toutefois une variation de phase d'origine lunaire. Un satellite de la taille de la Lune introduit une variabilité de phase importante qui domine complètement le signal de la planète. Cet effet ajoute une grande complexité à son interprétation par photométrie.

– À la lumière de ces résultats, nous concluons que les futures observations photométriques infrarouges des planètes terrestres seront utiles pour déterminer leurs caractéristiques atmosphériques et climatiques. Si la planète n'est pas complètement couvert par les nuages, comme il est le cas de Vénus, la présence de inhomogénéités de surface puissants (continents) peut être extraite à partir des variations journalières. La variation due au mouvement orbital de la planète peut également donner des estimations de sa température effective, du cycle saisonnier, de l'excentricité de son orbite, et de la distribution des continents dans sa surface.

9.4 Variabilité photométrique des planètes telluriques

9.4.1 Planètes avec une orbite terrestre

– J'ai étudié les courbes de lumière de l'émission thermique de quatre planètes telluriques : La Terre, une Terre lente avec une période de rotation de 10 jours, une aquaplanète avec les paramètres orbitaux de la Terre et de une aquaplanète "boule de neige". Le climat est très dépendant de la température de surface, du Bond albédo, de la vitesse de rotation, de la couverture nuageuse et de la distribution continentale. Premièrement, j'ai calculé les paramètres globaux de l'atmosphère, j'ai étudié les

conditions climatiques de la planète, et l'influence des caractéristiques physiques de la planète sur le signal.

– En comparaison avec le climat de la Terre, une Terre à rotation lente a des températures moyennes plus froides, les vents zonaux sont très lents et la circulation méridienne domine. En conséquence, une grande partie de la surface est congelée. Il y a un cycle diurne de formation des nuages de convection sous la forme d'énormes moussons sur les masses continentales et une couche épaisse des nuages basses au-dessus des océans. Contrairement à la Terre, il y a les vents zonales présentent des régimes de superrotation dans les niveaux supérieurs de la troposphère, jusqu'à une latitude de 60 dégrées.

– L'aquaplanète analogue a un climat plus chaud que la Terre, l'effet de serre est plus important en raison de la forte proportion de nuages de haute altitude. Dans le cas d'excentricité de l'orbite, les températures de surface sont influencées, l'été austral est plus chaud car à ce moment la planète passe par le périastre et au même temps, à cause de cette augmentation du gradient de température, il y a une expansion de la calotte polaire au Nord jusqu'à une latitude de 70 dégrées. Pour cette raison, l'hiver de l'hémisphère Nord est plus froid que cel de l'hémisphère Sud.

– Le climat de l'aquaplanète "boule de neige" est froid et sec, avec des vents très lents. Une couche de nuages basses recouvre la surface, sauf l'été, quand les nuages de convection sont formés dans tout l'hémisphère.

– La variabilité des séries temporelles de planètes telluriques est produite par trois facteurs principaux: la saisonnalité, par laquel l'énergie absorbée (et émise) change le long de l'orbite à cause de l'inclinaison de l'axe de rotation; la rotation de la planète, dont la variation de flux est créé par le contraste entre des zones chaudes et froides successives, produites par comme le désert du Sahara, comme la région humide de l'Indonésie; et la variabilité diurne, produite par le cycle de température d'une région particulière.

– La période de rotation de la planète peut être extrait du signal par le méthode de autocorrelation (en faisant un compromis de la longueur de la série temporelle considéré) si la durée de vie des nuages sont plus longues que la période de rotation ou si la planète a des régions de forte humidité avec formation des nuages de convection.

Dans ce cas, les nuages absorbent l'emission des couches inférieures et ces régions sont caractérisées pour la faible température de brillance de la partie supérieure des nuages. Le contraste des régions chaudes avec des régions de convection est à l'origine du signal périodique.

– Enfin , j'ai obtenu des courbes de lumière longitudinales, qui nous permettent d'identifier les régions chaudes et froides de la planète ainsi que l'influence de l'inclinaison de l'axe de rotation (saisons) et de l'excentricité de l'orbite.

9.4.2 Aquaplanètes

– J'ai étudié l'émission thermique de cinq aquaplanètes en orbite circulaire et sans inclinaison axiale (sans saisons) : O–1 et O–10 ont un taux de rotation de 1 et 10 jours, respectivement, et trois aquaplanètes synchrones Os–1, Os–10, Os–360 avec des taux de rotation de 1, 10 et 360 jours, où la constante stellaire est modifiée en fonction de la distance orbitale.

– Les aquaplanètes sont en général plus chaudes que les planètes telluriques, en raison de la grande humidité spécifique, en conséquence, la zone de convergence intertropicale a une forte concentration de nuages de convection. Une aquaplanète avec les mêmes paramètres orbitaux que la Terre a une température effective de $\sim$258 K, (en comparaison celle de la Terre est de $\sim$255 K)une aquaplanète analogue avec une orbite circulaire et sans inclinaison axiale a une température effective de $\sim$257 K. Les aquaplanètes synchrones ont des basses températures de surface et la plus part de la surface est gelée à l'exception de la région du point substellaire (ou une région prochaine quand le maximum de température de surface est déplacé à cause de la circulation atmosphérique). Un aquaplanète avec un taux de rotation de 1 jour a une température effective de $\sim$238 K.

– Dans des planètes synchrones, le point le plus chaud est généralement décalé du point substellaire à cause de de l'inertie thermique et de la circulation de l'atmosphère. Le point chaud est une région de convergence de la circulation atmosphérique avec une condensation importante des nuages de convection, ce qui a un effet léger sur le signal d'émission en diminuant l'émission de la couche supérieur de la atmosphere

dans cet point, parce que l'émission provient du sommet de ce type de nuages.

– En raison de la faible inertie thermique de l'eau, l' absorption des nuages est la seule source de variabilité rotationnelle du flux dans le signal, spécialement dans le cas des aquaplanètes avec une orbite circulaire. Ainsi, la période est récupéré par autocorrélation si la durée de vie des nuages sont plus longues que la période de la planète ou si les nuages sont liées aux régions de convergence.

– La période est récupéré dans le cas de l'aquaplanet O–1 parce que le taux de rotation est plus court que la durée de vie des nuages. O–10 présente une région de convergence sous la forme de "chevron", ce qui est un phénomène atmosphérique produit pour la superrotation différentielle de la troposphere. La période obtenue est plus courte que la période de rotation de la surface de la planète, parce que les vents en superrotation dans la haute troposphère, au sommet des nuages convectives, transportent les nuages en forme de "chevron". Le "chevron" est plus ouvert vers les hautes latitudes de la planète, par ce que la vitesse des vents en superrotation augmente avec la latitude. Le mouvement du motif de chevron est représenté sur les courbes de lumière longitudinales (flux vs. longitude).

– La période de rotation des aquaplanètes synchrones est récupéré directement de la courbe de lumière parce que la température de brillance est correlée avec la phase d'illumination de la planète. Les régions de convergence, dont les nuages diminuent le flux, sont liés à la température maximale de surface, et par consequence le signal intégrée ne varie pas considérablement.

9.5 Perspectives

– L'utilisation des données spectrales du LMDZ générique donne la possibilité de reproduire les conditions des planètes telluriques et de simuler le signal planétaire détecté par un observateur lointain. Par la comparaison du signal reçu avec le spectre de la Terre, les conditions de l'atmosphère (Figure 7.2) et l'abondance des principales espèces qui ont des caractéristiques spectrales, (Tableau 7.1) peuvent être identifiés.

– Par le calcul de la température de brillance de chaque bande, un profil

hypothétique atmosphérique peut être tracée par l'identification de la température et l'altitude, ce calcul permet de déterminer la température de surface. Par un modèle de la fonction de la contribution de la profondeur de l'intensité relative entre la ligne spectral et le continu, nous pouvons déterminer la profondeur des couches de la formation d'une ligne spectrale, et les résultats peuvent être comparés avec des profils atmosphériques (Figure 7.3).

– Les paramètres globaux du climat peuvent être calculés par l'intégration dans tout l'infrarouge thermique, parce que les planètes terrestres la grande majorité de son émission est dans cet domaine spectrale. La température effective de la planète correspond à la température de brillance "bolométrique", l'albédo de Bond de la planète est récupéré par l'application de la relation de l'équilibre énergétique (Équation 2.9), en supposant que le rayon de la planète peut être mesuré indépendamment, et le paramètre à effet de serre est finalement donnée par l'Équation 2.10 (ou l'Équation 2.12 pour g_N).

– Contrairement aux spectres planétaires, les courbes de lumière permet d'étudier la variabilité temporelle de chaque bande et de ses constituants atmosphériques. L'analyse comparative de la série d'autocorrélation de chaque bande donnera la vitesse de rotation de chaque couche de la atmosphère et portant le taux de rotation de grands systèmes météorologiques (Section 6.3.3) comme dans le cas des aquaplanètes. Les courbes de lumière longitudinales illustrent la distribution, l'état et l'évolution des différents composants de l'atmosphère, notamment des bio-signatures tels que H_2O, CO_2 et O_3. Finalement, par la typification d'un possible télescope de nouvelle génération (résolution spectrale, diamètre, technique, S/N, etc...), nous pouvons simuler une observation complète. Cependant, parce que le spectre d'émission thermique dépend à la fois du profil de température et des abondances des composants absorbants, les résultats peuvent avoir des dégénérations. Les courbes de lumière sont une voie prometteuse pour les identifier (von Paris et al., 2013).

– Le sujet de cette thèse est l'étude de l'émission thermique de planètes telluriques. Bien que l'observation de ce type de planètes sera possible dans une dizaine d'années, ce modèle est également applicable à l'étude d'autres types de planètes. L'étape suivante consiste à mettre en œuvre le modèle pour étudier des Super-Terres, car

aujourd'hui ce type de planètes sont détectables.

COMPLEMENTS

Acronyms

BTMG	*Brightness Temperature Meridional Gradient*
C	*Conjunction*
CM	*Central Meridian*
CNES	*Centre National d'Etudes Spatiales*
CoRoT	*pour Convection Rotation et Transits planétaires (space telescope)*
CRF	*Cloud Radiative Forcing*
EChO	*Exoplanet Characterization Observatory*
E-ELT	*European Extremely Large Telescope*
ESA	*European Space Agency*
Ete-	*the Earth*
EQ	*Eastern Quadrature*
FFT	*Fast Fourier Transform*
GCM	*General Circulation (or Global Climate) Model*
GEWEX	*Double Side Band*
HARPS	*Early Asymptotic Giant Branch*
HC	*Hadley Cell*
HIRES	*E-ELT high-resolution Spectrograph*
HZ	*Habitable Zone*
IR	*Infrared Radiation*
ITCZ	*Inter-Tropical Convergence Zone*
JWST	*James Webb Space Telescope*
LAB	*Laboratoire d'Astrophysique de Bordeaux*
LMD	*Laboratoire de Météorologie Dynamique de Paris*
LMDZ	*LMD's GCM*
LW	*LongWave radiation*
METIS	*Mid-infrared E-ELT Imager and Spectrograph*
NA	*Northern Autumn*
NASA	*National Aeronautics and Space Administration*
NE	*Northern Equinox*
NS	*Northern Solstice*

NSp	*Northern Spring*
NSu	*Northern Summer*
NW	*Northern Winter*
O	*Opposition*
O-	*Aquaplanet*
Os-	*Synchronous Aquaplanet*
Ote-	*Aquaplanet (with an Earth orbit)*
PAL	*Present Atmospheric Level*
SE	*Southern Equinox*
SOte-	*Snowball Aquaplanet (with an Earth orbit)*
SRB	*Surface Radiative Budget*
SS	*Southern Solstice*
SSu	*Southern Summer*
STMG	*Surface Temperature Meridional Gradient*
SW	*ShortWave radiation*
TOA	*Top Of the Atmosphere*
UT	*Universal Time*
WQ	*Western Quadrature*

Table 9.1. Useful Physical Constants

Constant	Symbol	Numerical value
Speed of light	c	$3.0 \cdot 10^{8}\ m\ s^{-1}$
Planck's constant	h	$6.63 \cdot 10^{-34}\ J\ s$
Stefan-Boltzmann constant	σ	$5.67 \cdot 10^{-8}\ W\ m^{-2}\ K^{-4}$
Boltzmann constant	k_B	$1.38 \cdot 10^{-23}\ J\ K^{-1}$
Universal gas constant	R	$8.31\ J\ K^{-1}\ mol^{-1}$
Solar Luminosity	$L_\odot$	$1.38 \cdot 10^{-23}\ J\ K^{-1}$
Solar Constant	F_S	$1369\ W\ m^{-2}$
Solar mean Radius	$R_\odot$	$6.96 \cdot 10^{8}\ m$
Solar Mass	$M_\odot$	$1.989 \cdot 10^{30}\ kg$
Earth mean Radius	$R_\oplus$	$6.371 \cdot 10^{6} m$
Earth Mass	$M_\oplus$	$5.972 \cdot 10^{24}\ kg$
Mean distance Sun-Earth	d_{se}	$1\ UA$
Earth's mean rotation rate	Ω	$7.29 \cdot 10^{-5}\ s^{-1}$
Mean gravity acceleration	g	$9.81\ m\ s^{-2}$
Standard surface pressure	p_0	$1013.25\ hPa\ (bar)$
Density of dry air at standard conditions	ρ_0	$1.29\ kg\ m^{-3}$
Heat capacity of dry air at constant presssure (s.c.)	c_p	$1005\ J\ K^{-1}\ kg^{-1}$
Molar mass of dry air	M	$28.97\ kg\ kmol^{-1}$
Specific gas constant of dry air	R_{sp}	$287\ J\ K^{-1}\ kg^{-1}$
Astronomical unit	UA	$149.597 \cdot 10^{9}\ m$
Parsec	pc	$3.086 \cdot 10^{16}\ m$

List of figures

List of tables

Bibliography

Adams, E. R., Seager, S., & Elkins-Tanton, L. 2008, *'Ocean Planet or Thick Atmosphere: On the Mass-Radius Relationship for Solid Exoplanets with Massive Atmospheres'*, *Astrophys. J.*, **673**, 1160.

Arnold, L., Gillet, S., Lardière, O., Riaud, P., & Schneider, J. 2002, *'A test for the search for life on extrasolar planets. Looking for the terrestrial vegetation signature in the Earthshine spectrum'*, *Astron. Astrophys.*, **392**, 231

Arnold, L. 2008, *'Earthshine Observation of Vegetation and Implication for Life Detection on Other Planets. A Review of 2001-2006 Works'*, *Space Sci. Rev.*, **135**, 323

Arnold, L., Bréon, F.-M., & Brewer, S. 2009, *'The Earth as an extrasolar planet: the vegetation spectral signature today and during the last Quaternary climatic extrema'*, International Journal of Astrobiology, **8**, 81

Bakun, A. 1990, *'Global Climate Change and Intensification of Coastal Ocean Upwelling'*, Science, **247**, 198

Batalha, N. M., Borucki, W. J., Bryson, S. T., et al. 2011, *'Kepler's First Rocky Planet: Kepler-10b'*, *Astrophys. J.*, **729**, 27

Belousova, E. A., Kostitsyn, Y. A., Griffin, W. L., et al. 2010, *'The growth of the continental crust: Constraints from zircon Hf-isotope data'*, Lithos, **119**, 457

Belu, A. R., Selsis, F., Morales, J.-C., et al. 2011, *'Primary and secondary eclipse spectroscopy with JWST: exploring the exoplanet parameter space'*, *Astron. Astrophys.*, **525**, A83

Bonfils, X., Delfosse, X., Udry, S., et al. 2013, *'The HARPS search for southern extra-solar planets. XXXI. The M-dwarf sample'*, *Astron. Astrophys.*, **549**, A109

Bracewell, R. N. 1978, *'Detecting nonsolar planets by spinning infrared interferometer'*, *Nature*, **274**, 780

Brooks, D. R., & Fenn, M. A. 1989, *'Parameterized Desert/Clear Atmosphere Limb-Darkening Model Derived From Earth Radiation Budget Satellite Along Track Measurements'*, Journal of Geophys. Research, **94**, 9947

Catanzarite, J., Shao, M., Tanner, A., Unwin, S., & Yu, J. 2006, *'Astrometric Detection of Terrestrial Planets in the Habitable Zones of Nearby Stars with SIM PlanetQuest'*, Publ. Astron. Soc. Pacific, **118**, 1319

Cash, B. A., Kushner, P. J., & Vallis, G. K. 2002, *'The Structure and Composition of the Annular Modes in an Aquaplanet General Circulation Model'*, Journal of Atmospheric Sciences, **59**, 3399

Cash, W., et al. 2009, *'The New Worlds Observer: the astrophysics strategic mission concept study'*, Proc. SPIE, 7436

Catala, C., & PLATO Consortium 2008, *'PLATO: PLAnetary Transits and Oscillations of stars'*, Journal of Physics Conference Series, 118, 012040

Chelton, D. B., Deszoeke, R. A., Schlax, M. G., El Naggar, K., & Siwertz, N. 1998, *'Geographical Variability of the First Baroclinic Rossby Radius of Deformation'*, J. Phys. Oceanography, **28**, 433

Christensen, P. R., & Pearl, J. C. 1997, *'Initial data from the Mars Global Surveyor thermal emission spectrometer experiment: Observations of the Earth'*, J. Geophys. Res., **102**, 10875

Cockell, C. S., Herbst, T., Léger, A., et al. 2009, *'DarwinÑan experimental astronomy mission to search for extrasolar planets'*, Experimental Astronomy, **23**, 435

Codron, F. 2012, *'Ekman heat transport for slab oceans'*, Climate Dynamics, **38**, 379

Cook, K. H. 2003, *'Role of Continents in Driving the Hadley Cells'*, Journal of Atmospheric Sciences, **60**, 957

Cowan, N. B., Agol, E., & Charbonneau, D. 2007, *'Hot nights on extrasolar planets: mid-infrared phase variations of hot Jupiters'*, *MNRAS*, **379**, 641

Cowan, N. B., & Agol, E. 2008, *'Inverting Phase Functions to Map Exoplanets'*,*Astrophys. J. Lett.*, **678**, L129

Cowan, N. B., Agol, E., Meadows, V. S., et al. 2009, *'Alien Maps of an Ocean-bearing World'*,*Astrophys. J.*, **700**, 915

Cowan, N. B., Robinson, T., Livengood, T. A., et al. 2011, *'Rotational Variability of Earth's Polar Regions: Implications for Detecting Snowball Planets'*, *Astrophys. J.*, **731**, 76C

Cowan, N. B., & Agol, E. 2011, *'A Model for Thermal Phase Variations of Circular and Eccentric Exoplanets',Astrophys. J.*, **726**, 82

Cowan, N. B., Voigt, A., & Abbot, D. S.: 2012, *'Thermal Phases of Earth-like Planets: Estimating Thermal Inertia from Eccentricity, Obliquity, and Diurnal Forcing'*, *Astrophys. J.*, **757(1)**, 80

Crossfield, I. J. M., Hansen, B. M. S., Harrington, J., et al. 2010, *'A New 24 ?m Phase Curve for ? Andromedae b'*, *Astrophys. J.*, **723**, 1436

Danchi, W. C., & Lopez, B. 2007, *'The Fourier Kelvin Stellar Interferometer (FKSI)–A practical infrared space interferometer on the path to the discovery and characterization of Earth-like planets around nearby stars'*, C. R. Phys., **8**, 396

del Genio, A. D., & Suozzo, R. J. 1987, *'A comparative study of rapidly and slowly rotating dynamical regimes in a terrestrial general circulation model'*, Journal of Atmospheric Sciences, **44**, 973

del Genio, A. D., & Zhou, W. 1996, *'Simulations of Superrotation on Slowly Rotating Planets: Sensitivity to Rotation and Initial Condition'*, Icarus, **120**, 332

Demory, B.-O., Gillon, M., Seager, S., et al. 2012, *'Detection of Thermal Emission from a Super-Earth'*, *Astrophys. J. Lett.*, **751**, L28

Des Marais, D. J., Harwit, M. O., Jucks, K. W., et al. 2002, *'Remote Sensing of Planetary Properties and Biosignatures on Extrasolar Terrestrial Planets'*, Astrobiology, **2**, 153

Doutriaux-Boucher, M., & Quaas, J. 2004, *'Evaluation of cloud thermodynamic phase parameterizations in the LMDZ GCM by using POLDER satellite data'*, *Geophys. Res. Lett.*, **31**, 6126

Dressing, C. D., & Charbonneau, D. 2013, *'The Occurrence Rate of Small Planets around Small Stars'*, *Astrophys. J.*, **767**, 95

Edson, A., Lee, S., Bannon, P., Kasting, J. F., & Pollard, D. 2011, *'Atmospheric circulations of terrestrial planets orbiting low-mass stars'*, Icarus, **212**, 1

Enderton, D., & Marshall, J. 2009, *'Explorations of Atmosphere-Ocean-Ice Climates on an Aquaplanet and Their Meridional Energy Transports'*, Journal of Atmospheric Sciences, **66**, 1593

Flament, N., Coltice, N., & Rey, P. F. 2008, *'A case for late-Archaean continental emergence from thermal evolution models and hypsometry'*, Earth and Planetary Science Letters, **275**, 326

Ford, E. B., Seager, S., & Turner, E. L. 2001, *'Characterization of extrasolar terrestrial planets from diurnal photometric variability'*, Nature, **412**, 885

Forget, F., Wordsworth, R., Millour, E., Madeleine, J.-B., Kerber, L., Leconte, J., Marcq, E., & Haberle, R. M. 2013, *'3D modelling of the early martian climate under a denser CO_2 atmosphere: Temperatures and CO_2 ice clouds'*, Icarus, **222**, 81

Fortney, J. J., Cooper, C. S., Showman, A. P., Marley, M. S., & Freedman, R. S. 2006, *'The Influence of Atmospheric Dynamics on the Infrared Spectra and Light Curves of Hot Jupiters'*, Astrophys. J., **652**, 746

Frierson, D. M. W., Lu, J., & Chen, G. 2007, *'Width of the Hadley cell in simple and comprehensive general circulation models'*, Geophys. Res. Lett., **34**, 18804

Fu, Q., Liou, K. N., Cribb, M. C., Charlock, T. P., & Grossman, A.,1997, *'Multiple Scattering Parameterization in Thermal Infrared Radiative Transfer'*, J. Atmos. Sci., **54**, 2799

Gaidos, E., & Williams, D. M. 2004, *'Seasonality on terrestrial extrasolar planets: inferring obliquity and surface conditions from infrared light curves'*, New Astronomy, **10**, 67

Gappinger, R. O., Diaz, R. T., Martin, S. R., Loya, F. M., & Lawson, P. R. 2007, *'Current progress on TPF-I mid-infrared achromatic nulling at the Jet Propulsion Laboratory'*, SPIE Conference Series, 6693

Giorgini, J. D., Yeomans, D. K., Chamberlin, A. B., et al. 1996, *'JPL's On-Line Solar System Data Service'*, BAAS, **28**, 1158

Gómez-Leal, I., Pallé, E., & Selsis, F.: 2012, *'Photometric Variability of the Disk-integrated Thermal Emission of the Earth'*, Astrophys. J., **752(1)**, 28

Gómez-Leal, I., Codron, F., & Selsis, F., 2013, *'Photometric Variability of the Disk-integrated Thermal Emission of Earth-like planets'*, (submitted to Astron. Astrophys.)

Gómez-Leal, I., Codron, F., & Selsis, F., 2013, *'Photometric Variability of the Disk-integrated Thermal Emission of Aquaplanets'*, (submitted to Astron. Astrophys.)

Greene, L. L. 1998, *'The role of continentality in seasonal variations of the Hadley circulation'*, M.S. thesis, Dept. of Earth and Atmospheric Sciences, Cornell University, 37 pp.

Guitreau, M., Blichert-Toft, J., Martin, H., Mojzsis, S. J., & Albarède, F. 2012, *'Hafnium isotope evidence from Archean granitic rocks for deep-mantle origin of continental crust'*, Earth and Planetary Science Letters, **337**, 211

Gupta, S. K., Darnell, W. L., & Wilber, A. C. 1992, *'A Parameterization for Longwave Surface Radiation from Satellite Data: Recent Improvements'*, J. Appl. Meteorol., **31**, 1361

Hamdani, S., Arnold, L., Foellmi, C., et al. 2006, *'Biomarkers in disk-averaged near-UV to near-IR Earth spectra using Earthshine observations'*, *Astron. Astrophys.*, **460**, 617

Hearty, T. and Song, I. and Kim, S. and Tinetti, G. 2009, *'Mid-Infrared Properties of Disk Averaged Observations of Earth with AIRS'*, *Astrophys. J.*, **693**, 1763

Heath, M. J., Doyle, L. R., Joshi, M. M., & Haberle, R. M. 1999, *'Habitability of Planets Around Red Dwarf Stars'*, Origins of Life and Evolution of the Biosphere, **29**, 405

Hodges, K. I., Chappell, D. W., Robinson, G. J., & Yang, G. 2000, *'An Improved Algorithm for generating Global Window Brightness Temperatures from Multiple Satellite Infrared Imaginery'*, Journal of Atmospheric and Oceanic Technology, **17**, 1296

Hourdin, F., Musat, I., Bony, S., et al. 2006, *'The LMDZ4 general circulation model: climate performance and sensitivity to parametrized physics with emphasis on tropical convection'*, Climate Dynamics, **27**, 787

Hourdin, F., Grandpeix, J.-Y., Rio, C., et al. 2012, *'LMDZ5B: the atmospheric component of the IPSL climate model with revisited parameterizations for clouds and convection'*, Climate Dynamics, 79

Hunt, B. G.: 1979, *'The Influence of the Earth's Rotation Rate on the General Circulation of the Atmosphere'*, Journal of Atmospheric Sciences, 36, 1392

Joshi, M. M., Haberle, R. M., & Reynolds, R. T. 1997, *'Simulations of the Atmospheres of Synchronously Rotating Terrestrial Planets Orbiting M Dwarfs: Conditions for Atmospheric Collapse and the Implications for Habitability'*, *Icarus*, **129**, 450

Joshi, M. 2003, *'Climate Model Studies of Synchronously Rotating Planets'*, Astrobiology, **3**, 415

Joshi, M. M., & Haberle, R. M. 2012, *'Suppression of the Water Ice and Snow Albedo Feedback on Planets Orbiting Red Dwarf Stars and the Subsequent Widening of the Habitable Zone'*, Astrobiology, **12**, 3

Kalnay, E., Kanamitsu, M., Kistler, R., et al. 1996, *'The NCEP/NCAR 40-Year Reanalysis Project'*, Bulletin of the American Meteorological Society, **77**, 437

Kaltenegger, L., & Fridlund, M. 2006, *'Characteristics of proposed 3 and 4 telescope configurations for Darwin and TPF-I'*, IAU Colloq. 200: Direct Imaging of Exoplanets: Science & Techniques, 255

Kasting, J. F., & Holm, N. G. 1992, *'What determines the volume of the oceans?'*, Earth and Planetary Science Letters, **109**, 507

Kitzmann, D., Patzer, A. B. C., von Paris, P., et al. 2010,*'Clouds in the atmospheres of extrasolar planets. I. Climatic effects of multi-layered clouds for Earth-like planets and implications for habitable zones'*, *Astron. Astrophys. Suppl. Ser.*, **511**, A66

Kitzmann, D., Patzer, A. B. C., von Paris, P., Godolt, M., & Rauer, H. 2011, *'Clouds in the atmospheres of extrasolar planets. II. Thermal emission spectra of Earth-like planets influenced by low and high-level clouds'*, *Astron. Astrophys. Suppl. Ser.*, **531**, A62

Knutson, H. A., Charbonneau, D., Allen, L. E., et al. 2007, *'A map of the day-night contrast of the extrasolar planet HD 189733b'*, *Nature*, **447**, 183

Knutson, H. A., Charbonneau, D., Allen, L. E., Burrows, A., & Megeath, S. T. 2008, *'The 3.6-8.0 μm Broadband Emission Spectrum of HD 209458b: Evidence for an Atmospheric Temperature Inversion'*, *Astrophys. J.*, **673**, 526

Kuchner, M. J. 2003, *'Volatile-rich Earth-Mass Planets in the Habitable Zone'*, *Astrophys. J. Lett.*, **596**, L105

Lawson, P. R., et al. 2007, *'Terrestrial planet finder interferometer: 2006-2007 progress and plans'*, Proc. SPIE., 6693

Leconte, J., Forget, F., Charnay, B., Wordsworth, R., Selsis, F., & Millour, E. 2013, *'3D climate modeling of close-in land planets: Circulation patterns, climate moist bistability and habitability'*, arXiv:1303.7079

Léger, A., Selsis, F., Sotin, C., et al. 2003, *'A new family of planets? "Ocean Planets"'*, Earths: DARWIN/TPF and the Search for Extrasolar Terrestrial Planets, **539**, 253

Léger, A., Selsis, F., Sotin, C., et al. 2004, *'A new family of planets? "Ocean-Planets"'*, *Icarus*, **169**, 499

Lewis, N. K., Knutson, H. A., Showman, A. P., et al. 2013, *'Orbital Phase Variations of the Eccentric Giant Planet HAT-P-2b'*, *Astrophys. J.*, **766**, 95

Livengood, T. A., Deeming L. D., A'Hearn, M. F., et al. 2011, *'Properties of an Earth-Like Planet Orbiting a Sun-Like Star: Earth Observed by the EPOXI Mission'*, Astrobiology, **11**, 907L

López-Valverde, M. A., López-Puertas, M., Funke, B., et al. 2011, *'Modeling the atmospheric limb emission of CO2 at 4.3 ?m in the terrestrial planets'* ,Planetary and Space Science, **59**, 988

Lu, J., Vecchi, G. A., & Reichler, T. 2007, *'Expansion of the Hadley cell under global warming'*, *Geophys. Res. Lett.*, **34**, 6805 .

Martín, E. L., & Guenther, E. 2006, *'Detectability of rocky planets with ELT infrared spectroscopy'*, The Scientific Requirements for Extremely Large Telescopes, **232**, 373

Marois, C., Macintosh, B., Barman, T., et al. 2008, *'Direct Imaging of Multiple Planets Orbiting the Star HR 8799'*, Science, **322**, 1348

Marotzke, J., & Botzet, M. 2007, *'Present-day and ice-covered equilibrium states in a comprehensive climate model',Geophys. Res. Lett.*, **34**, 16704

Marshall, J., Ferreira, D., Campin, J.-M., & Enderton, D. 2007, *'Mean Climate and Variability of the Atmosphere and Ocean on an Aquaplanet'*, Journal of Atmospheric Sciences, **64**, 4270

Maurin, A.-S., Selsis, F., Hersant, F., & Belu, A. 2012, *'Thermal phase curves of nontransiting terrestrial exoplanets. II. Characterizing airless planets'*, *Astron. Astrophys.*, **538**, A95

Mayor, M., Marmier, M., Lovis, C., et al. 2011, *'The HARPS search for southern extra-solar planets XXXIV. Occurrence, mass distribution and orbital properties of super-Earths and Neptune-mass planets'*, arXiv:1109.2497

Montañés Rodriguez, P., Pallé, E., Goode, P. R., et al. 2004, *'The earthshine spectrum'*, Advances in Space Research, **34**, 293

Murray, K. C., Christensen, P. R., Mehall, G. L., et al. 2003, *'2001 Mars Odyssey THEMIS Data Archive'*, Lunar and Planetary Institute Science Conference Abstracts, **34**, 1363

Merlis, T. M., & Schneider, T. 2010, *'Atmospheric dynamics of Earth-like tidally locked aquaplanets'*, Journal of Advances in Modeling Earth Systems, **2**, 13

Minnis, P., Young, D. F., & Harrison, E. F. 1991, *'Examination of the Relationship between Outgoing Infrared Window and Total Longwave Fluxes Using Satellite Data'*, Journal of Climate, **4**, 1114

Mitchell, J. L., & Vallis, G. K. 2010, *The transition to superrotation in terrestrial atmospheres*, Journal of Geophysical Research (Planets), ,**115**, 12008

Moskovitz, N. A., Gaidos, E., & Williams, D. M., 2009, *'The Effect of Lunarlike Satellites on the Orbital Infrared Light Curves of Earth-Analog Planets'*, Astrobiology, **9**, 269

Oliva, E., & Origlia, L. 2008, *'High-resolution near-IR spectroscopy: from 4m to 40m class telescopes'*, *SPIE Conference Series*, 7014,

Ollivier, M., Léger, A., Sekulic, C. A. P., et al. 1999, *'Nulling Interferometry for the DARWIN Mission - Laboratory Demonstration Experiment'*, Working on the Fringe: Optical and IR Interferometry from Ground and Space, **194**, 443

Ollivier, M., Mariotti, J.-M., Léger, A., et al. 2001, *'Interferometric coronography for the DARWIN space mission - Laboratory demonstration experiment'*, *Astron. Astrophys.*, **370**, 1128

Ollivier, M., Chazelas, B., & Bordé, P. 2008, *'Characterizing Earth-like planets: from CoRoT to DARWIN/TPF and beyond'*, Physica Scripta Volume T, **130**, 014031

Paillet, J. 2006, *'Exotic Earths: Forming Habitable Worlds with Giant Planet Migration'*, PhD thesis, Université Paris XI

Pallé, E., Montañés-Rodríguez, P., Goode, P. R., et al. 2004, *'The Earthshine Project: update on photometric and spectroscopic measurements'*, Adv. Space Research, **4**, 288

Pallé, E., Ford, E. B., Seager, S., Montañés-Rodríguez, P., & Vazquez, M. 2008, *'Identifying the Rotation Rate and the Presence of Dynamic Weather on Extrasolar Earth-like Planets from Photometric Observations'*, *Astrophys. J.*, **676**, 1319

Pallé, E., Zapatero Osorio, M. R., Barrena, R., Montañés-Rodríguez, P., & Martín, E. L. 2009, *'Earth's transmission spectrum from lunar eclipse observations'*, *Nature*, **459**, 814

Pallé, E., Zapatero Osorio, M. R., & García Muñoz, A. 2011, *'Characterizing the Atmospheres of Transiting Rocky Planets Around Late-type Dwarfs'*, *Astrophys. J.*, **728**, 19

Petigura, E. A., Marcy, G. W., & Howard, A. W. 2013, *'A Plateau in the Planet Population Below Twice the Size of Earth'*, arXiv:1304.0460

Philander, S. G. H., Gu, D., Lambert, G., et al. 1996, *'Why the ITCZ Is Mostly North of the Equator'*, Journal of Climate, **9**, 2958

Pierrehumbert, R. T. 2005, *'Climate dynamics of a hard snowball Earth'*, Journal of Geophysical Research (Atmospheres), **110**, 1111

Rauer, H., & Catala, C. 2011, *'The PLATO mission'*, IAU Symposium, **276**, 354

Rauscher, E., Menou, K., Seager, S., et al. 2007, *'Toward Eclipse Mapping of Hot Jupiters'*, *Astrophys. J.*, **664**, 1199

Raymond, S. N., Mandell, A. M., & Sigurdsson, S. 2006, *'Exotic Earths: Forming Habitable Worlds with Giant Planet Migration'*, Science, **313**, 1413

Raymond, S. N., Quinn, T., & Lunine, J. I. 2007, *'High-Resolution Simulations of The Final Assembly of Earth-Like Planets. 2. Water Delivery And Planetary Habitability'*, Astrobiology, **7**, 66

Raval, A., & Ramanathan, V. 1989, *'Observational determination of the greenhouse effect'*, Nature, **342**, 758

Ricker, G. R., Latham, D. W., Vanderspek, R. K., et al. 2009, *'The Transiting Exoplanet Survey Satellite (TESS)'*, Bulletin of the American Astronomical Society, 41, #403.01

Robinson, T. D., Meadows, V. S., Crisp, D., et al. 2011a, *'Modeling the Infrared Spectrum of the Earth-Moon System: Implications for the Detection and Characterization of Earthlike Extrasolar Planets and Their Moonlike Companions'*, Astrobiology, **11**, 393

Robinson, T. D., 2011b, *'Earth as an Extrasolar Planet: Earth Model Validation Using EPOXI Earth Observations'*, *Astrophys. J.*, **741**, 51

Rossow, W.B., Walker, A.W., Beuschel , D. E., & Roiter, M. D. 1996, *'International Satellite Cloud Climatology Project (ISCCP). Documentation of New Cloud Datasets'*, World Meteorological Organization, WMO/TD-No. 737, 115

Rutten, R. C. M. 1996, *'Eclipse mapping and related techniques (review)'*, Stellar Surface Structure, **176**, 69

Sagan, C., Thompson, W. R., Carlson, R., Gurnett, D., & Hord, C. 1993, *'A search for life on Earth from the Galileo spacecraft'*, Nature, **365**, 715

Sanromá, E., & Pallé, E. 2012, *'Reconstructing the Photometric Light Curves of Earth as a Planet along Its History'*, *Astrophys. J.*, **744**, 188

Sanromá, E., Pallé, E., & García Munõz, A. 2013, *'On the Effects of the Evolution of Microbial Mats and Land Plants on the Earth as a Planet. Photometric and Spectroscopic Light Curves of Paleo-Earths'*, *Astrophys. J.*, **766**, 133

Schopf, P. S. 1980, *'The Role of Ekman flow and Planetary Waves in the Oceanic Cross-Equatorial Heat Transport'*, Journal of Physical Oceanography, **10**, 330

Seager, S., & Deming, D. 2009, *'On the Method to Infer an Atmosphere on a Tidally Locked Super Earth Exoplanet and Upper Limits to GJ 876d'*, *Astrophys. J.*, **703**, 1884

Selsis, F. 2002, *'Search for signatures of life on exoplanets'*, Earth-like Planets and Moons, **514**, 251

Selsis, F. 2004, *'The Atmosphere of Terrestrial Exoplanets: Detection and Characterization'*, ASP Conf. Ser. 321, Extrasolar Planets: Today and Tomorrow, ed. J. Beaulieu, A. Lecavelier Des Etangs, & C. Terquem, (San Francisco, CA: ASP), 170

Selsis, F., Chazelas, B., Bordé, P., et al. 2007, *'Could we identify hot ocean-planets with CoRoT, Kepler and Doppler velocimetry?'*, *Icarus*, **191**, 453

Selsis, F., Wordsworth, R., & Forget, F. 2011, *'Thermal phase curves of nontransiting terrestrial exoplanets. I. Characterizing atmospheres'*, *Astron. Astrophys.*, **532**, A1

Showman, A. P., Fortney, J. J., Lian, Y., et al. 2009, *'Atmospheric Circulation of Hot Jupiters: Coupled Radiative-Dynamical General Circulation Model Simulations of HD 189733b and HD 209458b'*, *Astrophys. J.*, **699**, 564

Showman, A. P., & Polvani, L. M. 2011, *'Equatorial Superrotation on Tidally Locked Exoplanets'*, *Astrophys. J.*, **738**, 71

Smith, G. L., Manalo-Smith, N., & Avis, L. M. 1994, *'Limb-darkening models from along-track operation of the ERBE scanning radiometer'*, Journal of Applied Meteorology, **33**, 74

Smith, R. S., Dubois, C., & Marotzke, J. 2006, *'Global Climate and Ocean Circulation on an Aquaplanet Ocean Atmosphere General Circulation Model'*, Journal of Climate, **19**, 4719

Snellen, I. A. G., de Kok, R. J., de Mooij, E. J. W., & Albrecht, S. 2010, *'The orbital motion, absolute mass and high-altitude winds of exoplanet HD209458b'*, *Nature*, **465**, 1049

Solomon, S., Qin, D., Manning, M., Chen, Z., Marquis, M., Averyt, K. B., Tignor, M., & Miller, H. L., (eds.), 2007, *'Contribution of Working Group I to the Fourth Assessment Report of the Intergovernmental Panel on Climate Change'*, Cambridge University Press, Cambridge, United Kingdom and New York, NY, USA.

Sotin, C., Grasset, O., & Mocquet, A. 2007, *'Mass radius curve for extrasolar Earth-like planets and ocean planets'*, *Icarus* **191**, 337

Sterzik, M. F., Bagnulo, S., & Palle, E. 2012, *'Biosignatures as revealed by spectropolarimetry of Earthshine'*, *Nature*, **483**, 64

Stone, P. H. 1972, *'A simplified radiative-dynamical model for the static stability of rotating atmospheres'*, Journal of Atmospheric Sciences, **29**, 405

Stone, P. H. 1978, *'Constraints on dynamical transports of energy on a spherical planet'*, Dynamics of Atmospheres and Oceans, **2**, 123

Suttles, J.T., Green, R.N., Smith, G.L., et al. 1989, *'Angular Radiation Models for Earth-Atmosphere Systems, Vol. 2, Longwave Radiation'*, NASA Rep RP 1184-VOL-2, 88

Tanner, A. M., Catanzarite, J., & Shao, M. 2006, *'Detection and mass characterization of terrestrial planets in the habitable zone with SIM PlanetQuest'*, *SPIE Conference Series*, 6268

Tanner, A. M., Law, N., Plavchan, P., & Catanzarite, J. 2010, *'The Final Report: Detecting Terrestrial Mass Planets Around M-dwarfs: Is SIM's performance competitive?'*, Bulletin of the American Astronomical Society, **42**, #380.04

Tinetti, G., Vidal-Madjar, A., Liang, M.-C., et al. 2007, *'Water vapour in the atmosphere of a transiting extrasolar planet'*, *Nature*, **448**, 169

Tinetti, G., Beaulieu J. P., Henning, T., et al. 2011, *'The science of EChO'*, IAU Symposium, **276**, 359

Tinetti, G., Beaulieu, J. P., Henning, T., et al. 2012, *'EChO. Exoplanet characterisation observatory'*, Experimental Astronomy, **34**, 311

Tokano, T. 2011, *'Planetary science: Arrow in Titan's sky'*, Nature Geoscience, **4**, 582

Traub, W. A., Kaltenegger, L., Jucks, K. W., & Turnbull, M. C. 2006,*'Direct imaging of Earth-like planets from space (TPF-C)'*, Proc. SPIE, **6265**, 626502

Trauger, J. T., & Traub, W. A. 2007, *'A laboratory demonstration of the capability to image an Earth-like extrasolar planet'*, *Nature*, **446**, 771

Trenberth, K. E., Fasullo, J. T., & Kiehl, J. 2009, *'Earth's Global Energy Budget'*, Bulletin of the American Meteorological Society, **90**, 311

Vázquez, M., Pallé, E., & Rodríguez, P. M. 2010, *'The Earth as a Distant Planet: A Rosetta Stone for the Search of Earth-Like Worlds'*, Astronomy and Astrophysics Library. ISBN 978-1-4419-1683-9. Springer-Verlag New York.

Vidal-Madjar, A., Arnold, L., Ehrenreich, D., et al. 2010, *'The Earth as an extrasolar transitting planet. Earth's atmospheric composition and thickness revealed by Lunar eclipse observations'*, *Astron. Astrophys.*, **523**, A57

von Paris, P., Hedelt, P., Selsis, F., Schreier, F., & Trautmann, T. 2013, *'Characterization of potentially habitable planets: Retrieval of atmospheric and planetary properties from emission spectra'*, *Astron. Astrophys.*, **551**, A120

Wächtershäuser, G. 1988, *'Biogenesis; Biological Evolution; Enzymes; Membranes; Models, Biological; Surface Properties; Templates, Genetic'*, Microbiol. Rev., **52**, 452

Wächtershäuser, G. 1990, *'The case for the chemoautotrophic origin of life in an iron-sulfur world'*, Origins of Life and Evolution of the Biosphere, **20**, 173

Walsh, K. J., Morbidelli, A., Raymond, S. N., O'Brien, D. P., & Mandell, A. M. 2012, *'Populating the asteroid belt from two parent source regions due to the migration of giant planets–"The Grand Tack" '*, Meteoritics and Planetary Science, **47**, 1941

Welsh, W. F., Orosz, J. A., Seager, S., et al. 2010, *'The Discovery of Ellipsoidal Variations in the Kepler Light Curve of HAT-P-7'*, *Astrophys. J. Lett.*, **713**, L145

Williams, D. M., & Pollard, D. 2002, *'Earth-like worlds on eccentric orbits: excursions beyond the habitable zone'*, International Journal of Astrobiology, **1**, 61

Williams, D. M., & Pollard, D. 2003, *'Extraordinary climates of Earth-like planets: three-dimensional climate simulations at extreme obliquity'*,International Journal of Astrobiology, **2**, 1

Williams, P. K. G., Charbonneau, D., Cooper, C. S., Showman, A. P., & Fortney, J. J. 2006, *'Resolving the Surfaces of Extrasolar Planets with Secondary Eclipse Light Curves'*, *Astrophys. J.*, **649**, 1020

Woolf, N. J., Smith, P. S., Traub, W. A., & Jucks, K. W. 2002, *'The Spectrum of Earthshine: A Pale Blue Dot Observed from the Ground'*, *Astrophys. J.*, **574**, 430

Wordsworth, R. D., Forget, F., Selsis, F., Millour, E., Charnay, B., & Madeleine, J.-B. 2011, *'Gliese 581d is the First Discovered Terrestrial-mass Exoplanet in the Habitable Zone'*, *Astrophys. J. Lett.*, **733**, L48

Wordsworth, R., Forget, F., Millour, E., Head, J. W., Madeleine, J.-B., & Charnay, B. 2013, *'Global modelling of the early martian climate under a denser CO_2 atmosphere: Water cycle and ice evolution'*, *Icarus*, **222**, 1